Fischer-Tropsch based Power-to-Liquid process –

Technical, economic, uncertainty and sensitivity analysis

A thesis accepted by the Faculty of Energy-, Process- and Bio-Engineering of the University of Stuttgart to fulfill the requirements for the degree of Doctor of Engineering Sciences (Dr.-Ing.)

by

Sandra Katharina Adelung

born in Stuttgart, Germany

Main Referee: Prof. Dr. rer. nat. André Thess
Co-Referee: Prof. Dr.-Ing. Elias Klemm

Date of oral exam: 13.07.2023

Institute for Building Energetics, Thermotechnology and Energy Storage (IGTE) at the University of Stuttgart

2023

Declaration

I certify that the dissertation entitled: „Fischer-Tropsch based Power-to-Liquid process – Technical, economic, uncertainty and sensitivity analysis“ is entirely my own work. Passages and ideas from other sources have been clearly marked.

Eigenständigkeitserklärung

Ich versichere, dass ich die vorliegende Dissertation mit dem Titel: „Fischer-Tropsch based Power-to-Liquid process – Technical, economic, uncertainty and sensitivity analysis“ selbständig verfasst und keine anderen als die angegebenen Quellen und Hilfsmittel benutzt habe. Passagen und Gedanken aus fremden Quellen sind als solche kenntlich gemacht.

Stuttgart, _____

_____

Sandra Katharina Adelung

Acknowledgments

The following thesis developed during my research work at the German Aerospace Center (DLR) at the Institute of Engineering Thermodynamics in Stuttgart. I am very grateful for all the people who have supported, inspired and encouraged me along this journey.

First of all, I would like to thank Prof. Thess for the opportunity to be considered as a PhD candidate, for his support and supervision, for the guidance but also for allowing me a certain degree of freedom to conduct my research. A special thank you also to Prof. Klemm, who did not hesitate a second to become my co-examiner for this thesis. Also, I want to thank my supervisor Uwe Dietrich for giving me the opportunity to conduct the thesis, for reviewing and supervision, for the lively discussions and for his support. A big thank you also to Marc Linder, who encouraged me especially in the very beginning and in the final steps. Many thanks also to Antje Seitz who helped me to prepare and shape the first idea of this work.

A huge thank you also goes to the colleagues in my research group, who for example aided me to optimize my presentations, not only for the PhD seminars but also for the many other conferences. They have been a great support not only on a scientific basis but also on a personal level. A very special thank you to Simon Maier for his helping hands in TEPET and other programming issues, to Julia Weyand and Felix Habermeyer for their thorough revision of my papers as well as to Moritz Raab for his moral support.

Furthermore, I'd like to thank all the PhD seminar attendees, whose input helped me a lot to shape and rethink my work. I am also very grateful to my TPT colleagues, especially Jonas Tombrink, Jörg Bürkle, Sergej Belik, Jonina Felbinger, Andrea Gutierrez, Manuel Moosmann and Philipp Knödler for the fruitful discussions and especially for listening, motivating and encouraging me.

Moreover, I want to thank my students and colleagues who supported the foundation prior this thesis: Torsten Ascher, Daniel König, Stefan Martin, Michael Speidel, Holger Fischer, Friedemann Albrecht, Stefan Estelmann, Marc Hochberger, Daniel Schnellbögl, Franziska Kratz, Hannes Kohler, Fabian Klein and Julian Schmidt.

Last but not least, I want to express my gratitude to the most important people in my life:

Danke Mama, Papa, Oma, Opa, Juli und Felix!

I could not have taken this journey without your support.

"Research means that you don't know, but are willing to find out" - Charles F. Kettering

List of contents

Abstract

Liquid synthetic fuels are an important pillar for the defossilization of the hard-to-electrify modes of transport such as aircrafts, ships and heavy trucks. One possibility to produce these liquid fuels is from water, carbon dioxide and electricity via reverse water-gas shift (RWGS) reaction and Fischer-Tropsch synthesis in a Power-to-Liquid process. High carbon efficiencies are only feasible through recycling of unwanted by-products and unconverted reactants to a reformer[1]. This increases the process' complexity as changes in the RWGS reactor influence the process performance and design. Yet, an optimum RWGS reactor operation has not been studied in literature so far.

Therefore, this work targets to fill this gap with a systematic analysis of the impact of varying RWGS operating conditions on the process performance with respect to both, efficiencies and net production costs, while also taking into consideration the uncertainty in the cost calculations. The resulting confidence intervals are further examined in a global sensitivity analysis to identify the main contributors to the uncertainty.

Low costs as well as high efficiencies result at pressure dependent optimum RWGS temperatures (plateaus). Both, a high Power-to-Liquid efficiency and low net production cost, can be achieved at around 5 bar and 800 °C. This optimum is robust to changes in technical parameters, for example changes of Fischer-Tropsch operating conditions or electrolyzer efficiency, as well as to economic uncertainties, especially hydrogen cost. No unwanted graphite formation occurred in the equilibrium calculations in the temperature region of the described plateaus. Experiments further indicate that a suitable catalyst may aid to push the carbon formation boundaries to broaden the possible RWGS operating window. Electricity cost is the main contributor to the net production cost. Reducing the full load hours of the electrolyzer may reduce the average electricity price. However, oversizing of the electrolyzer outweighs the benefit of cheaper electricity resulting in higher net production cost at reduced electrolyzer full load hours. The results of the uncertainty and global sensitivity analysis indicate that seven of the 60 input variables for the economic assessment have a relevant impact on the uncertainty (95 % confidence interval: 2.8-5.3 $€_{2019}/kg_{C5+}$). For the assessment of the sensitivity indices in the global sensitivity analysis, a combination of the Azzini estimators is recommended over the other investigated estimators in order to minimize the computational effort.

Overall, the conducted systematic analysis allows to identify the optimal design and operation of the Fischer-Tropsch based Power-to-Liquid process with particular focus on the RWGS operating conditions to yield robust low net production cost with quantified uncertainty.

[1] Reformer: Reforming of short chained hydrocarbons and conversion of CO_2 to CO via reverse water-gas shift reaction (RWGS).

Kurzzusammenfassung

Flüssige synthetische Kraftstoffe können einen wichtigen Beitrag zur Defossilisierung des Transportsektors leisten. Im sogenannten Power-to-Liquid Prozess werden aus Wasser, CO_2 und Strom über reverse Wassergas Shift Reaktion und anschließende Fischer-Tropsch Synthese synthetische Kohlenwasserstoffe hergestellt. Eine hohe Kohlenstoffausnutzung erfordert dabei die Rückführung der Nebenprodukte zu einem Reformer[2]. Trotz seiner zentralen Aufgabe im Prozess wurden der Reformer und sein Einfluss auf den Prozess bislang kaum untersucht.

Um diese Lücke zu schließen wurde eine detaillierte Untersuchung der Reformerbetriebsbedingungen und deren Auswirkungen auf den Prozess aus technischer und ökonomischer Sicht, unter Berücksichtigung der Unsicherheiten in der Ermittlung der Herstellungskosten, durchgeführt. Zur Identifikation der Haupteinflussfaktoren auf die resultierenden Konfidenzintervalle wurde die Unsicherheitsanalyse durch eine globale Sensitivitätsanalyse ergänzt.

Aus der Analyse der Reformerbetriebsbedingungen ergeben sich druckabhängig optimale Temperaturen (Plateaus). Sowohl eine hohe Energieeffizienz als auch geringe Kosten werden bei 5 bar und 800 °C erzielt. Dieses Optimum ist außerdem robust gegenüber Änderungen der Prozessbedingungen anderer Prozesseinheiten sowie gegenüber Unsicherheiten in den Kosten. Im Bereich der Plateaus wurde keine unerwünschte Kohlenstoffbildung in den Gleichgewichtsberechnungen nachgewiesen. Experimentelle Arbeiten zeigen außerdem, dass die Wahl eines geeigneten Katalysators die Kohlenstoffbildungsgrenzen weiter verschieben könnte, um so das mögliche Reformerbetriebsfenster zu vergrößern. Resultierend aus der ökonomischen Analyse wird deutlich, dass die Wasserstoffkosten, und darin insbesondere die Stromkosten, den größten Beitrag zu den Herstellungskosten liefern. Dennoch führt eine Reduktion der Elektrolysevolllaststunden nicht zu einer Reduktion der Herstellungskosten, da die Überdimensionierung des Elektrolyseurs die Kosten zu stark erhöht. Aus der Unsicherheits- und Sensitivitätsanalyse geht hervor, dass 7 der 60 unsicheren Eingangsvariablen aus der ökonomischen Analyse von Relevanz sind (95 % Konfidenzintervall: 2.8-5.3 $€_{2019}/kg_{C5+}$). Zur Ermittlung der Sensitivitätsindizes in der globalen Sensitivitätsanalyse empfehlen sich die Schätzverfahren von Azzini, um den Rechenaufwand zu minimieren.

Zusammenfassend ermöglicht die in der vorliegenden Arbeit durchgeführte systematische Analyse die Ermittlung des optimalen Prozessdesigns und -betriebs zur Minimierung der Kosten unter Berücksichtigung der Unsicherheiten in den Herstellungskosten.

[2] Reformer: Reformierung kurzkettiger Kohlenwasserstoffe als auch die Umwandlung von CO_2 zu CO über die reverse Wassergas-Shift Reaktion (RWGS).

Nomenclature

Abbreviations

Cj	hydrocarbon with *j* carbon atoms
Cj+	fraction of hydrocarbons with at least *j* carbon atoms
COMP	compressors and pumps
FT(S)	Fischer-Tropsch (synthesis)
GSA	global sensitivity analysis
H2tL	Hydrogen-to-Liquid part of the plant
HC	hydrocracker
HEX-j	heat exchanger *j*
MEA	monoethanolamine
PEM	proton exchange membrane
PtL	Power-to-Liquid
RWGS	reverse water-gas shift
TEA	techno-economic analysis
TEPET	techno-economic process evaluation tool
UA	uncertainty analysis
V-j	valve *j*
WHB	waste heat boiler

Variables and constants (Greek characters)

η_c	carbon efficiency
η_H	hydrogen efficiency
η_{PtL}	Power-to-Liquid efficiency

Variables and constants (Latin characters)

CAPEX	capital expenditures
CI	confidence interval
ΔH_R^0	standard reaction enthalpy
LHV_{C5+}	lower heating value of C5+ product fraction
NPC	net production cost
OPEX	operational expenditures
S_i	first-order/main effect index of input variable *i*
S_{Ti}	total order/effect index of input variable *i*
T_{CI}	threshold 95 % confidence interval

Figures

1. Introduction

The following introduction is divided into three subchapters. The first subchapter targets to establish the context and to provide background information that lead to the overarching research question and with that to the motivation of this thesis. The second subchapter elaborates on the different research objectives that were set in order to fulfill the overall goal. Moreover, this subchapter targets to shortly review what was already available in the literature to depict the research gap. The last subchapter deals with the methodological advances that were necessary in order to approach the defined research objectives.

1.1. Background and Motivation

One of the main current challenges of mankind is to reduce the anthropogenic greenhouse gas emissions to drastically decrease their impact on the world's climate. Global actions are necessary in order to solve this overarching challenge. One important contributor to the greenhouse gas emissions is the transport sector, which emitted 7.7 Gt of CO_2 in 2021 (approx. 16 % of the global greenhouse gas emissions) [1]. Especially in the hard-to-electrify sectors, such as aviation and shipping, alternatives beyond hydrogen and synthetic natural gas are crucial [2]. In these cases, a high volumetric energy density is essential. A suitable **high-volumetric-energy-density-syncrude** can be derived through **Fischer-Tropsch (FT) synthesis** [3]. Moreover, synthetic Fischer-Tropsch fuels are already certified as drop-in jet fuel according to ASTM D5766-20b (50 % blending limit) [4].

The FT synthesis requires a source for carbon monoxide and hydrogen (equation (iii)). Carbon monoxide can be produced from carbon dioxide with hydrogen through the reverse water-gas shift reaction (RWGS) (equation (ii)). **Carbon dioxide** may originate from **point sources** or directly from air. Direct air capture is more cost- and energy-intensive regarding the provision of concentrated CO_2 in comparison to point sources [5]. However, point sources are limited and some may originate from fossil fuels [5]. It is likely that some of these fossil-fuel-based point sources will become unavailable in the upcoming decades due to the transition towards decarbonization, e.g. electrification or combustion of hydrogen instead of fossil fuel combustion. However, one interesting point source for CO_2 capture and utilization offers the **cement and concrete industry**. More specific, the **calcination process** (mineral decomposition of limestone) produces a significant amount of CO_2 that does **not originate from fossil fuels**. Over 60 % of the total CO_2 emissions (2.7 Gt CO_2/a_{2020} total CO_2 emissions) from modern cement plants originate from this calcination process [6, 7]. The cement industry has published a roadmap towards carbon neutrality in 2050, see Figure 1 [7]. They estimate that 1.37 Gt/a

CO_2 will have to end up in carbon capture and utilization as they cannot be avoided through other actions such as efficiency improvements or use of alternative carbon neutral fuels [7]. Hence, 373 Mt/a of carbon, in the form of CO_2, will be available even in the long run.

A **high carbon efficiency is essential** in order to fully exploit the limited amount of point sources. Stoichiometrically, the maximum carbon efficiency of the investigated process is $\eta_{C,stoichiometry}$ **= 100 %** (one CO_2 molecule reacting first to CO and then to -CH_2-, see equation (iv)). More realistically, applying a carbon efficiency of 83 % towards C5+ components in the FT process (see chapter 3.1) results in 310 Mt of carbon to be potentially incorporated from the cement plant into the C5+ product. In 2019 the global jet fuel demand was 288 Mt/a_{2019} jet fuel (≈ 247 Mt/a $carbon_{2019}$ in the form of jet fuel) [8]. Thus, on a global scale, the current jet fuel demand could be satisfied by the carbon available from the cement plant point source. The International Air Transport Association's vision is to produce 360 Mt/a_{2050} (≈ 309 Mt/a_{2050} carbon in the form of jet fuel) of sustainable aviation fuels (SAF) in 2050 (65 % of the overall demand) [9]. Prospectively, it seems that **the projected SAF demand for 2050 could be satisfied from the cement plant point source** assuming that all the CO_2 from the cement plants that cannot be avoided in 2050 is used for this purpose.

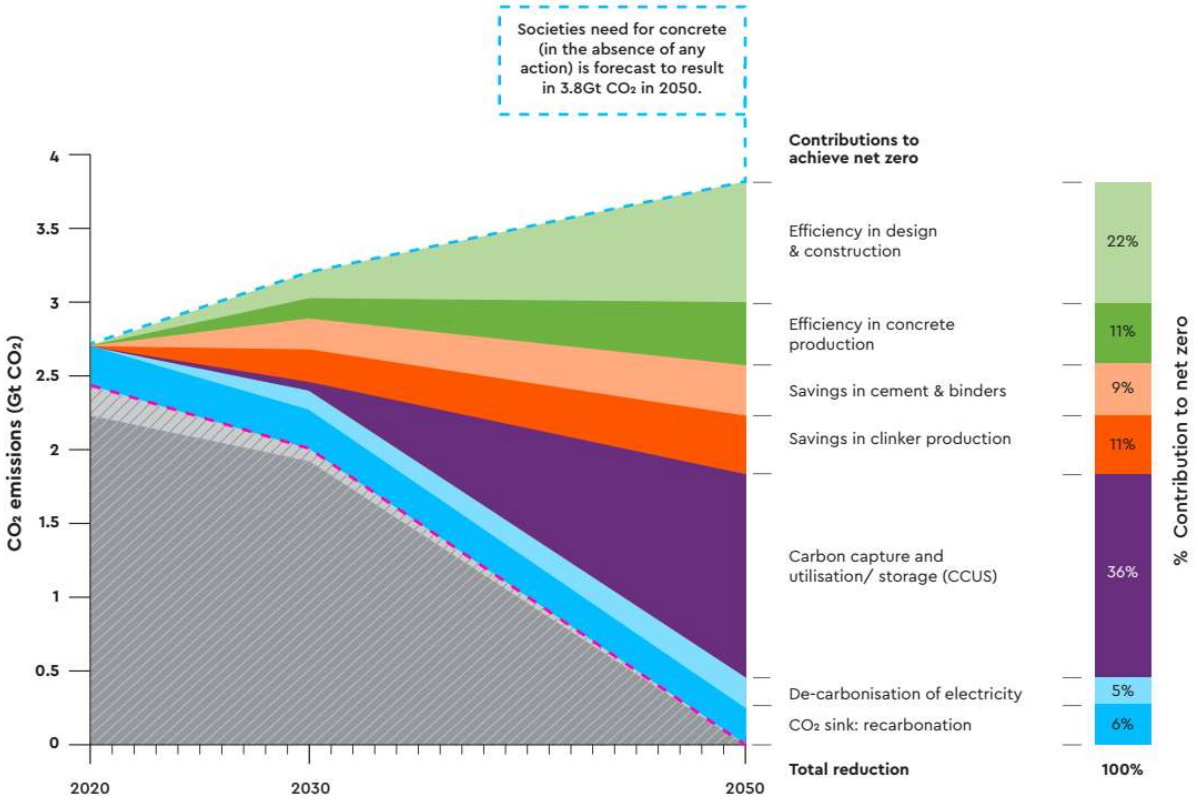

Figure 1: Global Cement and Concrete Association's roadmap towards carbon neutrality in 2050 [7].

The second reactant required for FT synthesis is **hydrogen**. It may be derived from the electrochemical reaction via **water electrolysis** or from biomass gasification. Two major drawbacks regarding the use of biomass as hydrogen source are the higher water demand and land-use for biomass cultivation,

which both are also of social relevance (fuel vs. food) [10]. In contrast, producing hydrogen via electrolysis requires significantly less water as well as land-use [10]. However, in order to reduce the greenhouse gas emissions in comparison to fossil fuel combustion, this approach requires electricity with a small carbon footprint (renewable electricity). Furthermore, the electricity must either be readily available for steady-state baseload operation or dynamic operation plus hydrogen storage is required.

The water electrolysis is an energy intensive step (equation (i)) and therefore it is essential to target a high hydrogen-to-fuel conversion and thus, a high hydrogen efficiency. Hydrogen is not only required for the FT synthesis itself but also to activate the very stable CO_2 molecule to form CO in the endothermic reverse water-gas shift reaction (see equation (ii)). Three water molecules form three H_2 molecules in the electrolysis step (3·(i)). Subsequently, one H_2 molecule is required to convert CO_2 to CO while producing one molecule of water (ii). Two H_2 molecules are then converted to form one molecule -CH_2- and one water molecule (iii). Thus, two of the three H_2 molecules end up to form water and one ends up in -CH_2-. Hence, the **maximum hydrogen efficiency** is $\eta_{H,stoichiometry}$ **= 33 %**.

From the reaction enthalpies, the maximum theoretical chemical conversion efficiency, or Power-to-Liquid efficiency, is $\eta_{PtL,theoretical}$ **= 70 %$_{LHV}$** (combustion heat of -CH_2- in relation to the energy demand for electrolysis and RWGS, equation (ix)). However, it is worth noting that typical polymer electrolyte membrane (PEM) electrolyzers have a system energy demand of 4.5-7.5 kWh/Nm^3 = 368-613 kJ/mol (in comparison: 286 kJ/mol for the ideal system) [11]. This lowers the PtL efficiency already to 33-55 %$_{LHV}$, which cannot be overcome through improved process design but only through improvement of the electrolyzer technology itself. In this work an (optimistic) PEM efficiency of 4.4 kWh/Nm^3 = 357 kJ/mol is assumed, resulting in a maximum chemical energy conversion efficiency of $\eta_{PtL,benchmark}$ **= 56 %$_{LHV}$.** This is the benchmark efficiency for the process optimization.

Power-to-Liquid Process:

$H_2O_{(l)} \rightarrow H_2 + 0.5\ O_2$	$\Delta H_R{}^0 = 286\ \mathrm{kJ/mol}$	(i)
$CO_2 + H_2 \rightleftharpoons CO + H_2O_{(g)}$	$\Delta H_R{}^0 = 41\ \mathrm{kJ/mol}$	(ii)
$CO + 2\ H_2 \rightarrow (-CH_2-) + H_2O_{(g)}$	$\Delta H_R{}^0 = -152\ \mathrm{kJ/mol}$	(iii)
$3\ H_2O_{(l)} + CO_2 \rightarrow 1.5\ O_2 + 2\ H_2O_{(g)} + (-CH_2-)$	$\Delta H_R{}^0 = 747\ \mathrm{kJ/mol}$	(iv)=3·(i)+(ii)+(iii)

Combustion Process:

$1.5\ O_2 + (-CH_2-) \rightarrow H_2O_{(g)} + CO_2$	$\Delta H_R{}^0 = -625\ \mathrm{kJ/mol}$	(v)
$3\ H_2O_{(g)} \rightarrow 3\ H_2O_{(l)}$	$\Delta H_R{}^0 = -122\ \mathrm{kJ/mol}$	(vi)

Energy Balance per mol (−CH_2−):

Benefit: (625 + 152 + 122) kJ = 899 kJ (vii)=(iii)+(v)+(vi)

Effort: (3 · 286 + 41) kJ = 899 kJ (viii)=3·(i)+(ii)

Power-to-Liquid Efficiency:

$\eta_{PtL,theoretical}$ = 625 / 899 = 70 $\%_{LHV}$ (ix) =(v)/(viii)

$\eta_{PtL,benchmark}$ = 625 / 1112 = 56 $\%_{LHV}$ (x)

Figure 2 shows the simplified block diagram of the investigated Fischer-Tropsch based Power-to-Liquid process concept. CO_2 is recovered from cement plant off-gas through amine absorption, which requires thermal energy for the desorption process. The heat for the desorption process can be provided from the exothermic FT reaction. The heat that is required for the **endothermic RWGS** reaction, at rather **high temperatures well above 600 °C** (see Chapter 3.1), is provided through oxy-fuel combustion of a partial amount of the recycled gases. The oxygen required for the oxy-fuel combustion is derived from the electrolysis alongside the hydrogen. The RWGS product syngas is subsequently converted in the FT reactor. The FT product is separated and long chained hydrocarbons are further processed in a hydrocracker to maximize the yield in the target hydrocarbon chain length (target: C5-C23).

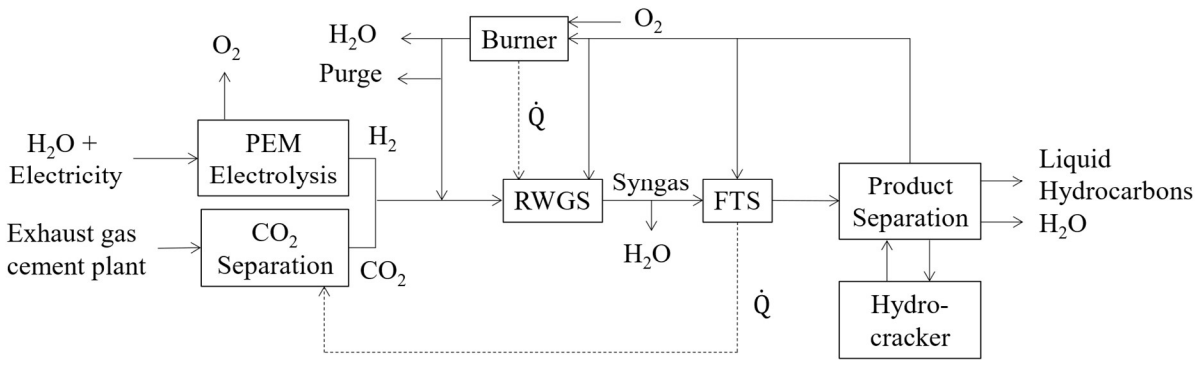

Figure 2: Simplified block diagram of the investigated Fischer-Tropsch based Power-to-Liquid process with reverse water-gas shift CO_2 activation.

Neither the RWGS nor the FT reactor allow for full conversion in a once-through process operation. Therefore, **recycling** of the reactants **is essential** in order to establish a **high carbon efficiency**. Additionally, the FT reaction does not only produce the desired C5+ fraction but also to some extent C1-C4 molecules, which are not assumed to be valuable products in this case. Recycling the by-products to the RWGS is very beneficial as it enables these by-products to be reformed again to carbon monoxide and hydrogen. Moreover, the recycling to the RWGS allows to activate unreacted CO_2. This is an excellent feature from the overall process perspective because it allows to increase the carbon efficiency when carbon containing by-products are yet again reactivated to potentially form C5+ components in the FT reactor.

High temperature is required in order to achieve high CO yields in the endothermic RWGS unit - see Appendix B for the entire reaction network and reaction enthalpies. However, the higher the temperature the higher the thermal heat demand for heating up the feed stream and the more issues may arise from a material perspective (e.g. catalyst, steel). The RWGS reaction is an equimolar reaction. Hence, the equilibrium is not affected by pressure. Nevertheless, unwanted side reactions (methane and carbon formation) are depending on the applied pressure. Especially, methane formation is favored at elevated pressure. Therefore, it seems favorable to operate the RWGS at low pressure in order to maximize the CO yield. Still, from the overall process design it might be more favorable to operate the RWGS and FT reactor at similar pressure levels (25 bar) to avoid excessive compression work. To summarize, these conflicting targets require a holistic process assessment. **As the RWGS reactor is a central step in the PtL process, the detailed investigation of the RWGS operating conditions and their impact on the overall process performance gave the main motivation for the research objectives defined in the following subchapter.**

1.2. Research Objectives

As described in the previous subchapter, the RWGS operating conditions have a strong impact on the overall process performance. The optimal operating conditions are not straight forward as increasing pressure and temperature have both positive and negative effects on the process efficiency and production cost. Overall, the aim is to identify a techno-economically optimal process design and operation mode. However, the input data for the economic analysis is a priori uncertain and is therefore only an approximation. A comparison of different designs and operating conditions requires a quantification of the uncertainty of the economic data in order to clearly rank the different options.

Conclusively, the aim is to analyze the Fischer-Tropsch based Power-to-Liquid process targeting (compare Figure 3):

- to optimize the operating conditions in order to **maximize** the overall process **efficiency** (Technical Analysis in Paper 1 & 2),
- to **minimize** the net production **cost** (Economic Analysis Paper 2 & 3) and
- to **quantify** and **allocate** the **uncertainties** deriving from the economic analysis (Uncertainty and Global Sensitivity Analysis Paper 2 & 3).

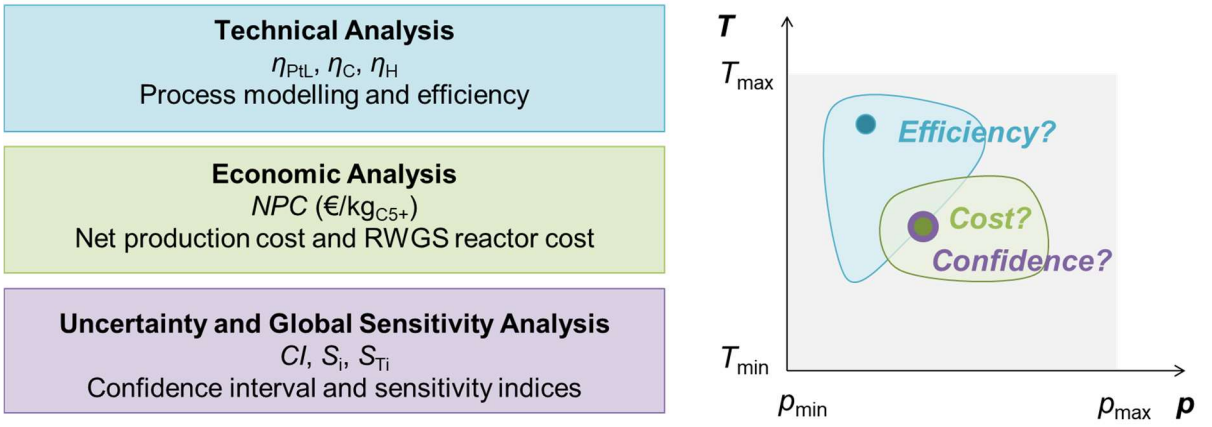

Figure 3: Key research objectives in the context of the Fischer-Tropsch based Power-to-Liquid process examining the impact of the (RWGS) operating conditions, e.g. pressure *p* and temperature *T*, on the process performance.

Technical Analysis:

The Fischer-Tropsch based Power-to-Liquid process has already been subject to different studies, which investigated different process designs, for example different strategies for using the tail gas, different hydrogen and carbon monoxide production routes and different FT reactors [12-19]. Similar process designs as in this thesis are available in [16, 19]. Vázquez *et al.* elaborate on the performance of the PtL bench-scale plant SOLETAIR and outline further improvement in a theoretical analysis [19]. Their PtL pilot plant comprises a small scale RWGS (allows to process 2 L_N/min or 233 g/h of CO_2), which is heated by an electrical oven [19]. The reaction is conducted over a monolithic precious metal catalyst at 1-5 bar and 850 °C [19]. They expect process performance improvements with increased RWGS pressure to FT pressure (20-30 bar) [19]. König *et al.* set up a PtL process model and evaluate the process for a fixed set of unit assumptions [16]. Their RWGS is assumed to operate at 25 bar and 900 °C [16]. **Neither** of these approaches **shows the impact of varying RWGS operating conditions** in a detailed manner **nor** do they **provide insight on how they chose their operating conditions**. Therefore, the first research objective is to **analyze the effect of variable RWGS operating conditions on the process efficiencies**:

- **Hydrogen and carbon efficiency**: Amount of hydrogen from water and carbon from CO_2 required for the fuel production at varying RWGS operating conditions.
- **Power-to-Liquid efficiency**: Amount of electrical energy required to produce the desired liquid hydrocarbons at variable RWGS operating conditions.

The goal is to identify the optimum operating conditions and the main correlations that lead to these optimum conditions. Beyond that, it is essential to investigate the **robustness of this optimum** to clarify whether small changes in other variables significantly affect the optimum RWGS operating conditions.

Economic Analysis:

Similarly to the technical analysis, economic evaluations for different syngas/hydrogen production pathways are available in the literature: co-electrolysis [14, 20, 21], solid oxide electrolysis [22], PEM [23-26] and alkaline electrolysis [14, 27]. The synthesis gas in this thesis is provided from PEM electrolysis and allothermal RWGS reaction with oxy-fuel combustion. Similar setups have been investigated by [23, 24, 26]. König *et al.* investigate the impact of full load hours, electricity costs and electrolyzer costs on the *NPC* [26]. They retrieve the RWGS reactor cost from [28], who base their RWGS reactor cost on water gas-shift reactor cost from source [29]. However, the operating conditions and the reactor design of a WGS (exothermic) reactor is very different from a RWGS (endothermic) reactor. Tremel *et al.* do not calculate the cost based on process modelling and equipment-based calculations [23]. Hence, it is not possible to outline the differences of the process designs and unit assumptions. Schemme *et al.* do not state their assumed RWGS reactor cost [24]. Furthermore, the allothermal oxy-fuel RWGS was not available at large scale [30]. As a result, **no reliable RWGS reactor cost** were **available** in the literature.

In order to complement the technical analysis with an economic analysis (economic and energetic optimum operating conditions may differ), the target is to:

- analyze the impact of the RWGS operating conditions on the **net production costs**,
- identify the RWGS operating conditions exhibiting the lowest net production cost and
- evaluate the **robustness** of the **economically optimal RWGS** operating conditions.

As mentioned, literature was lacking sufficient data for the reactor cost. Moreover, the reactor cost should be sensitive to changes in RWGS operating conditions to fulfill the target objective. Thus, a **methodology** needed to be **developed to estimate the RWGS reactor cost at varying RWGS operating conditions**. More specific this method requires the consideration of:

- factors directly impacting the reactor setup (for example different wall thicknesses of the reactor tubes at different RWGS pressures and temperatures) and
- factors indirectly impacting the reactor setup through changes in process streams (for example heat demand of the RWGS reactor, different feed compositions and mass/volumetric flow rates at different RWGS operating conditions).

A preliminary cost breakdown analysis indicated that the electricity cost for the electrochemical hydrogen production is a major contributor to the overall net production cost of the syncrude. The wholesale electricity price fluctuates throughout the year. Thus, the cost for electricity can be reduced by operating the electrolyzer at times when cheap electricity is available. None of the available works have explored the **impact of the electrolyzer full load hours on the wholesale electricity price,**

electrolyzer cost, hydrogen storage cost, stack replacement cost and finally the resulting net production cost [23, 26, 31]. Overall, the question is whether **this alternative mode of operation is economically beneficial**.

Uncertainty and Global Sensitivity Analysis:

The resulting net production cost from the deterministic model evaluation are intrinsically uncertain for example due to uncertainty in equipment cost or cost factors applied. A quantification of the uncertainty allows for a clear ranking of the operating conditions, if no overlapping confidence intervals are observed. Uncertainty may also arise from decision variables, where the actual value is not defined at the time of the evaluation. Then it might be helpful to investigate which input design variable should be investigated in detail and which can be fixed to a certain value without major impact on the result. This can be approached through global sensitivity analysis (GSA). While most researchers apply one-factor-at-a-time methods to conduct (local) sensitivity analyses, this approach is only valid for linear models. Global sensitivity analysis overcomes this issue and broadens the applicability to non-linear systems. However, techno-economic process analyses are seldomly complemented by uncertainty analysis (UA) or a proper sensitivity analysis beyond the typical one-factor-at the time methods. Still, there are a few publications that either complement or solely focus on conducting global uncertainty and sensitivity analysis. For example, some fields where UA and/or GSA are applied are biomass-based processes [32-39], carbon capture and storage [40-44], energy system analysis [45], wind farms [46] and photovoltaics [47, 48]. All of these studies include UA and a few also feature global sensitivity analysis. **No literature** was available that investigates the **economic uncertainty of a Fischer-Tropsch based Power-to-Liquid process**.

The calculation of the sensitivity indices in the variance-based global sensitivity analysis relies on the use of estimators and sampling strategies. Research is still ongoing in the formulation and identification of the most suitable estimators and sampling methods. Therefore, a few estimators are compared in order to find the most suitable one for this application. Thus, the methodological advances to arise from this thesis regarding GSA and UA with respect to techno-economic process analysis are:

- the identification of the **estimator** to conduct GSA at the **lowest computational effort**,
- the identification of the **sampling method** for **fast convergence** and
- to develop an **intuitive workflow to conduct combined GSA and UA**.

With respect to the Fischer-Tropsch based Power-to-Liquid process the tasks for GSA and UA are:

- to identify and **fix non-influential input variables** to reduce the complexity (first dataset contained more than 60 uncertain input variables),

- to **prioritize** the **important input variables** with respect to their impact on the overall uncertainty,
- to **analyze important decision variables** in order to fix them to their most beneficial value (full load hours of the electrolyzer as decision variable) and
- to **quantify** the remaining **uncertainty of the net production cost** after fixing the decision variable(s) and non-influential input variables.

1.3. Methodology

This subchapter targets to give an overview on the methodological advances that were necessary to fulfill the objectives while referencing to the corresponding publication which describes the methodological approach in every detail. Figure 4 summarizes the key methodological advances and the tools required in order to answer the research questions of this thesis. The general process model description including a thorough description of the different process units is provided in Paper 1. The RWGS reactor cost model is presented in Paper 2. The ranges of uncertainty applied and the methodology used for allocating the overall uncertainty to the different uncertain input variables are explained in Paper 3.

A **flexible and interdependent process model** was set up using **flowsheeting** software **Aspen Plus®** (Paper 1). Hydrogen and carbon dioxide provision are modelled as black box models with specified energy and material flows. Hydrogen is provided from water and electricity via PEM electrolysis with a system efficiency of 66 $\%_{LHV}$ [49], [50]. CO_2 is captured from a cement plant requiring 3.8 MJ_{th}/kg $CO_{2,\ captured}$ of thermal (at 120 °C) and 0.14 MJ_{el}/kg $CO_{2,\ captured}$ of electrical energy [51]. The **RWGS reactor** is modelled as a Gibbs reactor assuming **thermodynamic equilibrium** and variable operating conditions [16, 52]. Details on the RWGS reactor such as reactor types, catalytical requirements, carbon formation, metal dusting, model development and relevant experiments are outlined in Appendix B. The Fischer-Tropsch reactor is modelled as a stoichiometric reactor at 25 bar and 220 °C [53-55] applying the chain growth probability α [56]. The hydrocracker model is based on a yield reactor [57, 58] . More information on the FT reactor such as reactor types, catalysts, operating conditions, available plant sizes and the model development are described in Appendix C.

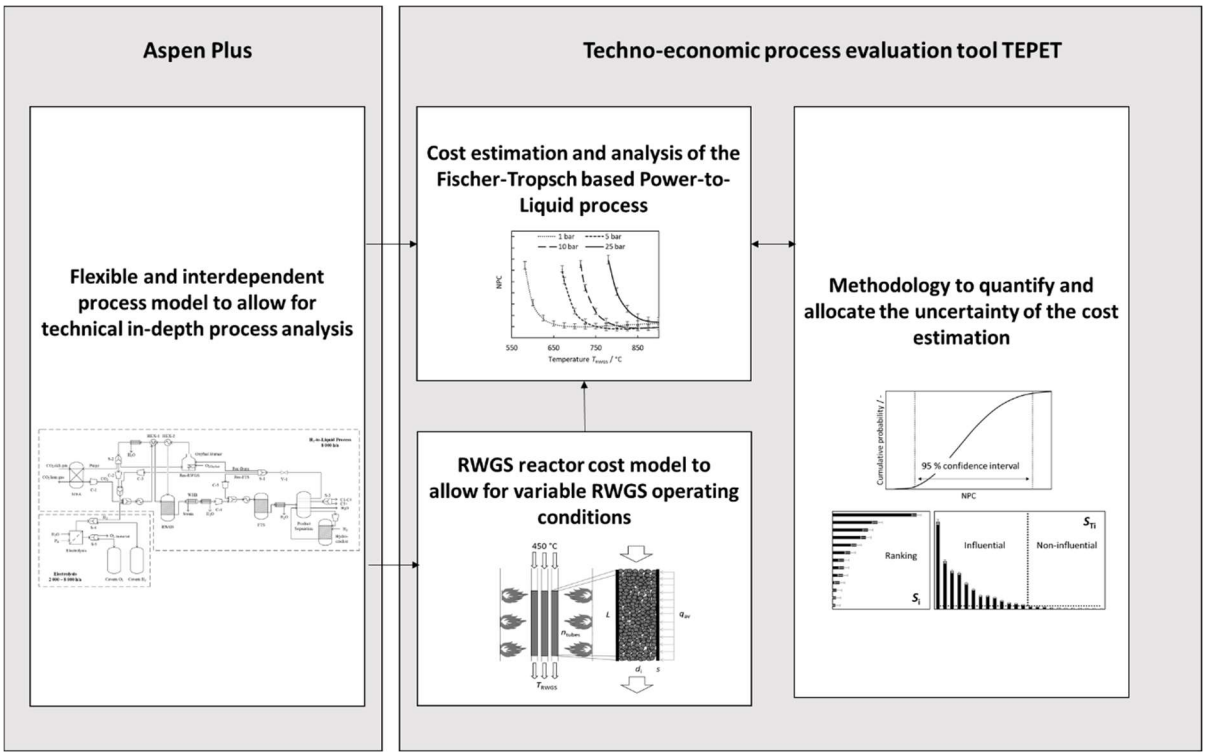

Figure 4: Overview of the methodological advances required to tackle the research objectives.

The resulting flowsheet is depicted in in Figure 5. The model was set up to allow for the necessary **flexibility** in **varying RWGS operating conditions** without excessive modelling and simulative effort for constant units that are not affected by these variations (e.g. the hydrogen production). Changes in RWGS pressure and temperature directly affect the yields as the thermodynamic equilibrium is shifted. Hence, the product composition from the RWGS reactor changes, which would subsequently change the feed of the FT reactor. In order to ensure that the FT reactor is operated at validated and safe operating conditions, the process model was designed such that the H_2/CO ratio and inert gas content in the feed of the FT reactor are constant. This was established through regulation of the split ratios of the recycling streams and by regulating the amount of CO_2 that enters the PtL process (details on the split ratios, see Paper 1). Nevertheless, different FT operating conditions (temperature, conversion, inert gas content) are additionally investigated in order to identify the impact of different FT operating conditions on the optimum RWGS operating conditions.

The possible operating window of the RWGS reactor is additionally narrowed down by unwanted **carbon formation**, which is investigated by assuming carbon as graphite in equilibrium calculations. However, it is worth to mention that experiments were conducted prior to this thesis that indicate that using suitable catalysts may broaden the possible operating window as no carbon formation was observed even under operating conditions that predict graphite formation in the equilibrium calculations (see Appendix A).

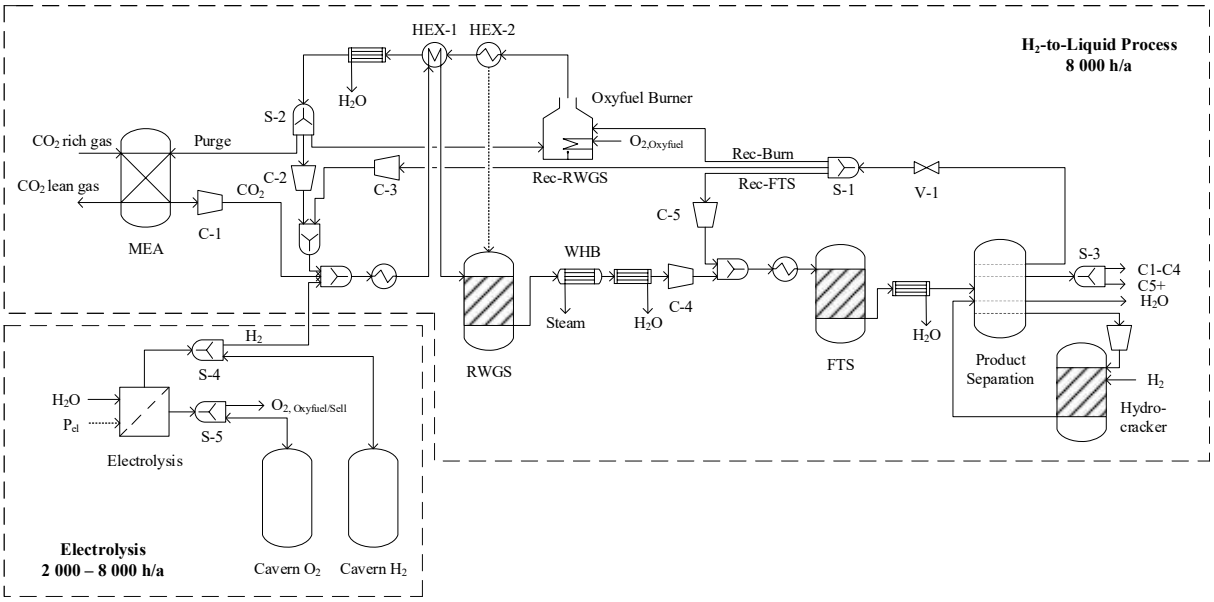

Figure 5: Flowsheet of the Power-to-Liquid process consisting of a hydrogen supply part and a H2tL part (reproduced from Paper 3) [59]. MEA-monoethanolamine absorption, WHB-waste-heat boiler, S-j-Split, C-j-compressor, V-j-valve.

DLR's Inhouse-Tool TEPET [25] accesses the process data for calculating the net production cost from the Aspen Plus® process simulation. The methodology used for calculating the net production cost is based on the methods available for the chemical industry [60]. It is widely accepted to be applicable for estimating the production cost of alternative fuels [25, 26]. Cost functions for standard equipment such as heat exchangers, columns, pumps and compressors are available from Peters *et al.* [60]. The remaining equipment cost (e.g. electrolyzer, FT reactor, hydrocracker) as well as the specific cost data for raw materials and utilities are taken from different literature sources (see Paper 2 and 3 [59, 61]). Typically, an equipment cost function is available for a fixed set of operating conditions and only scaled with the throughput in the form of e.g. mass flow, heat that is transferred, or similar. In order to calculate the **net production cost at varying RWGS operating conditions** it is necessary to set up a model that allows to estimate the **RWGS reactor cost depending on specific RWGS operating conditions**. Therefore, a **submodule** is **added to the existing TEPET tool** that allows to calculate the RWGS reactor cost depending on input data that is derived from the Aspen Plus® simulation such as heat duty and feed properties (see Paper 2). The reactor cost model firstly seeks to identify the **design criterion for the tubes** inside the combustion chamber. The design criterion may be based on a **limitation through heat transfer, reaction rates or pressure drop**. The **number of tubes, tube diameter and tube length** are then subject to an **optimization in order to establish the lowest reactor cost**. For a detailed description on the established model refer to Paper 2 [61].

Quantification and allocation of the economic uncertainties aids the evaluation of the economic results. In order to assess the confidence levels of the cost estimation and further to conduct the global sensitivity analysis, **TEPET is extended by integration of a UA/GSA module** (for the workflow see Paper

3, Figure 1 [59]). The integration allows to transfer the base case economic data into the UA/GSA module. As a first step in the module extension, the uncertain input variables and their probability functions have to be defined to reflect the uncertainty of each uncertain input variable. These probability functions are then processed in a module that calculates the **combined probability function (Monte-Carlo method)** for this set of input data in order to **quantify** the overall **uncertainty**. Therefore, the net production cost calculations need to be conducted several thousand times in order to establish a good fit for the combined probability function. From this combined probability function, the confidence interval, e.g. 95 % confidence interval, can readily be derived. The Monte-Carlo approach is a well-established technique in uncertainty analysis [62, 63]. The input probability functions are also used to conduct the **global sensitivity analysis**, which is a very helpful method in **identifying non-influential parameters** and also to **rank influential parameters** for further processing. The global sensitivity analysis is established using a variance-based approach which allows to calculate **first and total order indices** that are then used to rank and fix the parameters. This approach relies on the usage of estimators to calculate these indices. Research is still ongoing for identifying the most suitable estimators, especially with respect to the total order indices [64-66]. Therefore, in this thesis**, different estimators are compared with respect to their computation effort** in order to identify the most suitable for this application. A detailed description of the methodology to conduct the uncertainty and global sensitivity analysis is available in Paper 3.

Different system boundaries are set in order to fit the **different objectives** in the three publications. Paper 1 focuses on the technical analysis, especially with respect to obtaining the RWGS operating conditions for obtaining the optimum Power-to-Liquid efficiency. Moreover, the efficiency of the electrolyzer is varied in a local sensitivity analysis in order to identify any impact of the electrolyzer on the optimum RWGS operating conditions. Thus, the hydrogen production is included such that water and electricity enter the model boundaries. Paper 2 focuses on obtaining the economically optimum RWGS operating conditions. Therefore, a broad range of hydrogen cost cases is investigated in order to provide robust optima. For this objective it is irrelevant whether the hydrogen cost is reduced through improved efficiency, through lower electricity prices or electrolyzer equipment cost. Consequently, the hydrogen production in Paper 2 is outside the model boundaries. The electricity cost for hydrogen production is a major driver of the net production cost. Therefore, the objective in Paper 3 is to make use of lower wholesale electricity prices at specific hours of the year. However, this requires hydrogen storage and electrolyzer overcapacity in return. The flowsheet of this process is depicted in Figure 5. The hydrogen production and storage are calculated in dependence on the electrolyzer full load hours. The H2-to-Liquid part of the plant from Paper 3 is identical to the process in Paper 2. In the transition from Paper 1 to Paper 2, the focus shifts to the C5+ product fraction, which is why the efficiency definitions were adapted accordingly (see Chapter 3.1 for the final definitions in contrast to those used in Paper 1).

2. Publications

The following chapter contains the original articles and highlights the contributions of the authors. The three manuscripts are:

Paper 1: Impact of the reverse water-gas shift operating conditions on the Power-to-Liquid process efficiency
Sandra Adelung, Simon Maier, Ralph-Uwe Dietrich
Sustainable Energy Technologies and Assessments, Volume 43, February 2021, 100897,
https://doi.org/10.1016/j.seta.2020.100897, Copyright Elsevier

Paper 2: Impact of the reverse water-gas shift operating conditions on the Power-to-Liquid fuel production cost
Sandra Adelung, Ralph-Uwe Dietrich
Fuel, Volume 317, June 2022, 123440,
https://doi.org/10.1016/j.fuel.2022.123440, Copyright Elsevier

Paper 3: Global sensitivity and uncertainty analysis of a Fischer-Tropsch based Power-to-Liquid Process
Sandra Adelung
Journal of CO2 Utilization, Volume 65, November 2022, 102171,
https://doi.org/10.1016/j.jcou.2022.102171,Copyright Elsevier

In addition to these journal publications, the research outcomes have been presented at national and international conferences:

- ProcessNet Jahrestagung der Fachgruppe Energieverfahrenstechnik (Frankfurt 2016): Reverse Wassergas-Shift-Reaktion und Reformierungsreaktionen zur Synthesegasbereitstellung im Power-to-Liquid Prozess (Poster)
- ProcessNet Jahrestagung (Aachen 2016): Reaktionskinetik der reversen Wassergas-Shift Reaktion bei Normaldruck zur Übertragung auf die Synthesegasbereitstellung im PtL-Prozess (Lecture)
- 10th World Congress of Chemical Engineering (Barcelona, 2017): Experimental investigation of the reverse water-gas shift reaction at high temperature and elevated pressure (Lecture)
- ProcessNet Jahrestagung der Fachgruppe Energieverfahrenstechnik (Frankfurt, 2018): Reaktorkonzept zur Untersuchung der reversen Wassergas-Shift Reaktion (rWGS) bei Hochtemperatur und erhöhtem Druck (Poster)
- ProcessNet Jahrestagung (Aachen, 2018): Energetische Bewertung der Betriebsbedingungen der Synthesegaserzeugung im Power-to-Liquid Verfahren (Lecture)
- 10th European Congress of Chemical Engineering (Florence, 2019): Syngas production in the Power-to-Liquid process - Techno-economic assessment of the operating conditions (Lecture)
- ProcessNet Jahrestagung der Fachgruppe Energieverfahrenstechnik (Online, 2021): Influence of the reverse water-gas shift operating conditions on the Power-to-Liquid process efficiency (Lecture)
- 13th European Congress of Chemical Engineering (Online, 2021): Techno-economic analysis of alternative fuel production routes – Uncertainty and Global Sensitivity Analysis (Lecture)

Paper 1

Impact of the reverse water-gas shift operating conditions on the Power-to-Liquid process efficiency

Sandra Adelung, Simon Maier, Ralph-Uwe Dietrich

The following research paper was published in
Sustainable Energy Technologies and Assessments
Volume 43, February 2021, 100897
https://doi.org/10.1016/j.seta.2020.100897

Contribution roles

Sandra Adelung:
Research work - Methodology and model development, formal analysis and data curation, investigation and validation
Writing – Conceptualization, visualization, original draft and editing

Simon Maier:
Provision of TEPET tool for techno-economic analysis, model development

Ralph-Uwe Dietrich:
Reviewing and supervision

Sustainable Energy Technologies and Assessments 43 (2021) 100897

Contents lists available at ScienceDirect

Sustainable Energy Technologies and Assessments

journal homepage: www.elsevier.com/locate/seta

Original article

Impact of the reverse water-gas shift operating conditions on the Power-to-Liquid process efficiency

Sandra Adelung *, Simon Maier, Ralph-Uwe Dietrich

German Aerospace Center (DLR), Pfaffenwaldring 38-40, 70569 Stuttgart, Germany

ARTICLE INFO

Keywords:
Synthetic fuels
Alternative fuels
rWGS
Syngas
Syncrude

ABSTRACT

Fischer-Tropsch based fuels from renewable electricity and carbon dioxide provide one possibility to defossilise the transport sector, especially where long distances and high loads require fuels with high energy density. In this work, a stationary Power-to-Liquid (PtL) process model is set up in Aspen Plus®. The process involves CO_2 absorption, water electrolysis, CO_2 activation by reverse water-gas shift reaction (rWGS), an oxyfuel burner, Fischer-Tropsch synthesis, product separation and hydrocracking. The influence of the rWGS operating conditions (pressure and temperature) on the overall process performance in terms of PtL-efficiency and hydrogen/carbon efficiency is investigated. The operating conditions are varied between 550 and 950 °C and 1–25 bar. The temperature and pressure dependent methane formation in the rWGS is found to have major influence on the efficiencies. For the base case, a maximum Power-to-Liquid efficiency of $\eta_{PtL} = 38.7$ % is obtained at 5 bar and 825 °C, while a maximum hydrogen efficiency of $\eta_H = 28$ % results at 1 bar and 725 °C. The carbon efficiency is found to be constant ($\eta_C = 88$ %). Sensitivity studies show that the optimum operating conditions are not affected significantly by variation of the investigated process variables.

Introduction

Motivation for Power-to-Liquid

In order to limit the temperature increase to 1.5 °C, in comparison to 1990 [1], global actions in all energy sectors have to be taken to reduce greenhouse gas emissions (GHG). One crucial contributor is the transport sector, where global direct emissions reached 7 Gt of CO_2 equivalents ($CO_{2,eq}$) in 2010 [2]. This correlates to 23 % of the total energy related emissions [2]. Decarbonizing the transport sector poses a challenge regarding the difficult-to-electrify sectors (marine, heavy-duty vehicles, aviation), where high energy densities are required. In 2010, aviation accounted for 10.6 % of the GHG emissions of the transport sector, which equals 743 Mt $CO_{2,eq}$ [2]. In 2016 the civil aviation sector emitted 814 Mt CO_2, which is about 2 % of the anthropogenic carbon emissions [3]. Without further action the carbon dioxide emissions are expected to increase due to passenger growth [4,5]. In 2009, to reduce GHG emissions in the aviation sector, the International Air Transport Association (IATA) set itself three main goals [5]:

- 1.5 % increase of fuel efficiency p.a. from 2010 until 2020,
- Carbon-neutral growth starting 2020,
- 50 % reduction of net-CO_2 emissions until 2050, compared to 2005.

In 2017, the IATA reported that the first goal was, until then, "surpassed" [6]. In 2019, the IATA states they are "on track" to reach the first goal [3]. The IATA expects that, especially for long-haul aircrafts, liquid fuels will be required at least for the next 50 years [7]. Hence, to reach the latter two goals, large amounts of Sustainable Alternative Fuels (SAF) will be required [7]. Besides biomass-based fuel production routes, synthetic hydrocarbons can be obtained from renewable electricity (e.g. from wind and solar power) in a Power-to-Liquid (PtL) process [4]. According to the International Civil Air Transport Association (ICAO), the PtL process via Fischer-Tropsch (FT) synthesis should be considered as a measure to reduce GHG emissions [4]. Since 2009, FT synthesized isoparaffinic kerosene (FT-SPK) can be added with up to 50% as drop-in jet fuel [4]. For PtL jet fuel Schmidt *et al.* estimate a reduction of 70 % to > 95 % of specific GHG emissions in comparison to conventional jet fuel [8].

* Corresponding author.
E-mail addresses: Sandra.Adelung@dlr.de (S. Adelung), Simon.Maier@dlr.de (S. Maier), Ralph-Uwe.Dietrich@dlr.de (R.-U. Dietrich).

https://doi.org/10.1016/j.seta.2020.100897
Received 27 July 2020; Received in revised form 12 October 2020; Accepted 25 October 2020
Available online 13 November 2020

Basic process description

The production of liquid fuels from renewable electricity has been previously studied e.g. by [8–15], who investigated different process designs for example different strategies for using the tail gas, different hydrogen and carbon monoxide production routes and different FT reactors. [13,15] have studied similar PtL process configurations as described in this work. Vázquez *et al.* give insight on the performance of their PtL bench-scale plant SOLETAIR and state the operating conditions of each unit [15]. They analyze the process for further improvement in a theoretical study [15]. The pilot plant has a hydrogen efficiency (based on the overall FT products) of 30.8 % and a carbon efficiency of 59.5 % [15]. König *et al.* set up a PtL process model and evaluate the process for a fixed set of unit assumptions [13]. They calculate a PtL-efficiency of 43.3 % and a carbon efficiency of 73.7 % [13]. In comparison, the pilot plant lacks utilization/recycling of the tail gas, which probably explains the higher carbon efficiency in [13].

Fig. 1 shows one possible process configuration to produce synthetic hydrocarbons from renewable electricity. Carbon dioxide can be recovered from different point sources like steel factories, cement plants, power plants, or via direct air capture. As water and CO_2 are very stable molecules, the production of more reactive hydrogen and carbon monoxide requires a significant amount of energy. In the depicted approach, first the liquid water is split to form hydrogen via electrolysis (i) and second the CO_2 is activated to form CO in a reverse water-gas shift reaction (ii). The heat for the rWGS unit is provided by burning gaseous products from the product separation. In addition to the rWGS reaction itself, different side reactions may occur in the rWGS unit (see 1.3).

$$H_2O_{(l)} \rightarrow H_2 + 0.5\ O_2 \quad \Delta_R H^0 = 285\ \mathrm{kJ/mol} \tag{i}$$

$$CO_2 + H_2 \rightleftharpoons CO + H_2O_{(g)} \quad \Delta_R H^0 = 41\ \mathrm{kJ/mol} \tag{ii}$$

$$CO + 2\ H_2 \rightarrow (-CH_2-) + H_2O_{(g)} \quad \Delta_R H^0 = -152\ \mathrm{kJ/mol} \tag{iii}$$

The syngas is further converted in the exothermic FT reaction (iii) into a broad range of hydrocarbons. Long chained hydrocarbons are cracked in a hydrocracker to increase the output of the desired chain length for fuel production ($<C_{22}$). Gaseous products and unreacted educts are recycled to increase the carbon efficiency of the process (further information on the recycles see chapter 2).

To maximize the energetic efficiency, matching rWGS and FTS process parameters are required in order to maximize the production of desired liquid fuel, by minimizing side reactions and reusing unavoidable by-products. Optimal process parameters cannot be found on a unit-by-unit optimization basis, but only by adjusting all parameters of the entire PtL process simultaneously. Additionally, the selection of different technologies might lead to different optimum rWGS operating conditions. The Fischer-Tropsch synthesis can, for example, be conducted in a slurry reactor or a fixed bed reactor with different kinds of catalysts and at different operating conditions, e.g. temperatures (high and low temperature FTS) [16]. This will affect the FTS boundary conditions (required feed composition in terms of H_2/CO ratio and inert gas content) as well as the performance of the FTS (CO conversion and hydrocarbon product distribution). Hence, different FT reactor types may influence the stream properties in the PtL process significantly. Consequently, different FT reactor types may lead to a different set of optimum rWGS operation conditions.

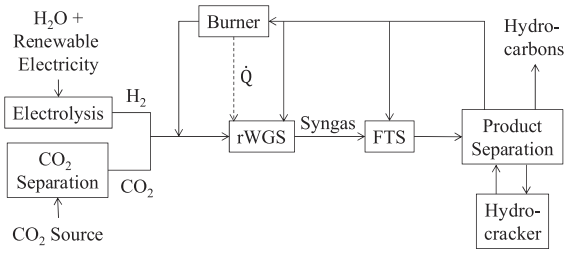

Fig. 1. Basic process scheme of the Power-to-Liquid process via Fischer-Tropsch synthesis (FTS) and reverse water-gas shift reaction (rWGS), including recycles to increase the carbon efficiency.

Different rWGS operating conditions have been applied in the literature. [13] and [15] have studied similar PtL process configurations as described in this work. König *et al.* assume $T_{rWGS} = 900\ ^\circ C$ and $p_{rWGS} = 25$ bar ($p_{FTS} = 25$ bar) in their process model [13]. Vázquez *et al.* operate their pilot plant at 850 °C and 1–5 bar [15]. However, they expect an improvement of energetic efficiency, if the rWGS reactor is operated at FT pressure level ($p_{FTS} = 20$–30 bar) [15]. A comparison of the energy efficiencies in [13] and [15] does not bring clarification which operating conditions are superior as they are additionally affected by other varying assumptions. To compare different rWGS operating conditions, constant boundary conditions, process unit assumptions and process configuration assumptions are required. To the author's knowledge, no systematic studies have been published on the influence of different rWGS operating conditions on the overall Power-to-Liquid process efficiency.

Syngas production – thermodynamics

The task of the rWGS unit is to produce carbon monoxide for the subsequent FT synthesis. The rWGS operating conditions affect the tail gas recycle and consequently the rWGS feed (compare Fig. 1). In addition to the rWGS reaction (ii), reactions involving methane and carbon may occur in the syngas reactor. Methane is formed in the FT reactor and can be formed or reformed in the rWGS unit depending on the rWGS operating conditions and the rWGS feed composition. The methane reforming reactions (iv)-(vi) are endothermic and thus methane reforming is thermodynamically favored at higher temperatures [17]. From the stoichiometry of reaction (iv)-(vi) follows that decreasing the pressure shifts the equilibrium to the right side and thus leads to lower a methane concentration in the product. Hence, to maximize the CO formation in the rWGS reactor, low pressures and high temperatures are required.

$$CH_4 + H_2O \rightleftharpoons 3\ H_2 + CO \quad \Delta_R H^0 = 206\ \mathrm{kJ/mol} \tag{iv}$$

$$CH_4 + 2\ H_2O \rightleftharpoons 4\ H_2 + CO_2 \quad \Delta_R H^0 = 165\ \mathrm{kJ/mol} \tag{v}$$

$$CH_4 + CO_2 \rightleftharpoons 2\ H_2 + 2\ CO \quad \Delta_R H^0 = 247\ \mathrm{kJ/mol} \tag{vi}$$

Carbon formation is an unwanted side reaction. It can lead to a shutdown of the whole unit due to break-up of the catalyst particles, blocking of active sites and encapsulation of the pellets [17]. Carbon formation may occur in the rWGS reactor via equation (vii)-(ix) [17]. Carbon formation due to Boudouard reaction (viii) is thermodynamically favored at low temperature and elevated pressure whereas methane pyrolysis (vii) is favored at high temperature and low pressure. Hence, carbon formation can occur at very different operating conditions.

$$CH_4 \rightleftharpoons 2\ H_2 + C \quad \Delta_R H^0 = -75\ \mathrm{kJ/mol} \tag{vii}$$

$$2\ CO \rightleftharpoons CO_2 + C \quad \Delta_R H^0 = 172\ \mathrm{kJ/mol} \tag{Viii}$$

$$H_2 + CO \rightleftharpoons H_2O + C \quad \Delta_R H^0 = 131\ \mathrm{kJ/mol} \tag{ix}$$

It has to be pointed out that carbon formation cannot be ruled out only by assessing the equilibrium composition, as local concentrations and temperatures may still lead to high local carbon formation affinities [17]. Hence, to rule out carbon formation, further assessment would be required.

Although the rWGS feed composition changes with different rWGS

operating conditions, the general influence of pressure and temperature is shown in Fig. 2 and Fig. 3 for a fixed feed composition. The temperature dependent equilibrium composition is calculated in Aspen Plus® at 5 bar for a constant H_2/CO_2 ratio of 2 and for a molar feed stream of 1 mol/s. The resulting gas composition and the carbon formation rate are shown in Fig. 2. The CO content increases monotonously with the temperature because all CO forming reactions are endothermic. Methane formation is favored at low temperature (Equation (iv)-(vi)). The carbon formation rate decreases with increasing temperature until it becomes negligible. Consequently, the exothermic reactions (Equation (viii) and (ix)) are critical for carbon formation.

The CO yield Y_{CO} and CO selectivity S_{CO} are calculated as follows:

$$Y_{CO} = \frac{\dot{n}_{CO,out}}{\dot{n}_{CO2,in}} \quad (x)$$

$$S_{CO} = \frac{\dot{n}_{CO,out}}{\dot{n}_{CO2,in} - \dot{n}_{CO2,out}} \quad (xi)$$

The CO yield expresses the overall CO production from CO_2, whereas the selectivity is a measure for occurring side reactions. Fig. 3 shows the influence of pressure and temperature, for a constant H_2/CO_2 ratio of 2, on the CO yield and CO selectivity. Both increase with increasing temperature and decreasing pressure due to decreasing methane formation. Hence, higher temperatures are required for the same CO selectivity/yield when the pressure is increased. In the methane forming temperature range ($S_{CO} < 1$), the temperature dependency is very pronounced. Once the CO selectivity approaches unity, the temperature dependency on the CO yield is decreased. In this temperature range only the rWGS reaction occurs. In conclusion, minimizing pressure and maximizing temperature leads to higher CO yield/selectivity. As has been pointed out in the beginning of this section, the CO yield affects the tail gas recycle properties. Different tail gas properties lead to different split ratios to the burner, rWGS and FTS (compare Fig. 1), and hence, affect the whole process operation control.

Aim of this work

Different authors have applied different rWGS operating conditions in their PtL processes (see Chapter 1.2). However, no systematic study can be found in the literature on the selection of the rWGS operating conditions within a PtL concept. The aim of this work is to assess the impact of different operating conditions (pressure and temperature) in the rWGS reactor on the overall PtL process performance. Due to the different recycles in the PtL process (see Fig. 1), determining the optimum rWGS operating conditions is not straightforward. Changes in

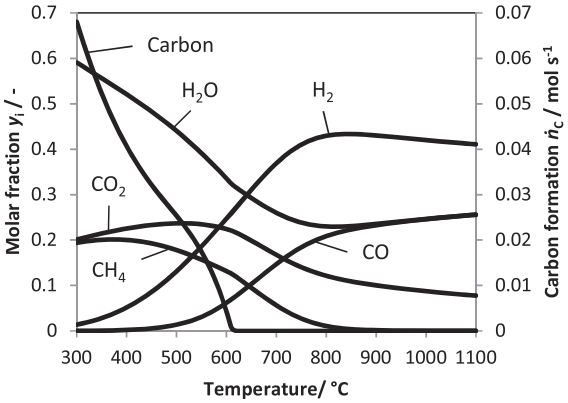

Fig. 2. Molar gas composition y_i and carbon formation rate $\dot{n}_C$ (graphite) for 300–1100 °C and 5 bar at thermodynamic equilibrium. Feed: 1 mol/s, $H_2/CO_2 = 2$.

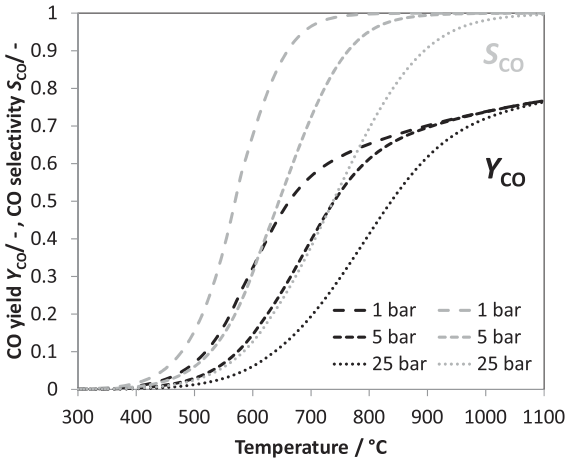

Fig. 3. CO yield (Y_{CO}) and CO selectivity (S_{CO}) at thermodynamic equilibrium for 300–1100 °C, 1–25 bar with an exemplary molar feed of $H_2/CO_2 = 2$. Increasing temperature and decreasing pressure leads to higher CO yields and CO selectivities.

rWGS pressure and temperature lead to changes in rWGS product distribution. This affects the recycle properties and thus, the split ratios towards FTS, burner and rWGS. For example, higher methane content in the rWGS product leads to higher recycling rates to the rWGS, which may affect the heat duty of the burner and consequently the fuel demand. The different influences lead to a set of favorable rWGS operating conditions. The objective of this work is to give an insight into the different correlations and to identify the best suited rWGS operating conditions to optimize the overall process performance. The process performance is investigated regarding:

- H-/C- efficiency: Amount of hydrogen from water/ carbon from CO_2 required for the fuel production.
- PtL-efficiency: Amount of electrical energy required to produce the desired liquid hydrocarbons.
- Pinch analysis: Assessment of heat integration possibilities.

In order to see how the optimum operating conditions are affected by the modelling assumptions, a sensitivity analysis is conducted.

Methodology

In the following chapter the modelling assumptions are defined. Chapter 2.1 describes the flowsheet and constraints in the general modelling approach. Chapter 2.2 deals with the assumptions of each process unit. In chapter 2.3 additional processing of the simulation results in Aspen Plus® using DLR's techno-economic process evaluation tool (TEPET) is explained. If not stated otherwise, temperature T and pressure p represent the temperature and pressure at the outlet of the rWGS reactor.

General modelling assumptions

The process is modelled in Aspen Plus®. The equation of state Peng-Robinson with Boston-Mathias modifications (PR-BM) is used, which is common for oil and gas production as well as hydrocarbon separation [18]. Chemical species involved in the model are H_2, CO, CO_2, H_2O, N_2, O_2 and alkanes (C_1-C_{30}, C_{32} representing C_{31}-C_{35}, C_{36} representing C_{36+}). Carbon formation in the rWGS reactor is not only affected by the thermodynamic equilibrium composition of the gas phase. The choice of catalyst as well as the concentration and the temperature profiles in the

actual reactor set-up affect the carbon formation, additionally [17]. It is beyond the scope of this work to investigate this in detail and to conclude whether carbon formation occurs. Thus, carbon is not included as a possible product.

The flowsheet is depicted in Fig. 4. The plant size is approximated to process the CO_2 emissions of an average German cement plant (~35.6 t_{CO2}/h calculated from [19]). In a first round of evaluation (p_{rWGS} = 1 bar, T_{rWGS} = 725 °C), the required hydrogen amount is calculated to 6 t_{H2}/h. It is worth mentioning, that this plant size requires a renewable base load power of 302 MW_{el} (see chapter 2.2 *Water electrolysis*) or 2.6 TWh p.a., which equals 0.56% of the installed wind power capacity (54 GW_{el} [20]) and 2 % of the wind power production in Germany in 2019 (131.8 TWh p.a. [20]). Although no water electrolyzers are in operation at this scale, chlor-alkali electrolysis is already available at large scale (typically 30–150 MW_{el} [21]), providing basic electrochemical know-how for large scale alkaline electrolysis [22]. Thyssenkrupp Industrial Solutions AG for example states, they could provide 10–20 MW_{el} modules (alkaline electrolysis) for a 100 MW_{el} plant and build 600 MW_{el} capacity each year [22]. In the following studies the hydrogen feed is kept constant, while the CO_2 feed varies with different rWGS operating conditions. The CO_2 feed is controlled to provide a constant molar ratio of H_2/CO = 2 in the feed of the FT reactor.

The aim is to produce syncrude for transportation fuels, especially targeting the kerosene and diesel range (C6-C21) [23]. To maximize the carbon efficiency, all gaseous components from the product separation are recycled. This recycle stream is split (S-1) as follows:

- The recycle to the FTS (Rec-FTS) is regulated to dilute the FT feed to have a constant inert gas content of 50 mol% (see chapter 2.2 *Fischer-Tropsch Synthesis*). Inert gas components are assumed to be all molecules except H_2 and CO.
- The recycle to the burner (Rec-Burn) is controlled to provide sufficient fuel and hence heat for the rWGS reactor.
- Remaining recycle gas is sent back to the rWGS (Rec-rWGS).

The flue gas from the burner is split (S-2) into three streams:

- The flue gas recycle to the burner is controlled to have a constant burner outlet temperature of 1200 °C [24,25].
- To account for impurities of the feed gases, a constant N_2 feed of 0.42 t/h is added to the hydrogen feed stream. This equals 0.36 vol-% of impurities based on the input of H_2, O_2 and CO_2. The overall impurity concentration is calculated with gas purities of 2.8 for H_2 and O_2 [26] and 2.0 for CO_2 [27]. The purge stream is controlled to have no accumulation of N_2 in the system.
- The remaining gas is sent back to the rWGS.

An overall pressure drop of 3 bar is assumed and implemented as a valve (V-1) in the recycle stream. The compressors are implemented as 3-staged compressors with an isentropic efficiency of 72 % and 100 % mechanical efficiency [28].

Unit description

CO_2 capture

Details on post combustion capture of CO_2 from cement plants can be found in [27]. Monoethanolamine (MEA) absorption is chosen, as it is a state-of-the-art technology (high maturity) for CO_2 capture [27]. MEA scrubbing is used in small plants producing up to 16.7 t CO_2/h for food, beverages and the chemical industry [27]. The downside of the MEA absorption process is a rather high thermal energy demand compared to other solvents under development [27]. As the exothermic FT reaction provides an excess of thermal energy, this energy can be used to provide the heat for CO_2 capture. The thermal energy demand for MEA absorption is 3.8 MJ_{th}/kg $CO_{2,\ captured}$ and the electricity required is 0.14 MJ_{el}/kg $CO_{2,\ captured}$ [29]. The desorption temperature is assumed to be constant at 120 °C for pinch analysis [29]. The CO_2 recovery ratio is 90 % [29] and the MEA outlet conditions of the stripped CO_2 after condensation are 1 bar and 25 °C [27].

Water electrolysis

Water electrolysis can be conducted in alkaline, proton exchange membrane (PEM) and solid oxide electrolysis cells, which are available at different levels of maturity [30]. PEM electrolysis is commercially available, but not in large scale applications [30]. However, PEM seems best suited for intermittent operation [30], which is crucial in most renewable electricity cases. Current PEM system efficiencies are in the range of 4.2–6.6 kWh_{el}/m^3_{H2} [30,31]. In this work an intermediate electrolysis efficiency of η_{LHV} = 66.67 % (≙ 4.47 kWh_{el}/m^3_{H2}) is assumed. The hydrogen feed is constant at 6.048 t/h (25 bar, 25 °C) for all scenarios (see chapter 2.1). Hence, 302 MW_{el} are required for the electrolysis. Current stack sizes range up to 2–3 MW_{el} [32]. Thema *et al.* reviewed the status-quo on existing Power-to-Gas plants in terms of hydrogen and methane production from electricity. In early 2019, the globally active Power-to-Gas projects comprise an electrical power input of 38.6 MW_{el} (electrical input for electrolysis) [33]. Hence, 8 times the globally produced hydrogen from electricity would be required for this plant. However, work is ongoing to bring the technology to the > 100 MW scale [33].

CO_2 activation

The rWGS reactor is modelled as a Gibbs reactor (Gibbs minimization) and thereby assuming thermodynamic equilibrium at the

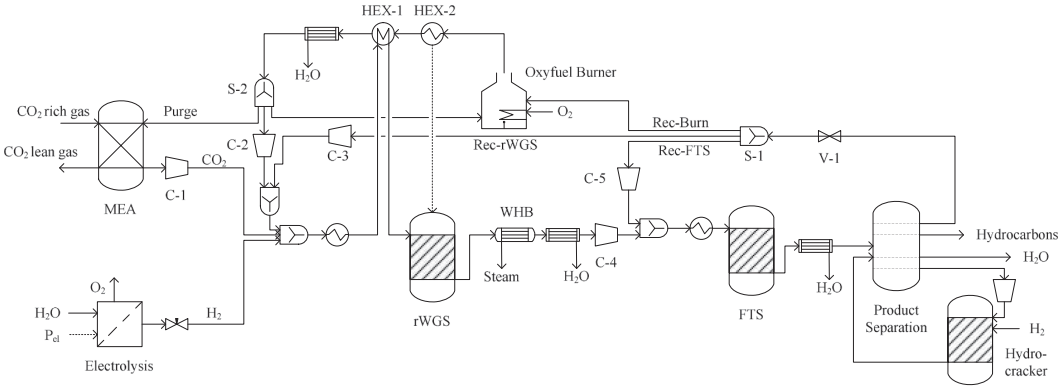

Fig. 4. Flowsheet of the PtL model in Aspen Plus® including monoethanolamine absorption (MEA), waste heat boiler (WHB), compressors (C), splits (S), heat exchangers (HEX) and valves (V).

respective outlet temperature and pressure of the reactor [13]. The operating conditions are varied from 550 to 950 °C and 1–25 bar (see chapter 3.1). It is assumed that the product stream cannot be used for preheating the feed stream, as its properties are prone to metal dusting (metal dusting occurs at high CO concentration and 450–800 °C [34]). Alternatively, the product gas is used in a waste heat boiler (WHB) to produce high pressure steam. In a WHB the heat transfer resistance is mainly at the product gas side and the wall temperature is close to the steam temperature [34]. With these low wall temperatures the risk of metal dusting is rather low [34].

Oxyfuel burner

To decrease the amount of inert gas in the process, the by-product oxygen from the electrolysis is used in an oxyfuel burner (instead of combustion with air). The burner, operated at 1 bar, provides the heat for the endothermic rWGS reactor. Complete combustion (stoichiometric reactor) is assumed with $\lambda = 1$. The cold flue gas is recycled back to the burner to have a constant, adiabatic, outlet temperature of $T_{\mathrm{Burn}} = 1200$ °C [24,25]. A flameless oxyfuel burner, providing 40 MW_{th}, is in operation in Sweden [25]. This configuration is well in line with the thermal energy demand in this work (compare Fig. 8). The outlet temperature of HEX-2 ($T_{\mathrm{HEX\text{-}2}}$ in °C) is calculated from the rWGS reactor outlet temperature (T_{rWGS} in °C) according to:

$$T_{\mathrm{HEX-2}} = T_{\mathrm{rWGS}} + \Delta T \tag{xii}$$

$$\Delta T = 340\ ^{\circ}\mathrm{C} - \frac{T_{\mathrm{rWGS}}}{5} \tag{xiii}$$

Equation (xiii) is approximated from tubular steam-methane reforming:

- Reformer exit temperature: 700–950 °C [17] (here: T_{rWGS}) and the according
- Flue gas exit temperature: 900–1100 °C [17] (here: $T_{\mathrm{HEX\text{-}2}}$)

The flue gas leaving the combustion chamber (HEX-2) is then further used to heat the rWGS feed in a countercurrent heat exchanger (HEX-1), with a $\mathrm{Hot_{out}}$ - $\mathrm{Cold_{in}}$ temperature difference of 50 K (U-value = 50 W/m^2K [35]). In some cases this specification leads to a temperature cross in the heat exchanger. The specification is then set to 50 K for the temperature difference of $\mathrm{Hot_{in}}$- $\mathrm{Cold_{out}}$ instead. As the CO concentrations in the flue gas and rWGS feed are low, minor risk for metal dusting in HEX-1 is expected.

Fischer-Tropsch synthesis

A tubular fixed bed reactor with cobalt catalyst, only alkanes as product [16], is assumed. This kind of reactor is, for example, used in the GtL plant in Bintulu, Malaysia [36]. This plant uses Shell Middle Distillate Synthesis (SMDS) technology and is about 5 times of the size of the reactor in this work [36]. However, the fixed bed reactor is comparably easy to scale [37]. The rWGS product stream is cooled (40 °C) to separate most of the water as steam may cause deactivation on cobalt catalysts [38]. The Fischer-Tropsch reactor is modelled as a stoichiometric reactor at 25 bar and 220 °C [39]. The H_2/CO ratio is fixed to 2 [36]. Under these conditions the chain growth probability α is calculated according to equation (xiv) to 0.839 [40]. The methane selectivity is $S_{\mathrm{CH4}} = 0.161$ [40].

$$\alpha = \frac{1}{1 + 0.0567\left(\frac{c_{H2}}{c_{CO}}\right)^{1.76} \exp\left(3620\ \mathrm{K}\left(\frac{1}{493.15\ \mathrm{K}}\right) - \left(\frac{1}{T}\right)\right)} \tag{xiv}$$

The CO conversion is assumed to be 40 % [41] and the inert gas share is fixed, conservatively, to 50 % [42] to prevent catalyst deactivation, decreasing selectivity and thermal runaway due to strong non-isothermal behavior [39].

Hydrocracker

To increase the yield towards liquid fuels, the heavy hydrocarbons (liquid fraction at 150 °C, 25 bar) are fed to a hydrocracker. The required hydrogen amount is calculated to satisfy the H/C ratio of the alkanes at the outlet of the hydrocracker. The reactor is modelled as a yield reactor at 35 bar and 370 °C [43]. A polynomial yield curve is approximated with a combination of yields for C_1-C_{10} taken from [44] and C_{10}-C_{30} taken from [43].

Product separation

In a first flash (150 °C, 25 bar) the heavy hydrocarbons are separated from the FT product stream and sent to the hydrocracker. The product from the hydrocracker is then added to the product separation, which consists of 8 flashes at 4 fixed temperatures (110 °C, 70 °C, 40 °C, −15 °C) and 2 pressures (25 bar, 1 bar) [13]. The main products of the separation are water, recycling gases (gaseous compounds at: 110 °C, 70 °C, 40 °C, −15 °C at 1 bar and −15 °C at 25 bar) and the desired synthetic hydrocarbons.

Validity of the process model

To our knowledge, there is no experimental data available in the literature for the exact same configuration as described in this work. Hence, the validation of the proposed overall PtL process concept is still pending. For the assessment of the entire PtL process, valid models for the FT reactor and for the rWGS reactor including the burner unit are essential. The FT model used in this study was proposed and fitted for a broad range of FT operating conditions by [40]: $T_{\mathrm{FTS}} = 470$–530 K, $p_{\mathrm{FTS}} = 12$–36 bar, syngas ratio in the bulk = 0.1–3.0, H_2/CO = 1–3. The FT operating conditions in this work are within the given boundaries for the fitted model. Further information on the validity of the FT model results can be found in [40]. The sensitivity of the rWGS reactor model on changing rWGS operating conditions is of high importance in this work. Thermodynamic equilibrium is assumed, as has been applied in previous studies [13,38]. In [45], kinetic experiments are conducted using a monolithic, noble metal catalyst at 1.5 bar for different H_2, CO_2 and CH_4 feeds at different temperatures (600–900 °C) and at a high residence time. The equilibrium composition calculated in Aspen Plus® matches the experimental results, if carbon formation is suppressed in the simulation [45]. The calculation of the burner temperature is based on empirical data for methane steam reforming. Although this seems reasonable, as both reactor types show a lot of similarities, a more detailed model or experimental validation would be beneficial to proof this assumption.

TEPET

The Aspen Plus® simulations are supported by DLR's 'Techno-Economic Process Evaluation Tool' (TEPET) [46]. Apart from the possibility to evaluate process economics, details see [46], this tool improves the handling of technical evaluations based on Aspen Plus® simulations. With TEPET's 'simulation control' it is possible to vary parameters in Aspen Plus®, for example operating conditions of a unit, while saving the results of each simulation run. This increases efficiency in data collection. As there are different recycles within this Aspen Plus® simulation, TEPET's 'open loops' is used to speed up convergence, even under severe changes in operating conditions. Automatic pinch analysis is carried out in TEPET's 'heat integration', using T-H curves derived from Aspen Plus®. Automatic heat integration allows estimating the amount of required cooling media or possible steam production from excess thermal energy without extensive heat exchanger networks.

Results and discussion

Chapter 3.1 to 3.5 deal with the base case as described in chapter 2. Chapter 3.1 addresses the limitations of the operating window of the

rWGS in the PtL process. In chapter 3.2 and 3.4 the influence of the rWGS operating conditions on the product output and Power-to-Liquid efficiency is analyzed and correlations are outlined in detail. Chapter 3.3 covers the carbon and hydrogen efficiency and chapter 3.5 gives insight into different heat integration options for one specific case. In chapter 3.6 sensitivity analysis is conducted to analyze the effect of the assumptions on the optimum operating conditions.

Operating window

The investigated rWGS pressure range is 1–25 bar. The lower pressure boundary of 1 bar is selected because lower pressure increases the CO-yield (see chapter 1.3). To reduce the required energy for compression, the upper pressure boundary is equal to the FTS operating pressure (25 bar). The investigated rWGS temperature range is between 550 and 950 °C. The maximum temperature is selected due to material considerations. The lower temperature boundary is restricted by the assumption of 50 mol% inert gas content in the FTS feed. The recycle to the FTS (Rec-FTS) varies strongly for different rWGS operating conditions (Fig. 5). With decreasing rWGS temperature and increasing rWGS pressure the methane content in the rWGS product stream increases. Hence, less gas is recycled back to the FTS (Rec-FTS) to provide the constant inert gas content in the feed of the FTS. At a certain temperature the recycle ratio to the FTS approaches zero. Below this temperature, the inert gas content exceeds the fixed molar share of 50 %. Thus, for 1 bar, 5 bar, 10 bar and 25 bar, the respective rWGS minimum temperature is 581 °C, 670 °C, 714 °C and 780 °C.

Product output

The product output $\dot{m}_{\mathrm{Hydrocarbons}}$ is the lumped hydrocarbon output of all liquid fractions (see stream "Hydrocarbons" in Fig. 4). An example for the hydrocarbon product distribution is shown in Fig. 6.

The dependency of the product output on the rWGS operating conditions is shown in Fig. 7. Starting at low temperature, the product output increases until it reaches a maximum. The maximum output (10.21 t/h) is obtained at 1 bar and 725 °C. Increasing the temperature further, shows first a slight decrease in product output, until the product output decreases again significantly. Streams leaving the system boundaries are water, purge gas and hydrocarbon product. Higher hydrocarbon product yields are achieved when purge gas and water production decrease. Conclusively, the product output correlates inversely with the water production and purged gas. Steam from combustion,

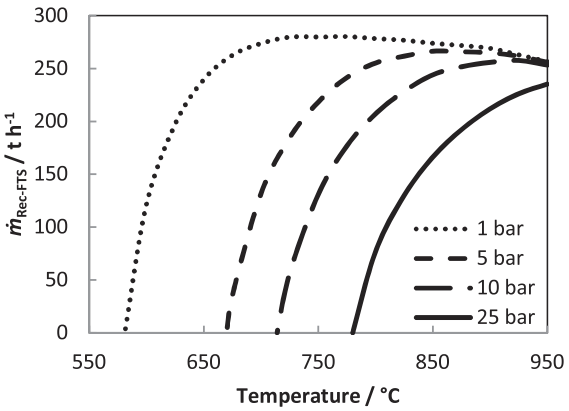

Fig. 5. Mass flow rate of the recycle stream from the product separation to the FTS $\dot{m}_{\mathrm{REC-FTS}}$ for different rWGS pressures and temperatures. Pressure dependent lower rWGS boundary temperature, where FTS recycle stream approaches zero.

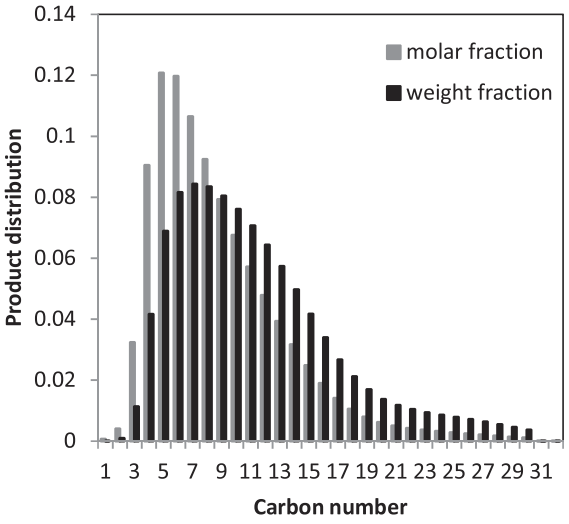

Fig. 6. Hydrocarbon product distribution (stream "Hyrocarbons" in Fig. 4) at $p_{\mathrm{rWGS}} = 5$ bar and $T_{\mathrm{rWGS}} = 825$ °C.

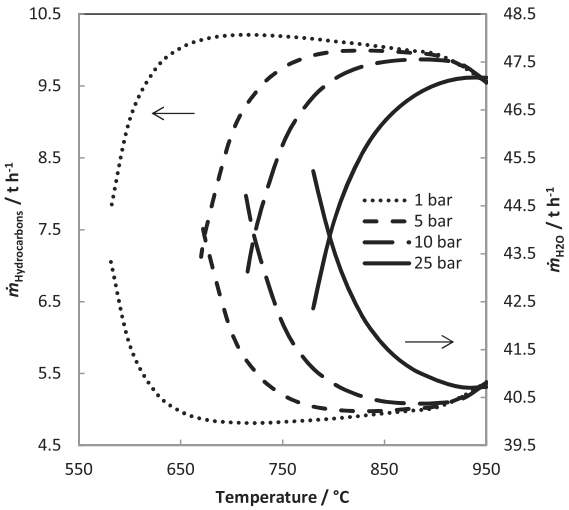

Fig. 7. Lumped hydrocarbon product output $\dot{m}_{\mathrm{Hydrocarbons}}$ and water output $\dot{m}_{\mathrm{H2O}}$ for different rWGS pressures and temperatures. The hydrocarbon output correlates with the water exiting the system boundaries.

rWGS reaction and FTS is condensed and separated from the process (compare Fig. 4). Hence, hydrogen forming steam is no longer available for the hydrocarbon production. Fig. 7 shows the amount of water $\dot{m}_{\mathrm{H2O}}$ exiting the system boundaries. It is evident, that the product output correlates inversely with the amount of water produced. In contrast, CO_2 (e.g. from CO combustion) is recycled via MEA absorption. As 90 % of the purged CO_2 is recovered in the MEA unit, the amount of purge gas has only minor influence on the product output.

The overall water production depends on:

- the heat duty $\dot{Q}_{\mathrm{rWGS}}$ required for preheating and for the endothermic reaction in the rWGS reactor,
- the composition (atomic hydrogen content β) of the fuel gas recycled to the burner (Rec-Burn) and

- the recuperation efficiency of HEX-1.

The heat demand of the rWGS reactor is shown in Fig. 8. It is the summation of heat required for preheating from 450 °C to rWGS reaction temperature plus the heat required for the endothermic reaction. For a given pressure there is an optimum temperature with minimum heat demand. Above this optimum temperature the heat demand increases slightly due to the increase in $\Delta T = T_{\mathrm{rWGS,\ out}} - T_{\mathrm{rWGS,\ in}}$. Decreasing the temperature leads to higher methane concentrations in the recycle and therefore higher recycle rates to the rWGS (Rec-rWGS). Hence, for temperatures lower than the optimum temperature, the heat demand increases due to a higher throughput that has to be heated up. The heat demand varies in the range of 28–49 MW_{th} and the minimum heat requirement is found at 625 °C and 1 bar.

Intuitively, higher heat demand leads to higher water production. However, for low and high rWGS temperatures the correlation between rWGS heat duty and overall water production shows deviations.

The combustion reaction of a hydrocarbon mixture is shown in equation (xv). From the stoichiometry of this reaction, it is evident, that a change in the recycle gas composition, thus burner fuel composition, influences the amount of water produced in the burner. For low rWGS temperatures the methane content in the recycle increases significantly, which leads to significant changes in burner fuel composition. This increase in methane content leads to an increase in β and consequently water production. Fig. 8 shows the atomic hydrogen content β for different rWGS pressures and temperatures. The higher methane content in the burner fuel leads to a prominent increase in water production at low rWGS temperatures, e.g. at 1 bar below 650 °C. Minimum β is found at 1 bar and 800 °C. As the minimum rWGS heat duty is obtained at 625 °C and the minimum β at 800 °C, the minimum overall water production is achieved between these temperatures at 725 °C.

$$C_\alpha H_\beta O_\gamma + \left(\alpha + \frac{\beta}{4} - \frac{\gamma}{2}\right) O_2 \rightarrow \alpha\, CO_2 + \frac{\beta}{2}\, H_2O \qquad \text{(xv)}$$

The heat exchanger preheating the rWGS feed with the flue gas (HEX-1) is specified to reach a temperature difference of 50 K for the Hot_{out}- $Cold_{in}$ streams (see chapter 2.2). For high temperatures (≥ 900 °C at 1 bar, 925 °C at 5 bar, 925 °C at 10 bar, 950 °C at 25 bar) this specification leads to a temperature cross in the heat exchanger. Under these rWGS operating conditions the heat exchanger is calculated to satisfy a temperature difference of 50 K for the Hot_{in}- $Cold_{out}$ streams. Consequently, the energy in the flue gas cannot be fully utilized, resulting in higher outlet temperatures of the hot stream and thus a higher thermal waste stream. Additional fuel is burned, as the flue gas is not fully recuperated, which leads to an increase in water production.

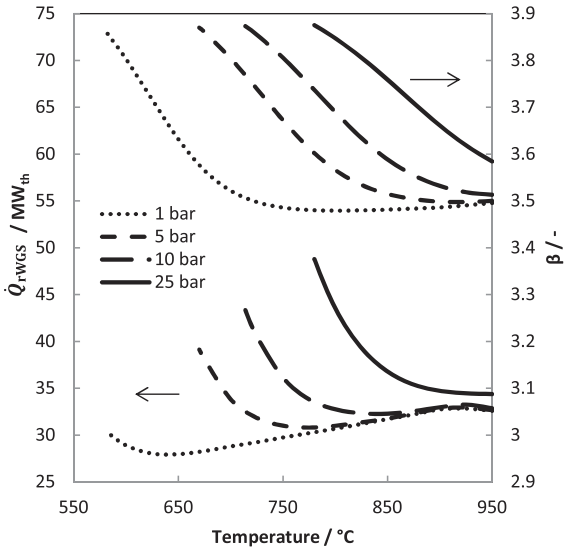

Fig. 8. Left: Heat demand of the rWGS unit $\dot{Q}_{rWGS}$ for different rWGS temperatures and pressures. Low temperatures lead to higher methane content in the recycle and thus higher recycle rates to the rWGS (Rec-rWGS). This increases the rWGS feed that requires heating up. Right: β (atomic hydrogen content in the recycle) as a function of rWGS temperature and pressure. Low temperatures lead to high methane content and thus higher β.

Carbon and hydrogen efficiency

Carbon enters the system boundaries as CO_2, flue gas from the cement plant ($\dot{n}_{C,\ Cement\ Plant}$), and leaves the system boundaries as hydrocarbon product ($\dot{n}_{C,\ Hydrocarbons}$), purge gas or dissolved in water. The amount of carbonaceous molecules dissolved in water is comparably low to the amount of carbon in the hydrocarbon product and purge gas. For calculating the carbon efficiency, the carbon incorporated in the hydrocarbon product is set in relation to the amount of carbon from the cement plant (equation (xvi)):

$$\eta_C = \frac{\dot{n}_{C,\ Hydrocarbons}}{\dot{n}_{C,\ Plant}} \qquad \text{(xvi)}$$

As both, the flue gas from the cement plant and the purge gas, are processed by the MEA unit, the performance of the MEA absorption has a large influence on the carbon efficiency. The MEA recovery rate is independent of the rWGS operating conditions. 10 % of the CO_2 from the cement plant and purge gas cannot be recovered (as a recovery rate of 90 % is assumed in chapter 2.2). The carbon efficiency obtained equals η_C = 88 % (Fig. 9) and is not affected by changes in rWGS operating conditions. The carbon dioxide amount required from the cement plant is shown in Fig. 9. The CO_2 stream correlates directly with the product output (compare Fig. 7). Higher product output leads to an increase in $\dot{m}_{CO2,\ Cement\ Plant}$, as the H_2/CO ratio in the feed of the FTS is assumed to be constant. Overall, this leads to a constant C-efficiency.

The hydrogen efficiency is calculated according to equation (xix) from the atomic hydrogen amount in the hydrocarbon product

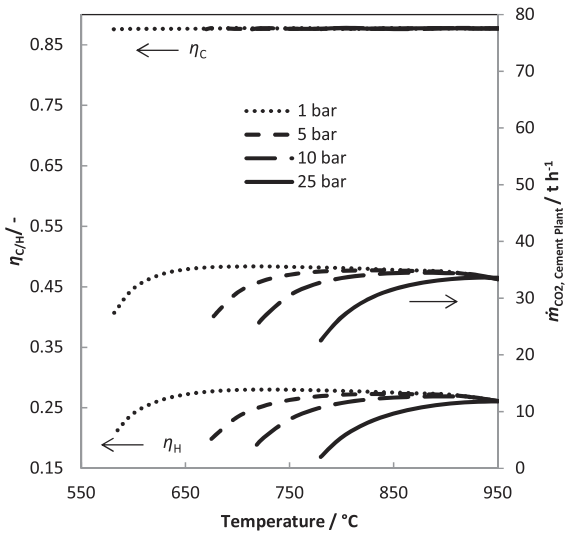

Fig. 9. Left: Hydrogen and carbon efficiency for different rWGS pressures and temperatures. η_H correlates inversely with the water production (compare Fig. 7). The carbon efficiency is not affected by the rWGS operating conditions. Right: CO_2 demand from the cement plant. The carbon dioxide demand correlates with the product output (compare Fig. 7).

($\dot{n}_{H,\ Hydrocarbons}$) and the atomic hydrogen amount in the electrolysis feed ($\dot{n}_{H,\ Electrolysis}$).

$$\eta_H = \frac{\dot{n}_{H,\ Hydrocarbons}}{\dot{n}_{H,\ Electrolysis}} \quad \text{(xvii)}$$

Hydrogen enters the system boundaries as water (feed to electrolysis) and leaves the boundaries as water (condensed steam) or hydrocarbon. As the hydrogen input is constant, the hydrogen efficiency (Fig. 9) correlates inversely with the water production (compare Fig. 7).

Power-to-Liquid efficiency

Electrolysis, MEA and compressors are the major contributors to the overall power consumption of the process. Hence, the Power-to-Liquid efficiency is calculated as follows:

$$\eta_{PtL} = \frac{\dot{m}_{Hydrocarbons}\ LHV_{Hydrocarbons}}{P_{Electrolysis} + P_{MEA} + P_{Compression}} \quad \text{(xviii)}$$

The efficiency is calculated from the lumped mass flow of the overall hydrocarbon output ($\dot{m}_{Hydrocarbons}$), the lower heating value of the overall hydrocarbon output ($LHV_{Hydrocarbons}$) and the electrical energy input for electrolysis ($P_{Electrolysis}$), MEA (P_{MEA}) and compression ($P_{Compression}$).

As the hydrogen input is constant in this study, the power demand for the electrolysis is constant (302 MW_{el}). The electricity demand for MEA absorption varies with the amount of $CO_{2,\ captured}$, between 1.0 and 1.55 MW_{el} (see Fig. 10). Hence, CO_2 capture has only a minor share of the overall electrical energy input. Compression work varies between 4 and 51 MW_{el} due to different gas flow rates and pressure levels. If the rWGS is operated at low pressure this increases the compression work in compressor C-4 (see Fig. 4). Operating the rWGS at 25 bar decreases the compression work, as the FTS and rWGS are operated at the same pressure level and thus no additional compression work is required. Decreasing the rWGS temperature leads to higher methane content and thus, higher recycling rates to the rWGS (Rec-rWGS). Therefore lower temperatures require more electrical energy for compression.

Fig. 11 shows the resulting PtL-efficiency at different rWGS temperatures and pressures. The PtL-efficiency varies between 25.4 % and 38.7 %. For a given pressure, there is a plateau, where the PtL-efficiency is only affected marginally by the rWGS temperature. The according

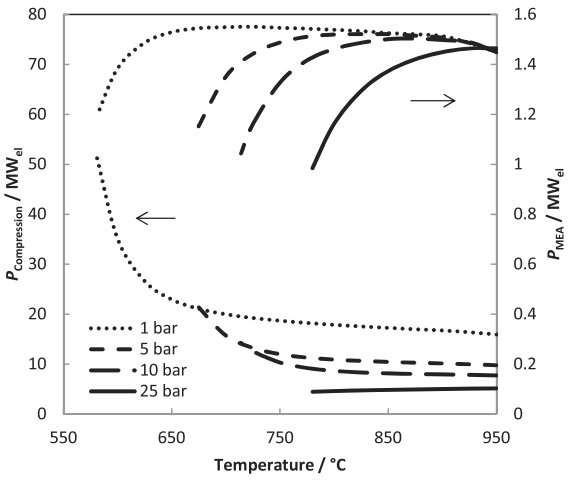

Fig. 10. Electricity demand required for compression $P_{compression}$ and monoethanolamine absorption P_{MEA} for different rWGS temperatures and pressures. P_{MEA} is comparably low to $P_{compression}$. $P_{compression}$ increases with decreasing pressure and temperature.

rWGS temperatures and pressures for a relative decrease of 1 % and 3 % PtL-efficiency are shown in Fig. 11 on the right side. The maximum PtL-efficiency is found at 5 bar and 825 °C:

$$\eta_{PtL}(5\ bar,\ 825\ ^{\circ}C) = \frac{2.77\ \frac{kg}{s} \cdot 43.85\ \frac{MJ}{kg}}{302\ MW + 1.5\ MW + 10.6\ MW} = 0.387$$

Analogous to the product output (compare chapter 3.2), the PtL-efficiency has an optimum temperature for a given pressure. However, the maximum product output is found at 1 bar and 725 °C (chapter 3.2) and the maximum PtL-efficiency is obtained at 5 bar and 825 °C. The increase in optimum pressure in terms of energetic efficiency corresponds to the higher compression work at lower pressures (compare Fig. 10). Hence, 5 bar is energetically favored over 1 bar. The higher optimum temperature from the energetic perspective is due to the increase in methane formation at higher pressure which requires higher temperatures for the same CO-yield.

Heat integration

Automated pinch analysis is conducted for all cases (see chapter 2.3). The pinch temperature difference is fixed to 10 K. Burner and rWGS reactor are not included in the pinch diagram as the thermal coupling is already performed in the Aspen Plus® simulation. One exemplary pinch analysis is shown in Fig. 12 for 5 bar and 825 °C (as this case has the maximum PtL-efficiency, see chapter 3.4). The diagram includes two curves: the summation of all hot streams ('hot stream'), which are available for heating or require active cooling, and the summation of all cold streams ('cold stream'), which require heating.

In this case, the heat from the exothermic FT reaction (39.5 MW_{th} at ~ 211 °C) is sufficient to provide enough heat for CO_2 absorption (31.6 MW_{th} at 120 °C). Below 100 °C active cooling is required (40 MW). As described in chapter 2.2, syngas leaving the rWGS reactor is cooled using a waste heat boiler. Most of this high temperature heat cannot be integrated in the process (20 MW_{th} at 370 °C-825 °C). One option to use this valuable high temperature heat is to produce electricity via a steam based Clausius-Rankine cycle 'SCR' (43 % efficiency, steam cycle modelled in Aspen Plus®). This scenario provides 15.8 MW_{el} and requires 1030 kg/s of cooling water ('CW'). The electricity regained from the Clausius-Rankine cycle can be used to decrease the power demand and hence increase the Power-to-Liquid efficiency:

$$\eta_{PtL,\ SCR} = \frac{\dot{m}_{Hydrocarbons}\ LHV_{Hydrocarbons}}{P_{Electrolysis} + P_{MEA} + P_{Compression} - P_{SCR}} \quad \text{(xix)}$$

This increases the PtL-efficiency from 38.7 % to 40.75 % (at 5 bar and 825 °C). Fig. 13 shows the efficiencies calculated with SCR for different rWGS pressures and temperatures. Compared to the PtL base case, the Clausius-Rankine cycle increases the PtL-efficiency by (ηPtL, SCR - η_{PtL} =) 1.6– 3.7 %. However, adding a Clausius-Rankine cycle to the PtL plant has yet to be proven to be economically beneficial. Another option to use the high temperature heat is high pressure steam (35.5 bar) production. The resulting 'cold stream' (at 5 bar and 825 °C) is shown in the pinch diagram in Fig. 12. This configuration produces 14.35 kg/s of steam and requires 906 kg/s cooling water.

Sensitivity studies

The findings in the previous subchapters result from the assumptions in chapter 2 (base case configuration). The assumptions described in chapter 2 are based on reasonable engineering guesses. Still, they may vary under different circumstances in a reasonable range. This might affect the overall optimum rWGS operating conditions. To investigate the influence of the most relevant assumptions on the optimum rWGS operating conditions, respective η_{PtL}, η_H, η_C, local sensitivity studies are conducted as depicted in Table 1.

Variables 1) and 2) do not influence the process streams and, thus, η_H

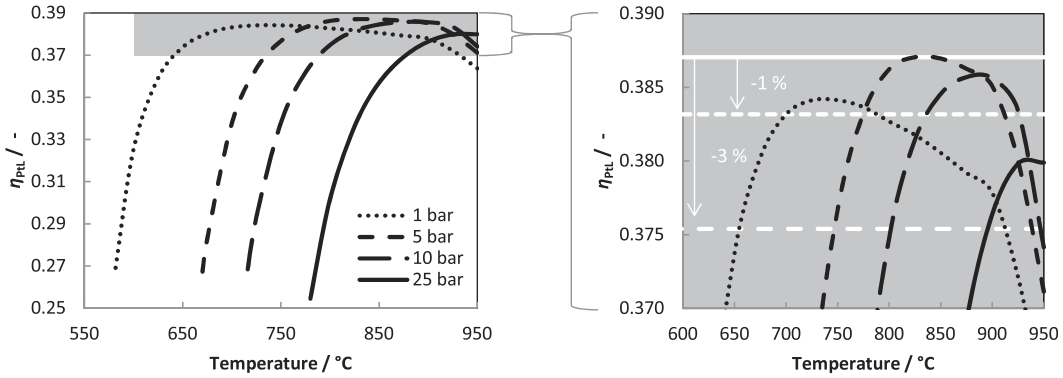

Fig. 11. Power-to-Liquid efficiency for different rWGS pressures and temperatures. Below and above a certain temperature, the PtL-efficiency decreases significantly.

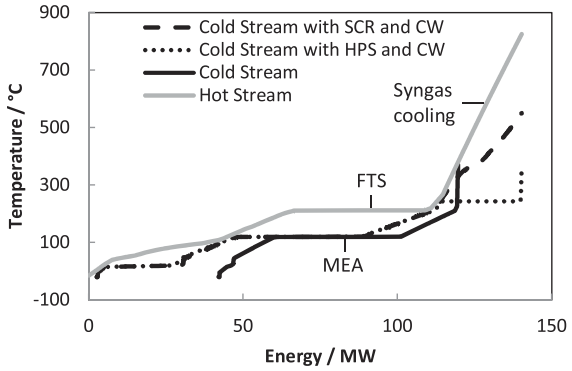

Fig. 12. Pinch analysis conducted at 825 °C rWGS temperature and 5 bar rWGS pressure. Major contributors to the "hot stream" are Syngas cooling and Fischer-Tropsch synthesis (FTS). The "cold stream" shows heat integration possibilities at high temperature. Thus, in one case a clausius-rankine cycle (SCR) and in a second case high pressure steam production (HPS) is integrated. Both cases include the cooling water demand (CW).

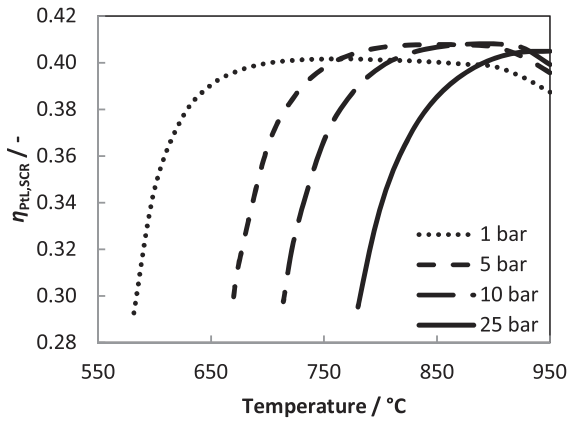

Fig. 13. Power-to-Liquid efficiency including clausius-rankine cycle at different rWGS pressures and temperatures. The PtL-efficiency can be increased by 1.6–3.7 % in comparison to Fig. 11.

Table 1
Variables for the sensitivity study related to the feed supply (1), 3)), rWGS + burner setup (4)-5)) and FTS performance (6)-9)). The α values are calculated with equation (xiv).

Variable	Min	Base	Max
1) $\eta_{Electrolysis,LHV}$ / -	0.6	0.667	0.7
2) $\eta_{Compression}$ / -	0.6	0.72	0.9
3) N_2 / t h^{-1}	0.042	0.42	–
4) ΔT_{HEX-1} / K	10	50	100
5) T_{Burn} / °C	1150	1200	1400
6) x / -	0.4	0.5	–
7) H_2/CO / (α/-)	1.8 (0.862)	2 (0.839)	2.2 (0.815)
8) T_{FTS} / (α /-)	210 (0.905)	220 (0.839)	225 (0.795)
9) X_{CO} / -	–	0.4	0.6

and η_C. However, they affect η_{PtL} directly as the electrolysis has a major share of the total energy input and the compression work has a significant effect on the optimum operating conditions (see chapter 3.4). The efficiency of the electrolyzer is varied between 57 and 47 kWh_{el}/kgH_2 [31], which equals $\eta_{Electrolysis,LHV}$ = 60–70 %. Varying the compressor efficiency can also be interpreted as a change in the overall pressure drop for a constant compressor efficiency. Variable 3) accounts for impurities in the feed streams (H_2, CO_2 and O_2) and may affect the process streams due to changes in partial pressures and hence rWGS product composition. As the base case has already been chosen conservatively, the N_2 feed is calculated for purities of 4.0 for H_2 and O_2 [26] and 3.0 for CO_2 [27]. Variables 4) – 5) influence the overall allothermal rWGS (rWGS + burner) configuration. They are prone to have a significant influence on the product output as they influence the heat duty of the burner. For example, decreasing the temperature difference in the heat exchanger HEX-1 will lead to an increase in heat transfer in HEX-1. Hence, the temperature of the rWGS feed stream increases and less thermal energy has to be provided by HEX-2. Thus, less fuel is consumed, which leads to lower water production and higher product output (compare chapter 3.2). Variables 6) – 9) represent changes in Fischer-Tropsch performance. The FTS temperature and the H_2/CO ratio in the FTS feed influence the chain growth probability α. Lower α leads to higher methane concentrations and hence more water production, which results in less product output (compare chapter 3.2). In addition, different H_2/CO ratios influence the CO_2 feed and hence all process stream properties. All FTS parameter have the ability to change the product distribution, which affects the recycle properties and consequently the product output.

Chapter 3.1 points out the lower rWGS temperature boundary, which is reached when the recycle to the FTS (REC-FTS) approaches zero. In contrast to that, an upper rWGS temperature boundary is found for specific cases marked with "u.b." in Fig. 15 and Fig. 16. In these cases the

recycle to the rWGS (Rec-rWGS) approaches zero and the inert gas content exceeds the fixed content of 50 mol%. Although it might be possible to operate the FTS with a higher reactants content than 50 %, these cases are marked as the upper temperature boundary, as they cannot be compared directly to the other cases.

Fig. 14 compares the deviation of the maximum PtL-efficiencies, calculated for the different variable values in Table 1, to the base case. The maximum PtL-efficiency is observed at $T_{rWGS} = 825$ °C and $p_{rWGS} =$ 5 bar for almost all variations, except for $H_2/CO = 2.2$. In this case the optimum is observed at slightly higher rWGS temperature (850 °C). The overall maximum PtL-efficiency is found at low FTS temperature $T_{FTS} =$ 210 °C ($\eta_{PtL} = 40.9\%$). In general, the PtL-efficiency increases with increasing $\eta_{Electrolysis}$, T_{Burn}, $\eta_{Compression}$, X_{CO}, x_{inert} and decreasing T_{FTS}, H_2/CO, $\Delta T_{HEX\text{-}1}$. The efficiency of the electrolyzer $\eta_{Electrolysis}$, the FTS temperature T_{FTS} and the H_2/CO ratio in the feed of the FTS reactor have the highest influence on the PtL-efficiency. Decreasing T_{FTS} and the H_2/CO ratio leads to an increase in chain growth probability. For longer chains, less water is produced per hydrogen atom integrated in the hydrocarbon product. This decrease in water production leads to the increase in PtL-efficiency. It should be mentioned that the model for α (equation (xiv)) does not account for differences in inert gas content. This seems reasonable, as the experimental results from [47] show only minor influence of the inert gas content on α. Impurities and X_{CO} are found to have only minor influence on the PtL-efficiency. However, it is worth noting that, in this work, α is independent of the CO conversion. In contrast, [48] state that the methane selectivity decreases with increasing CO conversion. They also state that the influence of the FT reactor temperature is larger than the influence of the CO conversion [48]. Hence, if the model was to include the X_{CO} and α correlation, we would expect an increase in PtL-efficiency, although the difference should not be as pronounced as for a lower FT temperature.

Fig. 15 shows the according Power-to-Liquid efficiencies for the different variables at varying rWGS pressures and rWGS temperatures. Evidently, different assumptions for the variables in Table 1 lead to different Power-to-Liquid efficiencies for a given rWGS pressure and rWGS temperature combination. The ranges of the PtL-efficiency, for a given set of assumptions, are highlighted in 3 different grey tones. Dark grey shows the range from maximum PtL-efficiency to 0.1 % of the respective maximum efficiency. Light grey indicates the range of 1–3 %

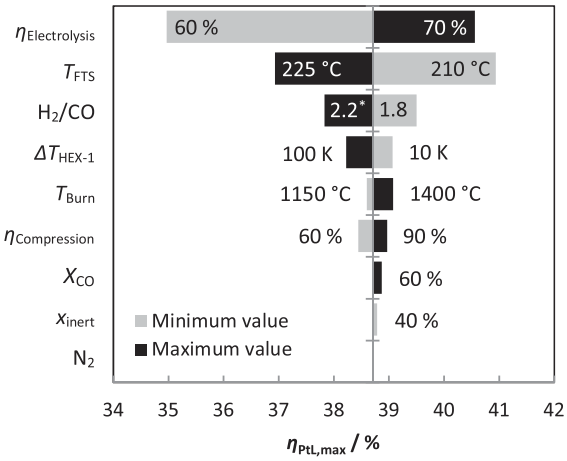

Fig. 14. Influence of the different variables from Table 1 on the maximum PtL-efficiency in terms of deviation from the base case (base case: $\eta_{PtL,max} = 38.7\%$). Black bars indicate an increase in variable value and grey bars a decrease in variable value. The optimum rWGS operating conditions (maximum PtL-efficiency) are found at $p_{rWGS} = 5$ bar and $T_{rWGS} = 825$ °C, except for the case with *$H_2/CO = 2.2$, where the optimum temperature is at $T_{rWGS} = 850$ °C.

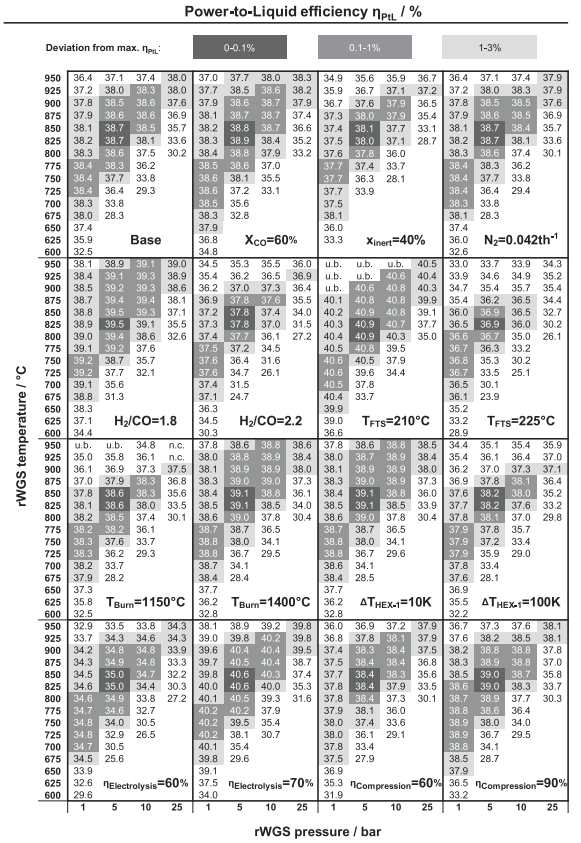

Fig. 15. Power-to-Liquid efficiency for different assumptions, rWGS pressures and rWGS temperatures. N.c. – not converged: No value available for the given constellation. U.b. – upper boundary: Rec-rWGS approaches zero and the inert gas content exceeds the fixed 50 mol%.

and medium grey of 0.1–1 %. The dark grey rWGS temperature and pressure constellations are not affected significantly by the variation of the variables. Remarkably, 5 bar and 825 °C (the optimum operating conditions for the base case) are included in the optimum operating conditions throughout the whole variation. This indicates that the optimum found for the base case is surprisingly robust. For increasing H_2/CO, T_{FTS} and decreasing T_{Burn}, $\Delta T_{HEX\text{-}1}$ the optimum window is comparably narrow whereas the inverse flattens the influence of the rWGS operating conditions leading to a broad range of rWGS operating conditions within the light grey range. The correlation of HEX-1 and HEX-2 becomes evident when comparing T_{Burn} and $\Delta T_{HEX\text{-}1}$. Similar efficiencies, for a fixed rWGS pressure and temperature, are found for $T_{Burn} = 1400$ °C and $\Delta T_{HEX\text{-}1} = 10$ K. Increasing the burner temperature from 1200 °C to 1400 °C leads to an increase in thermal energy available from HEX-2. This decreases the thermal energy demand in HEX-1. As described before, decreasing $\Delta T_{HEX\text{-}1}$ leads to decreased heat duty from HEX-2. Hence, both cases have lower fuel demand and thus higher product output, as less water is produced.

Fig. 16 shows the hydrogen efficiency for the different variable variations. Increasing T_{Burn}, X_{CO} and decreasing $\Delta T_{HEX\text{-}1}$, H_2/CO, T_{FTS} leads to higher hydrogen efficiencies. As the hydrogen efficiency is directly related to the product output, the product output increases. The maximum hydrogen efficiency found in the base case, 725 °C and 1 bar, is confirmed for all variable variations.

In general, the carbon efficiency varies only marginally between 87

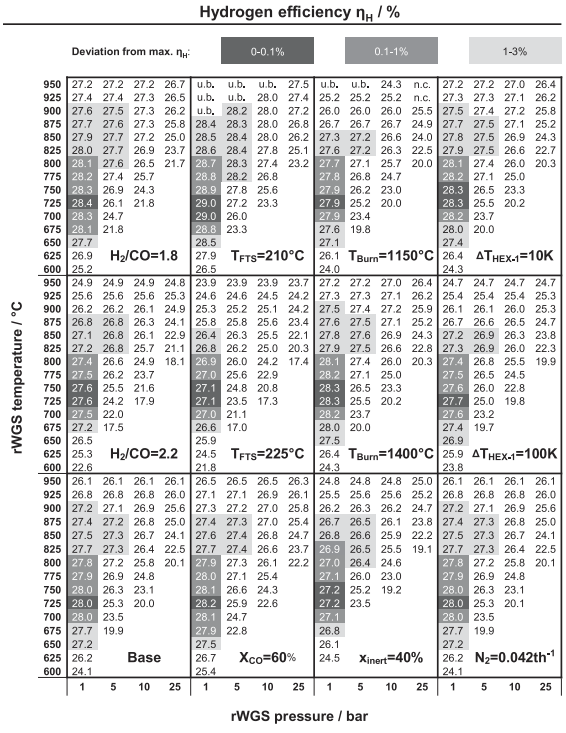

Fig. 16. Hydrogen efficiency for different assumptions, rWGS pressures and rWGS temperatures. N.c. – not converged: No value available for the given constellation. U.b. – upper boundary: Rec-rWGS approaches zero and the inert gas content exceeds the fixed 50 mol%.

and 90 %. It depends on the CO_2 recovery from the cement plant and purged gas. More purged gas decreases the carbon efficiency. The maximum carbon efficiency (90 %) is found for the variation of the impurities as the purged gas decreases with decreasing impurities. The influence of the rWGS operating conditions on the carbon efficiency is negligible (see chapter 3.3).

Comparison with literature results

To our knowledge, there is no experimental data available in the literature for the exact same configuration as described in this work. The closest resemblance of an experimental setup to the one described in this work can be found in [15]. The SOLETAIR pilot plant consists of a unit for direct air capture DAC, a PEM electrolyzer, a rWGS reactor with electrical heating and a FT micro-structured heat exchanger reactor [15]. In contrast to the configuration described in Chapter 2, there is no recycling of the gaseous FT products. The rWGS is operated at 850 °C and 4 bar and the operating conditions of the FT reactor are H_2/CO = 2.1, 230–240 °C and 20 bar [15]. No results are given for the PtL-efficiency. 30.8 % of the hydrogen and 59.5 % of carbon ends up in the FT product (including gaseous components) [15]. Applying the same operating conditions for the FTS (T_{FTS} is set to 230 °C) and rWGS in our process model gives a hydrogen efficiency of 27.3 %. The hydrogen efficiency in the pilot plant is probably slightly higher due to the fact that the heat for the rWGS is provided electrically and not by combustion of the recycling gas. The combustion of recycling gas increases water production, which decreases hydrogen efficiency. The carbon efficiency is higher in this work ($\eta_C = 88$ %) as the implementation of recycles increases the carbon efficiency, which was also observed in the analysis of a theoretical plant in [15]. In this theoretical plant a carbon efficiency of 94 % is calculated [15]. The carbon efficiency in [15] is based on the amount of CO_2 from the DAC, whereas in our definition it is based on the amount of CO_2 entering the MEA from the cement plant. Replacing the denominator in equation (xvi) by the amount of carbon recovered by the MEA unit, gives a carbon efficiency of 97%, which is slightly higher than the carbon efficiency in [15]. For the theoretical plant a PtL-efficiency of 47% (based on the higher heating value) is given in [15]. The maximum PtL-efficiency in this work is $\eta_{PtL,LHV} = 40.9$ % (T_{FTS} = 210 °C, see Fig. 15), which equals $\eta_{PtL,HHV} = 44$ % (based on the higher heating value HHV). The slightly lower PtL-efficiency is probably correlated to the slightly lower hydrogen efficiency. The hydrogen efficiency in the theoretical plant is 32 % which is close to the thermodynamic optimum of $\eta_H = 33.3$ % [15]. The highest hydrogen efficiency found in this work is 29 % (T_{FTS} = 210 °C, see Fig. 16). The slightly lower hydrogen efficiency is probably related to the difference in rWGS heat supply. In this work an allothermal rWGS reactor with oxyfuel burner is implemented, whereas the theoretical plant from [15] is equipped with an autothermal rWGS reactor. This possibly explains the difference in hydrogen efficiency, and further PtL-efficiency.

Conclusions

As neither the rWGS nor the FTS provide full conversion, recycles are necessary to increase the carbon efficiency of the PtL process. This increases the complexity of the process and thus, finding the optimum operating conditions for the rWGS unit within the FT-based Power-to-Liquid process is not straightforward. To find the optimum operating conditions in terms of energetic efficiency and H-/C-efficiency, a detailed process analysis was conducted. The findings of this process analysis can be summarized as follows:

- Increasing pressure and decreasing temperature in the rWGS reactor leads to increased methane formation. This affects the properties of the recycle and increases the recycle rates to the rWGS.
- For a given rWGS pressure there is a plateau, where the rWGS temperature has only minor influence on the efficiencies. Outside this plateau, the efficiencies decrease due to an increase in methane formation (low temperatures) and a decrease in HEX-1 efficiency (high temperatures).
- Intrinsically, the efficiencies are related to the product output. The product output correlates inversely with the water produced in the overall process. On the one hand, the water production correlates with the heating demand and the burner fuel composition, and hence, the recycle gas composition. Both are influenced mainly by the methane content in the rWGS product gas. On the other hand, the water production is influenced by the heat exchanger efficiency of HEX-1. The decrease in heat transfer at high temperatures (to avoid a temperature cross in the heat exchanger) leads to decreasing product output. The maximum product output is found at 725 °C and 1 bar.
- The H-efficiency correlates directly with the product output. Hence, the maximum efficiency ($\eta_H = 28$ %) is also found at 725 °C and 1 bar.
- The C-efficiency ($\eta_C = 88$ %) is not affected significantly by the rWGS operating conditions. It is restricted by the recovery rate of the MEA unit.
- The maximum Power-to-Liquid efficiency is obtained at 5 bar and 825 °C (η_{PtL} = 38.7 %). In comparison to the optimum operating conditions in terms of hydrogen efficiency, the energetic optimum is shifted towards higher rWGS pressure due to the decreased electricity required for compression. The optimum rWGS temperature is shifted towards higher temperature as higher temperatures are required to reach the same CO-selectivity (less methane formation).
- Pinch analysis shows a significant amount of excess high temperature heat available in the process. Using this high temperature heat to produce electricity may increase the overall PtL-efficiency. However, it has yet to be proven whether this is economically beneficial.

- Significant influence of the assumptions on the efficiencies is observed. However, the optimum rWGS operating conditions obtained in the base case are found to be in the highest PtL-efficiency ranges within the whole investigated parameter range (0.1% variation based on the respective $\eta_{PtL,max}$). This indicates robust rWGS optimum operating conditions.

Note: Although carbon formation is neglected in this work, it might narrow down the possible operating window of the rWGS, and thus, has to be further investigated in detail.

Declaration of Competing Interest

The authors declare that they have no known competing financial interests or personal relationships that could have appeared to influence the work reported in this paper.

References

[1] Paris Agreement. 2015, United Nations Framework Convention on Climate Change.
[2] Sims, R., et al., 2014: Transport, in Climate Change 2014: Mitigation of Climate Change. Contribution of Working Group III to the Fifth Assessment Report of the Intergovernmental Panel on Climate Change. 2014, Cambridge University Press: Cambridge, United Kingdom and New York, NY, USA. p. 606.
[3] Carbon offsetting for international aviation. 2019.
[4] Conference on aviation and alternative fuels. in Power-to-Liquids (PtL): Sustainable alternative fuels produced from renewable electricity. 2017. Mexico City.
[5] IATA Sustainable Aviation Fuel Roadmap. 2015(1).
[6] IATA, Resolution on the commercial deployment of sustainable alternative fuel for aviation. 2017: 73rd IATA Annual General Meeting.
[7] Steele, P., EU Renewable Energy Directive / Sustainable Aviation Fuel, in Open Letter from the IATA. 2018.
[8] Schmidt, P., et al., Power-to-Liquids as Renewable Fuel Option for Aviation: A Review. 2018. 90(1-2): p. 127-140.
[9] Becker, W., et al., Production of Fischer–Tropsch liquid fuels from high temperature solid oxide co-electrolysis units. 2012. 47(1): p. 99-115.
[10] Cinti, G., et al., Integration of Solid Oxide Electrolyzer and Fischer-Tropsch: A sustainable pathway for synthetic fuel. 2016. 162: p. 308-320.
[11] Fasihi, M., D. Bogdanov, and C. Breyer, Techno-economic assessment of power-to-liquids (PtL) fuels production and global trading based on hybrid PV-wind power plants. Energy Procedia, 2016. 99(10th International Renewable Energy Storage Conference, IRES 2016): p. 243-268.
[12] Herz, G., E. Reichelt, and M. Jahn, Techno-economic analysis of a co-electrolysis-based synthesis process for the production of hydrocarbons. 2018. 215: p. 309-320.
[13] König, D.H., et al., Simulation and evaluation of a process concept for the generation of synthetic fuel from CO2 and H2. 2015. 91: p. 833-841.
[14] Tremel, A., et al., Techno-economic analysis for the synthesis of liquid and gaseous fuels based on hydrogen production via electrolysis. 2015. 40(35): p. 11457-11464.
[15] Vázquez, F.V., et al., Power-to-X technology using renewable electricity and carbon dioxide from ambient air: SOLETAIR proof-of-concept and improved process concept. 2018. 28: p. 235-246.
[16] De Klerk, A., Fischer-tropsch refining. 2012: John Wiley & Sons.
[17] Rostrup-Nielsen, J. and L.J. Christiansen, Concepts in Syngas Manufacture, ed. W. S.P. Co.Pte.Ltd. Vol. Catalytic science series. 2011, Denmark: Imperial College Press, London.
[18] Finlayson, B.A., Introduction to chemical engineering computing. 2006: Wiley Online Library.
[19] Environmental Data of the German Cement industry. 2016: Duesseldorf.
[20] WindEnergie, B.B., Windenergie in Deutschland - Zahlen und Fakten. 2019.
[21] Estelmann, S., R.-U. Dietrich, and A. Seitz, Flexibilitätsoptionen in der Grundstoffindustrie Methodik| Potenziale| Hemmnisse. 2018.
[22] Schirrmeister, S. Power-to-X Anlagen im technischen Maßstab. in 2. Aachener Ofenbau- und Thermoprozess-Kolloquium. 2019. Aachen.
[23] Collins CD. Implementing phytoremediation of petroleum hydrocarbons. In: Phytoremediation. Springer; 2007. p. 99–108.
[24] Aftalion, F. and J.A. Kent, Handbook of industrial chemistry and biotechnology. 2012.
[25] von Schéele J. Technologies for energy and operation efficiency in stainless steel production. Linde India Limited 2015.
[26] Smolinka, T., M. Günther, and J. Garche, Stand und Entwicklungspotenzial der Wasserelektrolyse zur Herstellung von Wasserstoff aus regenerativen Energien: NOW-Studie: Kurzfassung des Abschlussberichts. 2011: Fraunhofer ISE.
[27] CO2 capture in the cement industry. 2008.
[28] Peters, M.S., et al., Plant design and economics for chemical engineers. Vol. 5. 2003: McGraw-Hill New York.
[29] S. Roussanaly et al. Techno-economic analysis of MEA CO2 capture from a cement kiln - impact of steam supply scenario 2017 Lausanne, Switzerland 14 18.
[30] Schmidt O, et al. Future cost and performance of water electrolysis: an expert elicitation study. Int J Hydrogen Energy 2017;42(52):30470–92.
[31] Bertuccioli, L., et al., Development of Water Electrolysis in the European Union. 2014, Fuel Cells and Hydrogen Joint Undertaking: Lausanne.
[32] Habermeyer, F., S. Adelung, and E. Kurkela, Flexible combined production of power, heat and transport fuels from renewable energy sources. Deliverable Report for EU Project FLEX CHX, 2018.
[33] Thema, M., F. Bauer, and M. Sterner, Power-to-Gas: Electrolysis and methanation status review. 2019. 112: p. 775-787.
[34] Wesenberg MH. Gas heated steam reformer modelling. Trondheim: Norwegian University of Science and Technology:; 2006. p. 11–2.
[35] Skogestad, S., Chemical and energy process engineering. 2008: CRC press.
[36] Sie ST, Senden MMG, Van Wechem HMH. Conversion of natural gas to transportation fuels via the shell middle distillate synthesis process. (SMDS) 1991;8 (3):371–94.
[37] Luque, R. and J. Clark, Handbook of biofuels production: Processes and technologies. 2010: Elsevier.
[38] Kaiser, P., F. Pöhlmann, and A. Jess, Intrinsic and Effective Kinetics of Cobalt-Catalyzed Fischer-Tropsch Synthesis in View of a Power-to-Liquid Process Based on Renewable Energy. 2014. 37(6): p. 964-972.
[39] Fratalocchi, L., et al., Intensifying heat transfer in Fischer-Tropsch tubular reactors through the adoption of conductive packed foams. 2018. 349: p. 829-837.
[40] Vervloet D, et al. Fischer-Tropsch reaction–diffusion in a cobalt catalyst particle: aspects of activity and selectivity for a variable chain growth probability. Catal Sci Technol 2012;2(6):1221–33.
[41] Kaiser, P., et al., Production of liquid hydrocarbons with CO2 as carbon source based on reverse water-gas shift and Fischer-Tropsch synthesis. 2013. 85(4): p. 489-499.
[42] Kaiser, P. and A. Jess, Modeling of multitubular reactors for Iron-and Cobalt-catalyzed Fischer–Tropsch syntheses for application in a power-to-liquid process. 2014. 2(5): p. 486-497.
[43] Leckel, D. and M. Liwanga-Ehumbu, Diesel-selective hydrocracking of an iron-based Fischer– Tropsch wax fraction (C15– C45) using a MoO3-modified noble metal catalyst. 2006. 20(6): p. 2330-2336.
[44] Coonradt HL, et al. Mechanism of hydrocracking. Reactions of Paraffins and Olefins. 1964;3(1):38–45.
[45] Adelung, S., D. Schnellbögl, and R.-U. Dietrich, Reaktionskinetik der reversen Wassergas-Shift Reaktion bei Normaldruck zur Übertragung auf die Synthesegasbereitstellung im PtL-Prozess.
[46] Albrecht, F.G., et al., A standardized methodology for the techno-economic evaluation of alternative fuels–A case study. 2017. 194: p. 511-526.
[47] Visconti, C.G. and M. Mascellaro, Calculating the product yields and the vapor–liquid equilibrium in the low-temperature Fischer–Tropsch synthesis. 2013. 214: p. 61-73.
[48] Yang, J., et al., Fischer–Tropsch synthesis: A review of the effect of CO conversion on methane selectivity. 2014. 470: p. 250-260.

Paper 2

Impact of the reverse water-gas shift operating conditions on the Power-to-Liquid fuel production cost

Sandra Adelung, Ralph-Uwe Dietrich

The following research paper was published in
Fuel
Volume 317, June 2022, 123440
https://doi.org/10.1016/j.fuel.2022.123440

Contribution roles

Sandra Adelung:
Research work - Methodology and model development, formal analysis and data curation, investigation and validation
Writing – Conceptualization, visualization, original draft and editing

Ralph-Uwe Dietrich:
Reviewing and supervision

Fuel 317 (2022) 123440

Contents lists available at ScienceDirect

Fuel

journal homepage: www.elsevier.com/locate/fuel

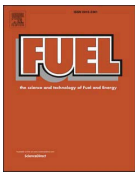

Impact of the reverse water-gas shift operating conditions on the Power-to-Liquid fuel production cost

Sandra Adelung *, Ralph-Uwe Dietrich

German Aerospace Center, Institute of Engineering Thermodynamics, Pfaffenwaldring 38-40, Stuttgart, Germany

ARTICLE INFO

Keywords:
TEA
Techno-economic
Reactor cost
Syn fuels
Synthetic fuels
Allothermal RWGS reactor
PtX
Power-to-fuels
Synthetic hydrocarbons

ABSTRACT

Fischer-Tropsch fuels from renewable sources may contribute to defossilize the transport sector, especially where high energy-dense fuels are required. The objective of this work is to analyze the impact of the RWGS operating conditions with respect to minimizing the net production cost *NPC*. Therefore, a method to estimate the RWGS reactor costs for varying RWGS operating conditions is introduced. This method allows to identify the respective tube design criterion (pressure drop, heat transfer or kinetic limitation) at a given set of operating conditions as well as to identify the optimum tube geometry with respect to low steel costs. The plant under investigation is assumed to process a constant amount of hydrogen (48.4 kt_{H2}/a) producing 52–82 kt_{C5+}/a syncrude depending on the RWGS operating conditions. The results indicate that the RWGS operating conditions affect the *NPC* rather through the general process performance than through the impact of the actual reactor costs. The main contributor to the *NPC* is the hydrogen cost. Different hydrogen cost cases are investigated to identify robust optimum RWGS operating conditions. The minimum *NPC* is observed at 1.81 €/kg_{C5+}, 3.06 €/kg_{C5+} and 5.47 €/kg_{C5+} for 2.3 €/kg_{H2}, 4.1 €/kg_{H2} and 7.6 €/kg_{H2}, respectively. Intermediate RWGS pressure (5 bar) and temperature (800 °C) allow for low production costs throughout all hydrogen cost cases.

1. Introduction

Sustainable aviation fuels (SAF) may help defossilizing the transport sector, particularly where high energy-dense fuels are required. Especially in the aviation sector, liquid alternative jet fuel will be important to reduce the net CO_2 emissions in the near future [1]. In 2019, < 200,000 tons of SAF were produced globally [1]. This accounts for < 0.1 % of the jet fuel for commercial airlines [1]. One of the four recommended alternative jet fuel production routes is to synthesize hydrocarbons from renewable electricity, water and carbon dioxide via Fischer-Tropsch synthesis (FTS) in a Power-to-Liquid process [1]. This route may exhibit the lowest maturity, but it offers the great benefit of abundant feedstock availability in comparison to biomass based processes (assuming direct air capture DAC) [1].

Most of the required technologies to convert water and CO_2 to FT fuels are readily available at industrial scale (except the reverse water–gas shift (RWGS) reactor for CO_2 activation) [2,3]. Mature technologies for hydrogen production from water splitting are proton exchange membrane (PEM) electrolysis (commercially available at medium scale, efforts ongoing to bring the technology to the 100 MW scale [3]) and alkaline electrolysis (commercially available at large scale, typical scale of chlor-alkali electrolysis: 30–150 MW_{el} [4]). CO_2 absorption by amine scrubbing is state-of-the-art for food and beverages to capture CO_2 from point sources (typical scale: 16.7 t_{CO2}/h) [5]. Fischer-Tropsch synthesis from syngas, including hydrocarbon upgrading, is a mature technology available at large scale (Bintulu, Malaysia, Shell, 14,700 barrel per day, ~ 2.33 million liter per day) [6]. Apart from that, alternative technologies are subject to research and development or available at smaller scales, like solid oxides electrolyzer cells SOEC, co-electrolysis, CO_2 capture from air and intensified reactor concepts like microreactors for FTS.

The FT based PtL process chain has been experimentally investigated at pilot scale. The pilot plant SOLETAIR in Finland comprises DAC, PEM, RWGS (electrically heated) and a FT micro-structured reactor [7]. The product capacity is 6.2 kg per day of FT wax and oil [7]. Sunfire's pilot plant in Germany is in operation since 2015 for endurance testing [8]. It has been built to produce one barrel per day (=159 L per day) of FT syncrude [8]. The plant consists of SOEC (provides partial amount of hydrogen demand), RWGS (electrically heated) and a cobalt catalyzed FTS [8]. In the project Kopernikus PtX, a small test facility (DAC, co-electrolysis, FT micro-structured reactor and hydrocracking) has been set up (10 L per day), and will be expanded to a plant capacity of 200 L per day, first, and then into the pre-industrial scale of a demonstration

* Corresponding author.

https://doi.org/10.1016/j.fuel.2022.123440
Received 26 November 2021; Accepted 22 January 2022
Available online 12 February 2022

Nomenclature

Abbreviations

AEL	alkaline electrolysis
API	American Petroleum Institute
C-j	compressor *j*
Cj	hydrocarbon with *j* carbon atoms
Cj+	fraction of hydrocarbons with at least *j* carbon atoms
COMP	compressors
DAC	direct air capture
Δp	pressure drop limitation
FT(S)	Fischer-Tropsch (synthesis)
h	heat transfer limitation
HC	hydrocracker
HEX-j	heat exchanger *j*
i.n.	impact neglected
k	kinetic limitation
LPG	liquefied petroleum gas
MEA	monoethanolamine
MPS	medium pressure steam
n.i.	no impact
NBC	Nordic Blue Crude
PEM	proton exchange membrane
PO	plant overhead cost
POX	partial oxidation
PtL	Power-to-Liquid
(R)WGS	(reverse) water-gas shift
SAF	sustainable aviation fuels
S-j	split *j*
SMR	steam methane reforming
SOEC	solid oxides electrolyzer cell
TRL	technology readiness level
V-j	valve *j*
WHB	waste heat boiler

Variables and constants (greek characters)

δ_{CA}	corrosion allowance
Δp	pressure drop
δ_σ	stress thickness
ε	void fraction
η	efficiency factor
η_H	hydrogen efficiency
η_{PtL}	power-to-liquid efficiency
μ	dynamic viscosity
ν	kinematic viscosity
ρ_{bed}	catalyst bed density
ρ_{steel}	steel density (RWGS reactor tube)
σ_r	rupture allowable stress

Variables and constants (time dependent)

$\dot{m}_{C5+}$	mass flow C5+ product
$\dot{n}_{H,C5+}$	molar flow rate of hydrogen in C5+ product fraction
$\dot{n}_{H,in}$	molar flow rate of hydrogen from electrolysis
$\dot{Q}_{RWGS}$	heat demand RWGS
$\dot{V}$	volumetric flow rate

Variables and constants (latin characters)

ACC	annualized capital cost
CAPEX	capital expenditures
C_{cat}	mean specific catalyst cost for plant lifetime
$C_{Catalyst}$	cost for RWGS catalyst
CEPCI	chemical engineering plant cost index
$C_{Furnace}$	cost for RWGS furnace
C_{labor}	labor cost
C_{steel}	mean specific steel cost for plant lifetime (RWGS reactor tube)
C_{Tubes}	cost for RWGS reactor tubes
d_i	degression factor of equipment *i*
D_i	inner tube diameter (RWGS reactor tube)
$D_{i,opt}$	optimum inner tube diameter (RWGS reactor tube)
D_p	catalyst pellet diameter
EC_i	equipment cost of equipment *i*
$EC_{Ref,i}$	equipment cost of reference equipment *i*
EC_{RWGS}	equipment cost of RWGS
FCI	fixed capital invest
f_{corr}	corrosion fraction
$F_{eco,i,j}$	economic factor *j* ($j = 1…12$) for equipment *i*
IR	interest rate
L	tube length (RWGS reactor tube)
LHV_{C5+}	lower heating value of C5+ product fraction
L_{opt}	optimum tube length (RWGS reactor tube)
NPC	net production cost
$n_{tube,h}$	number of tubes in case of heat transfer limitation
$n_{tube,opt}$	optimum number of tubes (RWGS reactor tube)
$n_{tube,\Delta p}$	number of tubes in case of pressure drop limitation
OPEX	operational expenditures
$OPEX_{dir}$	direct operational expanditures
$OPEX_{indir}$	indirect operational expanditures
$P_{compression}$	electricity for compression
$P_{electrolysis}$	electricity for electrolysis
p_j	partial pressure of component *j*
P_{MEA}	electricity for MEA
p_{RWGS}	pressure RWGS
q_{av}	average heat flux density
R^2	corefficient of determination
s	wall thickness (RWGS reactor tube)
S_i	physical capacity for equipment *i*
$S_{Ref,i}$	physical capacity of reference for equipment *i*
T_{RWGS}	temperature RWGS
V_{heat}	steel volume in case of heat transfer limitation (RWGS reactor tube)
$V_{kinetic}$	steel volume in case of kinetic limitation (RWGS reactor tube)
$V_{optimum}$	optimum steel volume (RWGS reactor tube)
$V_{pressure}$	steel volume in case of pressure drop limitation (RWGS reactor tube)
w_0	velocity at tube inlet
y	Operating time of plant

plant (1500–2000 L per day) [9].

Larger scales are in planning/construction phase. Nordic Blue Crude NBC AS at Herøya, Porsgrunn, Norway plans to commission the demonstration plant E-fuel 1 in 2023 (8,000 t syncrude/a (20 MW_{el})) [2]. The patented RWGS reactor concept consists of a POX (partial oxidation) section, alumina bed and quenching section [2]. The electricity for the hydrogen production is to be provided from onshore and offshore wind farms [2]. According to [10], partners involved in the E-fuel 1 planning phase were Sunfire (expertise in SOEC and co-electrolysis) and Climeworks (expertise in DAC). However, according to NBC, in order to keep the costs low, most of the CO_2 is to be bought from a fertilizer plant (30 €/t_{CO2} vs. 600 €/t_{CO2}) and hydrogen will be produced via alkaline electrolysis [11]. *CAPEX* for the demo plant are given by Aker Solutions with 120 million € [2]. Moving to the next scale,

their schedule foresees to increase the capacity to a 200 million liter per annum plant (E-fuel 2), to be commissioned in 2027 also at Herøya [2].

Some theoretical works have been published on the assessment of the described PtL process chain (see [3,12] for literature reviews). Techno-economic evaluations for different syngas/hydrogen production pathways are available in the literature: co-electrolysis [13–15], SOEC [16], PEM [17–20] and AEL [15,21]. See also [22] for other options in the field of CO_2 activation (e.g. photocatalytic pathways). The syngas in this work is provided from hydrogen and carbon dioxide in an allothermal RWGS reactor with oxyfuel burner. Similar setups have been investigated by [17,18,20]. König *et al.* investigate the impact of full load hours, electricity costs and electrolyzer costs on the *NPC* [20]. Based on this they calculate a broad range of *NPC*s (5.48–21.35 USD per gasoline gallon equivalent, 2.01–7.83 USD/kg) [20]. They use the RWGS reactor cost from [23], who base their RWGS reactor cost on WGS reactor cost from source [24]. It is worth mentioning that the operating conditions of a WGS (exothermic) reactor differ broadly from the operating conditions of a RWGS (endothermic) reactor. Tremel *et al.* assume hydrogen cost of 3 €/kg_{H2} and from that approximate the *NPC* to 2.34 €/kg_{diesel} and 2.01 €/$kg_{syncrude}$ [17]. Their economic assessment is not based on process modelling and equipment-based calculations. Hence, it is not possible to outline the differences of the process designs. Schemme *et al.* calculate a *NPC* of 2.3 € per liter diesel equivalent (= 2.75 €/kg) for hydrogen cost of 4.6 €/kg_{H2} [18]. The underlying RWGS reactor cost assumption is not recorded in their work. For a cost comparison of these publications with this work see Chapter 3.3.

Previous work focused on finding the optimum RWGS operating conditions with respect to maximizing the carbon, hydrogen and Power-to-Liquid efficiency [25]. The investigated process consisted of a PEM electrolysis, an allothermal RWGS reactor with heat supply from an oxyfuel burner, that burns a partial amount of the recycling gas, a fixed-bed FT reactor and a hydrocracker [25]. Gaseous products are recycled to maximize the carbon efficiency [25]. The RWGS operating conditions influence the recycling gas composition and split ratios as well as the heat demand of the RWGS reactor [25]. The maximum Power-to-Liquid efficiency was observed at 825 °C and 5 bar and the maximum hydrogen efficiency at 725 °C and 1 bar [25]. In order to complement the previously conducted technical analysis with an economic analysis (economic and energetic optimum operating conditions may differ), this work focuses on:

- analyzing the impact of the RWGS operating conditions on the net production costs,
- finding the RWGS operating conditions exhibiting the lowest net production cost and
- evaluating the robustness of the economically optimal RWGS operating conditions.

To reach these objectives, the RWGS reactor costs have to be estimated. As the RWGS setup still has a low TRL and no data was available in the literature to account for the effect of different RWGS pressures and temperatures on the RWGS reactor cost, a methodology needed to be developed. This method, for assessing the RWGS reactor cost, accounts for:

- factors directly impacting the reactor setup (for example different wall thicknesses of the reactor tubes at different RWGS pressures and temperatures) and
- factors indirectly impacting the reactor setup through changes in process streams (for example heat demand of the RWGS reactor, different feed compositions and mass/volumetric flow rates at different RWGS operating conditions).

2. Methodology

The following chapter outlines the methodology used for process modelling, estimation of the net production cost and uncertainty analysis as well as the method used to calculate the RWGS reactor cost for varying RWGS pressures and temperatures.

2.1. Process description

The underlying process simulation is thoroughly described in [25], where the process is analyzed in terms of energetic efficiency as well as carbon and hydrogen efficiency. In comparison to the model in [25], the boundary conditions are shifted such that hydrogen is entering the system boundaries, instead of electricity and water for water electrolysis. Hence, hydrogen production is decoupled from the process and the hydrogen cost is considered as raw material (produced in Germany or imported, e.g. from Norway or Saudi Arabia, see Chapter 2.2). Fig. 1 shows the basic flowsheet for the process simulation. The plant is assumed to process a constant amount of 6.05 t/h_{H2}, which equals an electrolysis capacity of 300 MW_{el} with an efficiency of 66.7 %, based on the lower heating value [25]. Carbon dioxide is captured from a cement plant by amine washing. Carbon dioxide is then activated in the RWGS reactor to form carbon monoxide. The RWGS product gas is assumed to be at equilibrium – no full conversion can be achieved. The hot syngas is cooled in a waste-heat boiler to prevent metal dusting. The cooled syngas is subsequently converted in the FT reactor forming a broad range of hydrocarbon chain lengths. Long chained hydrocarbons are cracked in a hydrocracker and gaseous components are recycled to increase the overall carbon efficiency. One part of the recycling gas is recycled back to the FT reactor (to provide a constant inert gas content in the feed of the FT reactor), another part continues to the combustion chamber (to provide the heat for the high temperature RWGS reaction in an oxyfuel burner) and the remaining recycling gas is again converted in the RWGS reactor. Varying RWGS operating conditions affect the split ratios (S-1 and S-2). The RWGS pressure is varied between 1 bar (maximum yield of CO due to equilibrium considerations) and 25 bar (to operate the RWGS reactor on the same pressure level as the FT reactor and thereby potentially decreasing the electricity demand for compression). The maximum RWGS temperature investigated is fixed to 900 °C due to material considerations [26] and the minimum RWGS temperature corresponds to the temperature where the inert gas content in the feed of the FT reactor would exceed the predefined specification of 50 mol-% [25].

2.2. Economic analysis

The methodology used for the economic analysis is based on [27] and further described in [19]. General plant assumptions are shown in Table 1.

The specific net production cost NPC_{C5+} for the syncrude product fraction $\dot{m}_{C5+}$ is calculated according to:

$$NPC = \frac{ACC + \sum OPEX_{dir} + \sum OPEX_{indir} + C_{labor}}{\dot{m}_{C5+}} \quad (1)$$

The annuity cost *ACC* is calculated using equation (4) from the fixed capital investment *FCI*, the interest rate *IR* and the plant operating time *y*. The *FCI* derives from equation (3) through the equipment costs EC_i and the economic factors $F_{eco,i,j}$. For the respective economic factors $F_{eco,i,j}$ see Table 5 - Base Case. Equipment costs EC_i for non-standard equipment are calculated from equation (2) with the input data from Table 2. Costs for standard equipment like heat exchangers, pumps, compressors and columns are estimated based on data from [27].

$$EC_i = EC_{Ref,i} \times \left(\frac{S_i}{S_{Ref,i}}\right)^{d_i} \times \left(\frac{CEPCI}{CEPCI_{Ref}}\right) \quad (2)$$

$$FCI = \sum_{i=1}^{m} EC_i \times \left(1 + \sum_{j=1}^{10} F_{eco,i,j}\right) \times \left(1 + \sum_{j=11}^{12} F_{eco,i,j}\right) \quad (3)$$

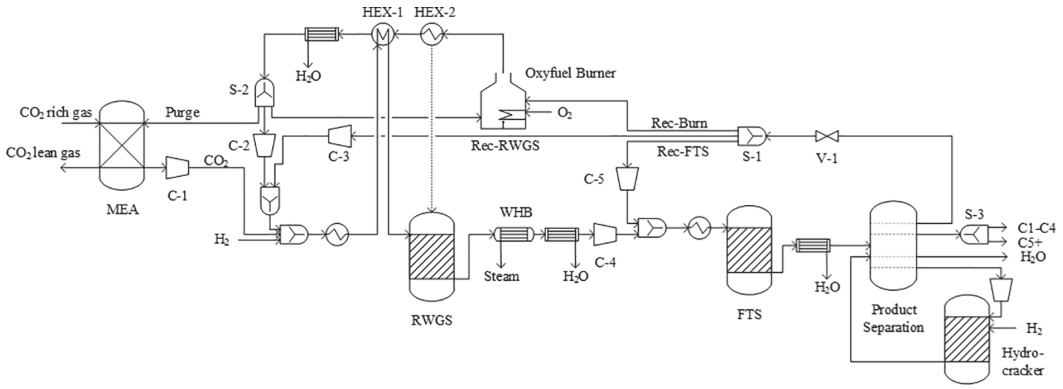

Fig. 1. Flowsheet of the PtL model in Aspen Plus® including monoethanolamine absorption (MEA), waste heat boiler (WHB), compressors (C), splits (S), heat exchangers (HEX) and valves (V).

Table 1
General assumptions for the Power-to-Liquid plant.

General Plant Assumptions	
Plant capacity	6.05 t/h H_2 input
Full load hours	8,000 h/a
Operating time of plant *y*	20 years
Interest rate *IR*	7 %
Base year	2019
Location	Germany
Site	Brownfield

Table 2
Cost data for calculating equipment cost according to equation (ii) for non-standard equipment.

	EC_{Ref}	S_{Ref}	Unit	*d*	Ref.
MEA	31.8 M$	134.81	$t_{CO2,captured}$/h	0.8	[5]
FT	3.65 M$	3.345	kg_{C5+}/s	0.67	[28]
HC[a]	43.56 M$	35.88	kg/s	0.55	[29]
RWGS	See chapter 2.4				

[a] Turnkey: All economic factors already included.

$$ACC = FCI\left(IR \times \frac{(1+IR)^y}{(1+IR)^y - 1} + \frac{IR \times y}{9}\right) \quad (4)$$

Direct *OPEX* are calculated based on data given in Table 3 by multiplying the specific cost with the stream quantity. Raw materials, utilities and waste water add to the expenditures whereas the remaining by-products may be sold to reduce the *NPC*. Therefore, the remaining FT products C1-C4, mainly propane and butane as the smaller molecules are recycled, are assumed to be sold. Indirect *OPEX* are calculated with the factors depicted in Table 4 (see [19,27] for details). Labor cost C_{labor} is estimated according to [27].

As the hydrogen cost is the main contributor to the *NPC* (see chapter 3.3) and the hydrogen cost is, among other factors, highly dependent on the electricity price, two additional scenarios are investigated to determine the impact of the hydrogen cost on the optimum RWGS operating conditions: 2.3 €/kg_{H2} (2030, balancing grid services) and 7.6 €/kg_{H2} (2012, renewable generation only, subsidies included, off-grid scenario) [30]. More details on these three scenarios can be found in [30]. Apart from that work, hydrogen supply costs have been estimated and investigated by several researchers, also with the focus on imported hydrogen. For example, Brändle *et al.* calculate the costs to produce and supply hydrogen in Germany (wind onshore: 2.7–3.1 USD/$kg_{H2,2030}$) and compare the results to the costs for imported hydrogen from Norway (wind onshore, pipeline transport: 2.2–3.2 USD/$kg_{H2,2030}$) as well as

Table 3
Specific cost for raw materials, utilities and by-products to calculate direct *OPEX* for the base year 2019.

	Price	Unit	Ref.
Raw Materials and Utilities			
Electricity[a]	84.55	€/MWh	[35]
Hydrogen[b]	4.1	€/kg	[30]
Cooling Water[c]	0.005	€/m^3	[36]
Oxygen[d]	23.77	€/t	[37]
MEA[e]	2.313	€/$t_{CO2,\ captured}$	[5]
By-Products			
District Heating[f]	0.03	€/kWh	[38]
Medium Pressure Steam[g]	19.241	€/t	[39]
C1-C4 Product[h]	1.252	€/kg	[40]
Waste water	2.5	€/m^3	[19]

[a] Electricity price for industrial consumers in Germany in 2019, recoverable levies and taxes excluded, scale: intermediate value chosen between > 150,000 MWh consumption and 70,000–150,000 MWh consumption.
[b] From [30] for the base year 2012: PEM electrolysis with an electricity price of 51 €/MWh, *CAPEX* of 1856 €/kW, 100 % load factor and an efficiency of 50 kWh/kg_{H2} = 66.67 % (LHV). In comparison for 2019 the electricity price for industrial consumers in Germany (>150,000 MWh consumption) is given by [35] between 76.8 €/MWh (excluding recoverable levies and taxes) and 34.8 €/MWh (excluding all levies and taxes).
[c] Cooling water from Elbe river.
[d] Cryogenic oxygen generation.
[e] CO_2 captured from cement plant.
[f] Brownfield: 6 bar, heating from 45 °C to 95 °C.
[g] Brownfield: 20 bar, heating from 210 °C to 215 °C, own calculations based on gas price from [39].
[h] C1-C4 product stream consists mainly of C3 and C4, hence LPG (0.626 €/L from [40]) revenue is assumed. The density is assumed to be 0.5 kg/L.

Table 4
Factors for estimating indirect *OPEX* [19,27].

	Factor	Basis
Operating supervision	0.15	Operating labor
Maintenance labor	0.01	*FCI*
Maintenance material	0.01	*FCI*
Operating supplies	0.15	Maintenance
Laboratory charges	0.2	Operating labor
Insurances and taxes	0.02	*FCI*
Plant overhead costs *PO*	0.6	Total labor costs
Administrative costs	0.25	*PO*

Table 5
Minimum and maximum values used for uncertainty analysis and economic factors $F_{eco,i,j}$ required for estimating the *FCI* (j = 1–12).

Variable	Min	Max	Base
Equipment Cost [42]			
MEA	−30 %	+50 %	
HEX	−15 %	+30 %	
Pumps & Compressors	−15 %	+30 %	
Hydrocracker	−30 %	+50 %	
FT	−30 %	+50 %	
RWGS	−30 %	+50 %	
Columns	−15 %	+30 %	
Economic Factors [27,19]			
1 Installation factor	0.25	0.55	0.47
2 Instrumentation and control	0.08	0.5	0.36
3 Piping system	0.1	0.8	0.68
4 Electrical systems	0.1	0.4	0.11
5 Buildings	0.1	0.7	0.18
6 Yard improvements	0.1	0.2	0.1
7 Service facilities	0.3	0.8	0.7
8 Engineering and supervision	0.32	0.33	0.33
9 Construction expenses	0.34	0.41	0.41
10 Legal expenses			0.04
11 Contractor's fee	0.015	0.06	0.05
12 Contingency	0.05	0.15	0.1

Saudi Arabia (photovoltaic, transport via ship: 3.9–4.6 USD/$kg_{H2,2030}$) [31]. Schorn *et al.* state hydrogen cost for the supply from Saudi Arabia to Germany of 3.4 €/$kg_{H2,2030}$ [32]. A recent study provided by Uniper and Kearney gives hydrogen cost of 4.1 €/$kg_{H2,2025}$, so the same hydrogen cost as applied in the base case in this work, for the hydrogen supply from Saudia Arabia as ammonia [33]. Timmerberg *et al.* estimate that hydrogen may be supplied to central Europe from North Africa via pipeline for 1.8–4 €/$kg_{H2,2020}$ [34]. Although these are only a few results from the various hydrogen cost supply estimates available in the literature, it seems that the investigated hydrogen cost range (2.3 €/kg_{H2} – 7.6 €/kg_{H2}) is reasonable.

2.3. Uncertainty analysis

In order to compare the different net production costs at different RWGS pressures and temperatures, an uncertainty analysis (UA) is conducted. Within this UA the uncertainties for the estimated equipment costs are taken into consideration as well as the uncertainty of the economic factors for calculating the fixed capital investment. The range of uncertainties applied is depicted in Table 5. A triangular distribution (maximum probability at base case level) is assumed for the probability functions. The UA is conducted via Monte-Carlo simulation and by applying the Sobol sequence as the sampling method. Direction numbers and primitive polynomials for the Sobol sequence are retrieved from [41]. The number of samples is 10,000. The results from the UA are incorporated as the 95 % confidence intervals shown in Fig. 10.

2.4. Cost estimation RWGS reactor

In order to identify the optimum RWGS operating conditions, the RWGS reactor cost needs to be sensitive to changes in RWGS pressure and temperature. Additionally, the RWGS feed properties change for different RWGS pressures and temperatures as the recycling ratios differ [25]. Therefore, a more detailed approach is necessary in comparison to the equipment cost estimation techniques applied in Chapter 2.2.

The reactor is designed as a tubular fired reformer – similar to allothermal steam methane reforming (SMR) (compare Fig. 2). The feed stream enters the tubes at 450 °C. The reaction takes place at the nickel catalyst pellets and the heat is provided by a furnace in the combustion chamber. SMR is a highly mature technology, whereas no RWGS reactor has been built at industrial scale, yet [43]. Hence, appropriate data for SMR is widely available and quite reliable. Table 6 shows some

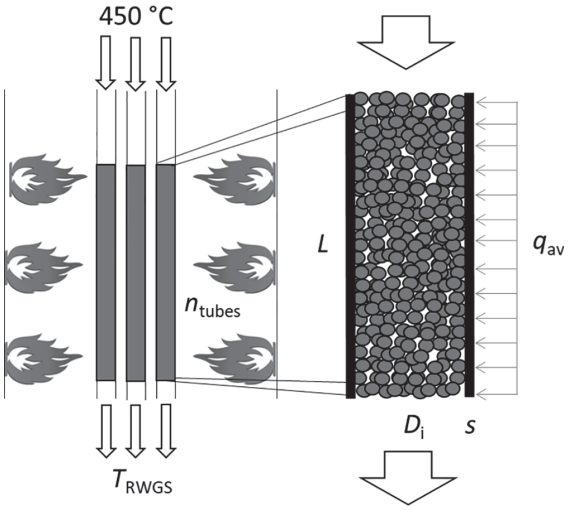

Fig. 2. Basic scheme of the allothermal RWGS reactor. The feed stream enters at 450 °C and the reactants are converted on nickel pellets. The heat is provided by a furnace. The number of tubes n_{tubes} and the optimum tube geometry (lenght L and inner diameter D_i) are calculated using the methodology depicted in Fig. 4.

Table 6
Comparison of steam methane reforming SMR and reverse water–gas shift RWGS. RWGS reactor is assumed to be integrated in the investigated process concept.

	SMR	RWGS
Reactor setup	Fired tubular reformer	Fired tubular reformer[a]
TRL	9	6 [44]
Educt to be converted	Methane	Carbon dioxide
Reaction partner	Steam	Hydrogen
Target product	Hydrogen	Carbon monoxide
Side reactions	Water-gas shift	Reforming/forming of methane[f], reforming of light hydrocarbons[f]
Heat of reaction	Endothermic ((14): 165 kJ/mol, (12): 206 kJ/mol))	Endothermic ((13): 41 kJ/mol[e])
Technical challenges	Carbon formation and metal dusting [45]	Carbon formation and metal dusting
Operating conditions	20–30 bar, 700–900 °C [45]	1–25 bar, up to 900 °C[d]
Tube design criterion	Heat transfer limitation in gas phase	Heat transfer vs. pressure drop vs. kinetics[d]
Kinetics	Ni-catalyst [45], high temperature process: diffusion limited reaction [45]	Ni-catalyst [46], high temperature process: diffusion limited reaction [46]
Inner diameter	0.1–0.2 m [45]	0.1–0.2 m[b]
Tube length	10–13 m [45]	4–10 m[b]
Number of tubes	40–400 [45]	150–560[c]
Average heat flux	100–150 kW/m^2 [45]	100 kW/m^2[a]

[a] Assumed in this work
[b] Optimized in this work
[c] Result from this work
[d] Investigated in this work
[e] Overall endothermicity increases with increased amount of short chained hydrocarbons in the RWGS feed, which is affected by the RWGS operating conditions and their impact on the recycling gas.
[f] Reforming/ forming of methane and reforming of light hydrocarbons based on RWGS feed composition and operating conditions (see [e]).

similarities and deviations when comparing SMR and RWGS with respect to the different processes, reactors and reactions. Due to the similarities of SMR and the allothermal RWGS reactor in this study, typical values for SMR are assumed, if the data for RWGS are not available.

In this work, the RWGS reactor cost EC_{RWGS} are defined as the sum of furnace cost, cost for the tubes and cost for the catalyst:

$$EC_{RWGS} = C_{Furnace} + C_{Tubes} + C_{Catalyst} \quad (5)$$

The furnace cost $C_{Furnace}$ is scaled with the amount of energy that needs to be transferred in order to increase the temperature from 450 °C to T_{RWGS} plus the amount of energy required for the endothermic reaction. The according heat demand $\dot{Q}_{RWGS}$ is extracted from the process simulation. The furnace cost is calculated as follows [47]:

$$C_{Furnace} = CEPCI \times 10^{\left(A + B \log \dot{Q}_{RWGS} + C (\log (\dot{Q}_{RWGS}))\right)^2} \quad (6)$$

With $\dot{Q}_{RWGS}$ in kW, $C_{Furnace}$ in USD, A = 3.068, B = 0.6597, C = 0.0194 and $CEPCI$ = 1.535 (2002 to 2019).

The tube cost C_{Tubes} is calculated from the amount of high temperature steel required. The catalyst cost $C_{Catalyst}$ is calculated from the volume inside the tubes. Hence, the number of tubes and the geometry of each tube needs to be accessed. The tube geometry and the number of tubes may be designed to overcome:

- kinetic limitations,
- heat transfer limitations or
- limitations due to pressure drop.

Kinetics, heat duty and pressure drop are affected by the RWGS operating conditions, directly, as well as through back coupling effects from the recycling streams. Assuming a stand-alone RWGS reactor (constant feed conditions, product at equilibrium) allows to theoretically investigate the direct influences in a more straightforward way. Table 7 shows the qualitative impact of increasing temperature, pressure and inner diameter on pressure drop, kinetics, heat transfer, wall thickness, CO yield and heat duty. It is assumed that only temperature, pressure and inner diameter are varied, while all other variables are kept constant. The classification spans from highly positive (+++, meaning: low pressure drop, fast kinetics, good heat transfer, small wall thickness, high CO yield and low heat duty, respectively) to highly negative (—, meaning: vice versa). Higher temperatures lead to faster reaction kinetics (Arrhenius), increased CO yields, larger heat duty as well as higher pressure drop through higher velocities. Higher pressure decreases the pressure drop through decreased volumetric flowrate and shifts the equilibrium towards CH_4 (lower CO yield), which also decreases the heat duty (less endothermic). Increasing the inner tube diameter decreases the pressure drop, allows for improved heat transfer but also increases the wall thickness. Most of these influences exhibit a strong non-linear behavior (e.g. Arrhenius), making it difficult to provide general design regions without a numerical investigation.

Table 7
Influence of increasing temperature T, pressure p and inner tube diameter D_i in a stand-alone RWGS reactor setup on pressure drop, kinetics, heat transfer, wall thickness, equilibrium yield and heat duty. Ranking spans from highly positive (+++, meaning: low pressure drop, fast kinetics, good heat transfer, small wall thickness, high CO yield and low heat duty, respectively) to highly negative (− − −). Abbreviations: n. i. – no impact, i. n. – impact neglected, equil.-equilibrium.

	T	p	D_i
Pressure drop	–	++	+++
Kinetics	++/+++	-/+	++
Heat transfer	i. n.	i. n.	++
Wall thickness	-/–	-/–	-/–
CO yield (equil.)	+/+++	-/—	n. i.
Heat duty	-/–	+/++	n. i.

In order to calculate the required steel volume, the wall thickness of the tubes is calculated. The wall thickness depends on pressure and temperature as well as the inner tube diameter. The wall thickness s is calculated according to API 530 [26]. The tubes are designed for a lifetime of 100,000 h and the high temperature steel chosen is HK-40 [26]. The corrosion allowance δ_{CA} is assumed to be 5 mm. The design temperature is assumed to be 50 K higher than the respective reactor outlet temperature T_{RWGS}. For a given design temperature, the rupture allowable stress σ_r and the rupture exponents are retrieved from Table E.22 in API 530 [26]. In order to retrieve continuous values for the allowable stress σ_r, a fitting is conducted in the range of T_{RWGS} = 600–900 °C (coefficient of determination R^2 = 99.9). The resulting function is:

$$\sigma_r = 6.04281 \times 10^9 \times e^{-0.00774044 \times T_{RWGS}} \quad (7)$$

Further the stress thickness δ_σ is calculated from the rupture allowable stress σ_r, rupture pressure (assumed to be the operating pressure p_{RWGS}), and the inner diameter (assumed to be in the range of: D_i = 0.1–0.2 m) [26]:

$$\delta_\sigma = \frac{p_{RWGS}\, D_i}{2\sigma_r - p_{RWGS}} \quad (8)$$

The corrosion fraction is retrieved fromFigure 1 in API 530 by usage of the corrosion allowance δ_{CA} (predefined assumption, here: δ_{CA} = 5 mm), the stress thickness δ_σ and the rupture exponent [26]. The corrosion fraction is assumed to be unity if no rupture exponent is given in Table E.22 in API 530 [26]. In the transition between corrosion fractions smaller than unity to unity, non-monotone behavior occurred. For example, at 10 bar the wall thickness was observed to be: 7.3 mm, 6.2 mm, 6.9 mm at 800 °C, 750 °C, 700 °C, respectively. The corresponding corrosion fractions are 0.62, 0.68, 1, respectively. Due to this inconsistency a conservative approach is chosen by setting the corrosion fraction to unity. The resulting wall thickness s is calculated from the stress thickness δ_σ, corrosion allowance δ_{CA} and the corrosion fraction f_{corr} (here: f_{corr} = 1):

$$s = \delta_\sigma + f_{corr}\, \delta_{CA} \quad (9)$$

Similar calculations are conducted for elastic stress instead of rupture stress. The wall thicknesses obtained from the rupture stress evaluations exceed the wall thicknesses derived from the elastic stress calculations in all investigated cases ($T_{RWGS} \geq$ 600 °C). Hence, the rupture stress derived wall thickness defines the minimum required wall thickness. Table 1 in API 530 additionally states the minimum required wall thickness for austenitic steel tubes at a respective outside diameter [26]. This minimum allowable wall thickness is exceeded in all cases calculated (the minimum wall thickness calculated is 5.09 mm and the maximum of the minimum allowable thickness is 3.7 mm, at 273.1 mm outside tube diameter). The resulting wall thicknesses for different inner tube diameters at different pressures and temperatures are shown in Fig. 3. The wall thickness increases with temperature T_{RWGS}, pressure p_{RWGS} and inner tube diameter D_i.

The approach to identify the optimum geometry (D_i, L) in terms of low steel cost, and hence low steel volume, is shown in Fig. 4. In the first step the design criterion has to be identified. Therefore, reaction kinetics, heat transfer and pressure drop are investigated independently in order to find the number of tubes required to satisfy heat transfer, kinetics and pressure drop specifications ($n_{tube,\ heat}$, $n_{tube,\ kinetic}$ and $n_{tube,\ pressure}$). The bottleneck is observed where the maximum number of tubes is required to fulfill the design specifications (n_{tube} (D_i, L) = Max ($n_{tube,\ kinetic}$ (D_i, L), $n_{tube,\ heat}$ (D_i, L), $n_{tube,\ pressure}$ (D_i, L))). This gives the restricting design criterion for a given tube length L and inner diameter D_i. In order to find the optimum tube length and diameter combination, length (4–8 m) and inner diameter (0.1–0.2 m) are varied and the

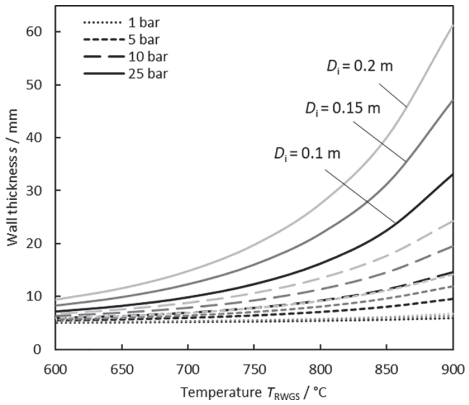

Fig. 3. Wall thickness s calculated based on API 530 [26] as a function of T_{RWGS} and p_{RWGS} for different inner diameter D_i.

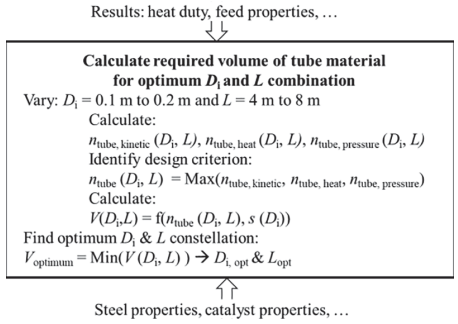

Fig. 4. Scheme for calculating the optimized tube design (optimum inner diameter D_i and length L) in terms of minimum steel volume V.

respective steel volumes $V(D_i, L)$ are calculated from the number of tubes n_{tube} (D_i, L) and the respective wall thickness s (D_i). The optimum combination (L_{opt}, $D_{i,opt}$) is established where the minimum steel volume $V_{optimum}$ is obtained. These values are then used to calculate the costs for the tubes and the catalyst (see Table 8 for additional data):

$$C_{Tubes} = n_{tube,opt}\frac{\pi}{4}\left(\left(D_{i,opt} + 2s\right)^2 - D_{i,opt}^2\right) \times L_{opt}\,\rho_{steel}\,C_{steel} \quad (10)$$

$$C_{Catalyst} = n_{tube,opt}\,\frac{\pi}{4}\,D_{i,opt}^2\,L_{opt}\,\rho_{bed}\,C_{cat} \quad (11)$$

Table 8
Input data for the estimation of tube and catalyst cost.

Parameter	Value	Unit	Ref.
ρ_{steel}	8236	kg/m^3	
C_{steel} [a]	68.5	USD/kg	[47]
ρ_{bed} [b]	667	kg/m^3	[45,48]
ε	0.55	–	[45]
C_{cat} [c]	35.7	USD/kg	[47]

[a] Mean steel cost for whole plant lifetime assuming a tube exchange after 100,000 h on stream. Steel cost of 60 USD/kg from [47] were updated to 2019 with Rogers International Commodity Index for Metals [9].
[b] Bed density is calculated from: solid density = 2355 kg/m^3 [48], pore volume = 0.25 dm^3/kg [48] and void fraction ε [45].
[c] Mean catalyst cost for plant lifetime assuming catalyst exchange every 4 years: Catalyst cost (Ni/$MgAl_2O_3$) from [47] updated with Rogers International Commodity Index for Metals [9].

In the following three subsections the methods applied to calculate the required number of tubes to satisfy heat transfer, kinetics and pressure drop specifications ($n_{tube,\,heat}$, $n_{tube,\,kinetic}$ and $n_{tube,\,pressure}$) are described.

2.4.1. Reaction kinetics

The feed of the RWGS reactor consists mainly of H_2, CO_2, CO, CH_4 and N_2. There is also a small amount of C2+ hydrocarbons in the feed of the reactor (0.4 mol % at 800 °C and 5 bar). As the concentrations are comparably low, the reforming reactions of these short chained C2+ hydrocarbons are neglected in the following approach. This was concluded to be reasonable as the resulting composition at the outlet of the reactor shows no significant difference to the equilibrium composition calculated in Aspen Plus® (see Chapter 3.1). Further, carbon formation is neglected in the kinetics calculations but monitored in the Aspen Plus® process simulation (see in Fig. 8 at which operating conditions carbon formation in form of graphite is observed in the equilibrium calculations).

The reaction is modelled as an isothermal integral reactor (1-D pseudo-homogeneous model). The intrinsic reaction rates are calculated according to Xu and Froment for the following reactions [49]:

$$CH_4 + H_2O \rightleftharpoons 3H_2 + CO \quad (12)$$

$$CO + H_2O \rightleftharpoons CO_2 + H_2 \quad (13)$$

$$CH_4 + 2H_2O \rightleftharpoons 4H_2 + CO_2 \quad (14)$$

The equilibrium constants for the three reactions are calculated according to [50,51]. From the intrinsic reaction rates the effective reaction rates are calculated assuming an effectiveness factor of $\eta = 0.02$ for all reactions (with η being a measure of how diffusion, internal and external mass transfer limitations, reduces the reaction rate - η is approximated conservatively from [46]). The number of tubes is iteratively increased until the sum of the absolute values for the three intrinsic reaction rates at the outlet of the reactor is below a certain value (= 0.1 kmol h^{-1} kg_{Cat}^{-1}, reference value approximated from the intrinsic reaction rates at the outlet of a steam methane reformer in [48]).

2.4.2. Heat transfer

A mean heat flux over the tube length is assumed. An impact of the RWGS operating conditions on this mean heat flux is neglected. The mean heat flux is set to q_{av} = 100 kW/m^2, which is a typical value for steam methane reforming [45].The number of tubes required can be directly calculated from the RWGS heat demand $\dot{Q}_{RWGS}$:

$$n_{tube,h} = \frac{\dot{Q}_{RWGS}}{q_{av}\,\pi\,D_i\,L} \quad (15)$$

It is evident that, higher heat demand and/or inner diameter requires larger tube numbers. It is worth noting that this approach does intrinsically not give results on the optimum tube length as it does not distinguish between for example doubling the length or doubling the number of tubes.

2.4.3. Pressure drop

Higher tube numbers reduce the pressure drop as the volumetric flow rate decreases. The maximum pressure drop allowed is set to 1 bar. The pressure drop is calculated according to Hicks [52,53]. Using Hicks approach, the number of tubes is calculated according to [52]:

$$w_0 = \left(\frac{\Delta p}{L}\,\frac{1}{6.8}D_P^{1.2}\frac{\nu^{0.8}}{\mu}\,\frac{\varepsilon^3}{(1-\varepsilon)^{1.2}}\right)^{1/1.8} \quad (16)$$

$$n_{tube,\Delta p} = \frac{\dot{V}}{\frac{\pi}{4}\,D_i^2\,w_0} \quad (17)$$

with the void fraction of the catalyst bed $\varepsilon = 0.55$ and the equivalent catalyst pellet diameter $D_p = 0.0142$ m [45]. The viscosities (μ, ν) and the volumetric flowrate $\dot{V}$ are extracted from the process simulation.

3. Results and discussion

In the first subchapter, the approach to identifying the design criterion as well as to find the minimum required steel volume is visualized in an example at constant RWGS operating conditions. The latter two chapters discuss the results from the RWGS reactor cost estimation as well as the results from the assessment of the net production costs at varying RWGS operating conditions for different hydrogen cost cases.

A detailed analysis of the process behavior at different RWGS operating conditions is available in [25]. Reducing the RWGS temperature decreases the CO yield and with that increases the inert gas content in the RWGS product stream [25]. In order to keep the inert gas content in the feed of the FT reactor constant, the recycling rates to the FT reactor decrease leading to higher recycling rates to the RWGS reactor [25]. The same may be observed when increasing RWGS pressure [25]. Based on this, higher RWGS pressure and lower RWGS temperature increase the flowrate in the RWGS reactor. This correlation plays an important role in finding the optimum RWGS operating conditions.

3.1. Tube design

The following example aims at visualizing the methodological approach that is described in Fig. 4 and also intends to show the effect of the number of tubes and inner tube diameter on the resulting pressure drop, heat supply and reaction rates. For the sake of simplicity (reduction of dimensions) the example focuses only on identifying the optimum inner tube diameter, whereas the tube length is fixed to 4 m. The example is evaluated at $T_{RWGS} = 800$ °C and $p_{RWGS} = 5$ bar.

3.1.1. Axial partial pressure profiles

Fig. 5 shows the axial partial pressure profiles along the tube length of 4 m. The black dots represent the respective partial pressures derived from the Aspen Plus® simulation through Gibbs minimization. The very small deviation between the equilibrium partial pressures (black dots versus partial pressures at the reactor outlet) may be explained by the fact that a small fraction of C2+ components was not included in the integral reactor model. The partial pressure profiles indicate that the gas composition at the outlet of the reactor is close to equilibrium composition. The reaction rates in the first part of the reactor are very high, leading to steep changes of the reactants' partial pressures. After approximately 1 m the reaction rates decrease significantly. The minimum number of tubes to satisfy the kinetics criterion ($D_i = 0.1$ m) is 179.

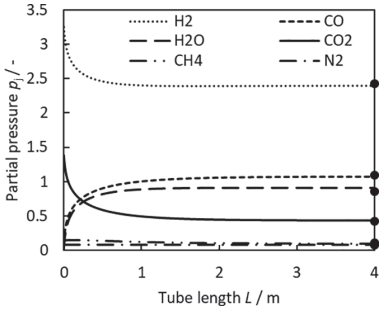

Fig. 5. Partial pressures of the reactants along the reactor tube length. $T_{RWGS} = 800$ °C and $p_{RWGS} = 5$ bar. The number of tubes required are 179 to reach the kinetic criterion. The inner tube diameter is $D_i = 0.1$ m. The dots at reactor length L represent the equilibrium partial pressures extracted from the Aspen Plus® simulation.

As the changes in partial pressures are small at outlet of reactor, and close to the values derived from the Aspen Plus® simulation, the kinetics criterion seems to be in a reasonable range. However, it is worth noting that the independent calculation of kinetics and heat transfer may only be regarded as an approximation as the temperature at the inlet of the tube is far lower than the outlet temperature.

3.1.2. Design criteria assessment

Fig. 6 visualizes how the tube design criterion is identified. Plotted are the normalized values for the occurring heat supply, pressure drop and reaction rates (sum of the absolute intrinsic reaction rates at the outlet of the reactor) as a function of the number of tubes for three different inner tube diameters D_i. Therefore, heat supply, pressure drop and $\sum$ | Intrinsic reaction rates| are normalized by their respective target values − 30.1 MW_{th}, 1 bar and 0.1 kmol h^{-1} kg_{Cat}^{-1}. Thus, the number of tubes required to reach the target values is observed where the normalized values reach unity.

Fig. 6 shows the influence of the number of tubes and inner diameter on heat supply, pressure drop and reaction rates. The heat supply increases with increasing number of tubes and inner diameter as the heat transfer area increases. The pressure drop decreases with increasing number of tubes and inner diameter as the cross sectional area increases. The same applies for the reaction rates at the outlet of the reactor. It is worth reminding that the target here is to reach a reaction rate below a predefined value in order to satisfy a certain approach to equilibrium.

The different grey tones in Fig. 6 represent the different inner tube diameters. For example, black lines represent the results for an inner diameter of 0.1 m. At this diameter, the number of tubes required to fulfill the respective target specifications are 245, 259 and 180, for heat supply, pressure drop and kinetics. Hence, the design criterion in this case is the pressure drop, which is marked with a black dot in Fig. 6. In comparison, the light grey lines represent the results for an inner diameter of 0.2 m. The number of tubes required are 123 (heat), 65 (pressure drop) and 45 (kinetics), with heat transfer limitation consequently being the design criterion at an inner diameter of 0.2 m. To summarize, the number of tubes required are 259 (pressure drop limitation), 165 (heat transfer limitation), 123 (heat transfer limitation) at $D_i = 0.1$ m, $D_i = 0.15$ m and $D_i = 0.2$ m.

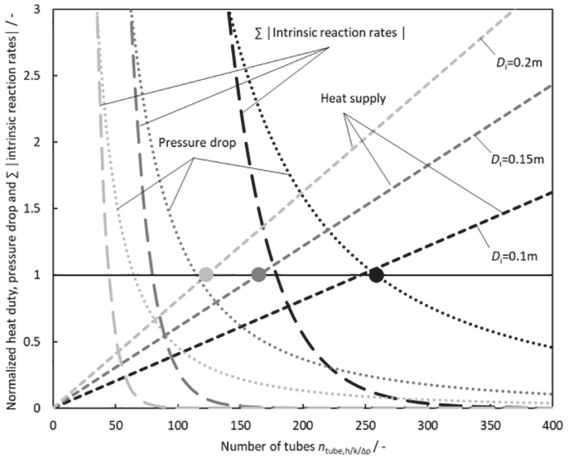

Fig. 6. Normalized heat supply , pressure drop and $\sum$ |Intrinsic reaction rates| as a function of number of tubes for different inner tube diameters D_i. Heat supply, pressure drop and $\sum$ |Intrinsic reaction rates| are normalized by their target values of 30.1 MW_{th}, 1 bar and 0.1 kmol h^{-1} kg_{Cat}^{-1}, respectively. The dots mark the number of tubes that are required for a certain inner tube diameter in order to fulfill the respective design criterion. RWGS operating conditions in this example are $T_{RWGS} = 800$ °C, $p_{RWGS} = 5$ bar and the tube length is set to 4 m.

3.1.3. Optimum inner tube diameter

The next step is to identify the optimum inner tube diameter with respect to the minimum steel demand. Fig. 7 shows the number of tubes, the wall thickness and the resulting steel volume for the three inner tube diameters investigated. The wall thickness rises with larger inner tube diameter, whereas the number of tubes required decreases. Overall, the resulting steel volume increases with increasing inner diameter. From this it is evident that it is not only important to optimize the number of tubes but to optimize the overall amount of steel by taking into consideration the different wall thicknesses at different inner diameters. In this example ($T_{RWGS} = 800$ °C and $p_{RWGS} = 5$ bar) it may be concluded that the optimum inner tube diameter is 0.1 m (at 4 m tube length) and the respective design criterion is the pressure drop (although closely followed by the heat transfer).

3.2. RWGS reactor cost

The following results do not reflect the stand-alone RWGS reactor cost but incorporate the cumulative impact of process and reactor design changes through changes of RWGS operating conditions. Thus, the resulting reactor cost, at a given RWGS pressure and temperature, is only valid for the specified process configuration. In order to understand the resulting RWGS reactor cost, the volumetric flow rate, heat demand, wall thickness, optimum inner diameter and design parameter are discussed in detail (Fig. 8).

Fig. 8 C shows the impact of the RWGS operating conditions on the volumetric flowrate. The volumetric flow rate of the RGWS product increases with decreasing pressure and decreasing temperature. Below a certain RWGS temperature, the volumetric flow rate rises significantly due to considerably higher recycling rates to the RWGS reactor (see the introduction of Chapter 3 for details). Lower RWGS pressures lead to higher volumetric flow rates, as the density reduces with decreasing pressure ($p \propto 1/\dot{V}$).

Fig. 8 B shows the relationship between heat duty and RWGS operating conditions. For a defined RWGS pressure, the heat demand exhibits a minimum at a certain temperature. From this minimum, increasing the temperature increases the heat demand mildly due to the larger temperature difference ($\dot{Q} \propto \Delta T = T_{RWGS} - 450\,^{\circ}C$), while decreasing the temperature increases the heat demand more substantially due to higher recycling rates to the RWGS reactor ($\dot{Q} \propto \dot{m}$).

In general, the wall thickness depends on pressure, temperature and inner diameter (compare Fig. 3). Fig. 8 D, shows the resulting wall thickness for the respective optimum inner diameter (compare Fig. 8 E for the according inner tube diameter). The obtained wall thickness rises significantly at high pressure (> 10 bar) and high temperature combinations, whereas the temperature has only minor impact at low pressure

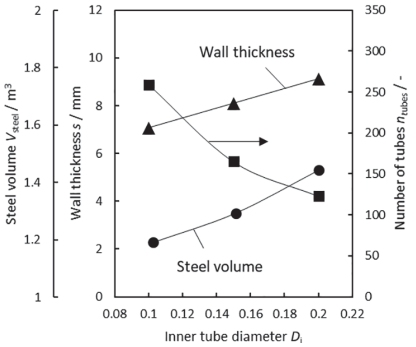

Fig. 7. Resulting steel volume, wall thickness and number of tubes required to fulfill the design criteria at different inner tube diameters (T_{RWGS} = 800 °C, p_{RWGS} = 5 bar).

(≤ 5 bar).

Fig. 8 E exhibits the identified tube design criterion. For low pressure (1 bar), in most cases, the pressure drop is limiting due to the high volumetric flow rates / velocities ($\dot{V} \propto 1/p$). Additionally, kinetics may be the restricting parameter due to low reaction rates at very low temperatures (<650 °C). At intermediate pressure (5–10 bar) pressure drop and heat transfer are the competing design criteria. At 5 bar, starting from low temperatures, first heat transfer is limiting due to the higher recycling rates to the RWGS reactor and thus increased heat demand ($\dot{Q} \propto \dot{m}$), until, in the region of minimum heat demand, the pressure drop becomes the limiting factor. Again, at high temperatures the heat transfer is limiting due to the higher ΔT and hence higher heat demand ($\dot{Q} \propto \Delta T$). At high pressures (10–25 bar) the heat transfer becomes the limiting factor as the pressure drop is reduced due to the higher densities/lower volumetric flow rates ($\dot{V} \propto 1/p$).

Fig. 8 E, also gives the determined optimum inner tube diameter from the parametric optimization. At low pressure (1 bar), large inner diameters ($D_i = 0.2$ m) and short tube lengths ($L = 4$ m) are preferred as these geometries decrease the pressure drop: large diameters decrease the volumetric flow rate per tube and short tube lengths generally decrease the pressure drop (equation (16) and (17)). At high pressures (≥ 10 bar), small diameters are preferred although the heat transfer would be superior at larger diameters (equation (15)). The reason is that the impact of the inner diameter on the wall thickness increases significantly with increasing pressure, especially at high temperature, which in turn leads to high steel volumes (compare Fig. 8 D). Hence, the smaller inner diameter arises from the impact of the wall thickness and not from the heat transfer limitation. It is worth noting that, as the area for heat transfer can either be provided by doubling the tube length or the number of tubes, it is intrinsically not possible to identify the optimum tube length in the heat transfer limited cases. Overall, the number of tubes varies between 150 and 566 (assuming a tube length of 4 m for the heat transfer limited cases).

The grey sections in Fig. 8 E mark the RWGS operating conditions where carbon formation may be expected from thermodynamic considerations (assuming graphite as carbon). From a thermodynamic perspective it seems that carbon formation is likely to occur via Boudouard reaction, which is favored at low temperature and high pressure. However, it is worth noting that carbon formation is also highly dependent on local concentrations and temperatures as well as catalyst properties.

Fig. 8 A exhibits the resulting equipment cost of the RWGS reactor EC_{RWGS}, including furnace, tube and catalyst costs, at different RWGS pressures and temperatures. The cost for furnace and tubes is generally larger than that for the catalyst (2–14 % of EC_{RWGS} is the maximum share observed at 1 bar and 600 °C). Over a broad range of operating pressures (≤ 10 bar) the furnace cost has the largest share of the equipment cost (50–70 %). This shifts at high pressure (25 bar) and temperatures where the tube cost exhibits the largest share (50–65 %). Overall, at high pressure (25 bar) the reactor cost EC_{RWGS} is the highest due to significantly greater wall thickness and thus significantly higher tube cost as well as higher heat demand and hence higher furnace cost. The minimum RWGS reactor cost are found at 1 bar and 700 °C. However, there is a broad range of RWGS temperatures at low pressures (≤ 5 bar) that show only marginal impact on the reactor cost. Below the optimum temperature, the reactor costs increase due to higher recycling rates to the RWGS reactor (higher heat demand and higher volumetric flow lead to higher furnace cost and higher tube cost, respectively). Above the optimum temperature, the reactor cost rises mildly as the wall thickness and the heat demand increase.

3.3. Net production cost in 2019

3.3.1. Cost breakdown

Fig. 9 shows the fixed capital invest, net production cost and direct

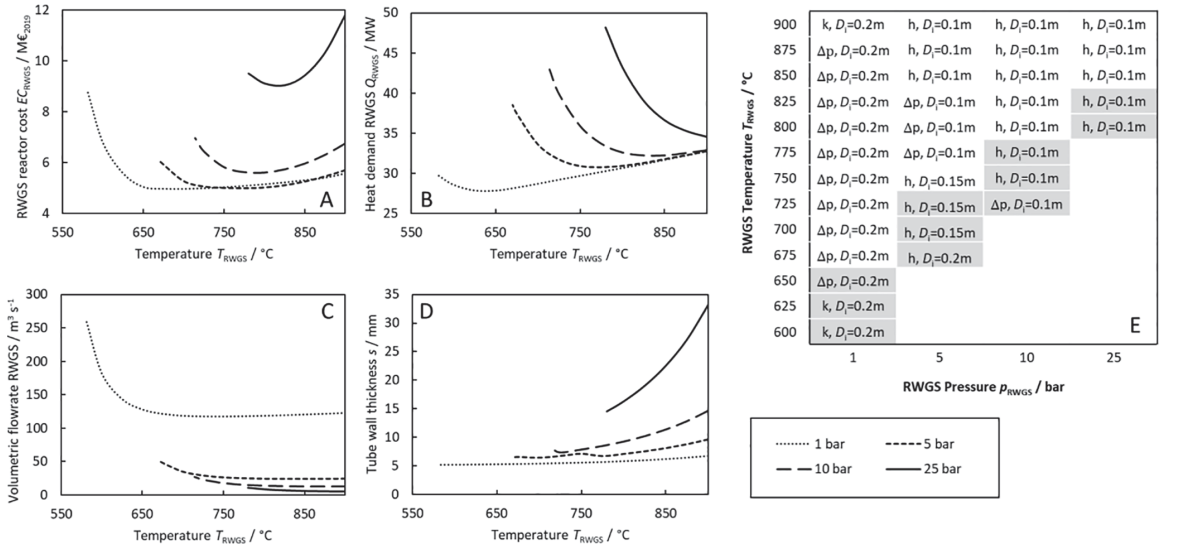

Fig. 8. A: RWGS reactor cost EC_{RWGS}, including furnace, tube and catalyst cost, at different RWGS operating conditions. B: Heat duty required for heating from 450 °C to T_{RWGS} plus heat demand for the endothermic reaction. C: Volumetric flowrate $\dot{V}$ of the RWGS product. D: Tube wall thickness calculated from API 530. E: Limiting factors (Δ*p* - pressure drop, h – heat transfer, k - kinetics) for estimating the tube cost and the optimized inner tube diameter D_i. The grey section expresses the region where carbon formation (as graphite) occurs in the equilibrium calculations.

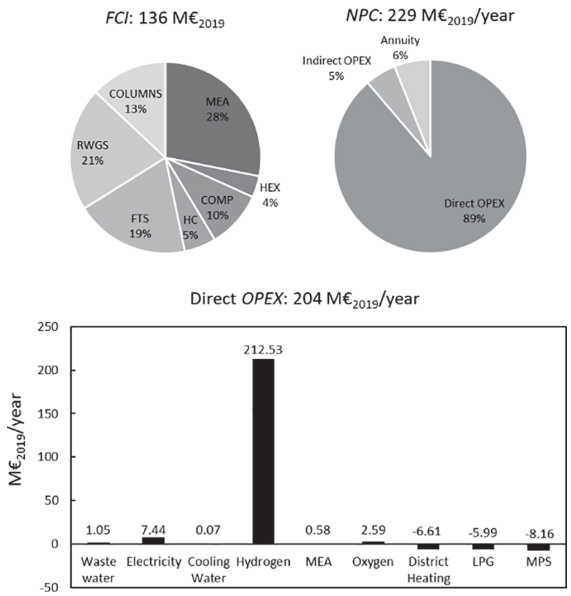

Fig. 9. Fixed capital investment (*FCI*), net production cost (*NPC)* and direct *OPEX* for the case with hydrogen cost of 4.1 €/kg_{H2} and a RWGS temperature of 800 °C and a pressure of 5 bar. Abbreviations: MEA-Monoethanolamine Absorption Unit, FTS-Fischer-Tropsch Synthesis, HC-Hydrocracker, COMP-Compressors, HEX-Heat Exchangers, LPG-Liquefied Petroleum Gas (representing the C1-C4 by-products), MPS-medium pressure steam.

OPEX for a RWGS pressure of 5 bar and a RWGS temperature of 800 °C (base case hydrogen cost of 4.1 €/kg). In this case the *FCI* is 133 million €. Major contributors to the *FCI* are the MEA unit, FT and RWGS reactor. The equipment cost for MEA and FT reactor are based on empirical cost data that scale with the feed/product stream. This seems reasonable as the operating conditions of these units (like pressure, temperature, inert gas content, H_2/CO ratio, conversion) are kept constant at the different RWGS operating conditions. In contrast to this, the operating conditions (pressure, temperature, feed composition) of the RWGS reactor vary. At 5 bar and 800 °C, the RWGS reactor cost is close to the minimum RWGS reactor cost observed in the previous subchapter (compare Fig. 8). The direct *OPEX* are 204 million € per annum. By far the largest share of the direct *OPEX* is accounted for by the hydrogen cost (212 million € per annum). Electricity cost for compression and oxygen cost further add to the direct *OPEX*. Selling the by-products (district heating, C1-C4 product fraction and medium pressure steam) gives a revenue of 20.8 million € per annum. The resulting net production cost is 229 million € per annum or 3.06 €/kg_{C5+}. The largest share of the net production cost arises from the direct *OPEX* and hence from the hydrogen cost. The annuity, representing the *CAPEX*, accounts for only 6 %. Hence, it is evident that the RWGS reactor cost, as well as the remaining equipment cost, constitute only a minor share of the net production cost.

3.3.2. *Impact of RWGS operating conditions and hydrogen cost on the NPC*

As the hydrogen cost is the major contributor to the net production cost, and also may vary substantially depending on the source (see Chapter 2.2), three hydrogen cost scenarios are investigated. The resulting *NPC*s for the different hydrogen cost scenarios and different RWGS operating conditions are shown in Fig. 10.The error bars indicate the 95 % confidence level from the uncertainty analysis (see chapter 2.3). Naturally, the *NPC*s vary significantly for different hydrogen costs (1.8–2.6 €/kg_{C5+} at 2.3 €/kg_{H2}, 3–4.3 €/kg_{C5+} at 4.1 €/kg_{H2} and 5.4–7.9 €/kg_{C5+} at 7.6 €/kg_{H2}). Fig. 10 also depicts the Power-to-Liquid efficiency (assuming 66.7 % efficiency for electrolysis) and the hydrogen efficiency (see [25] for a detailed analysis). Below a certain temperature, the hydrogen efficiency and the PtL efficiency decline drastically with decreasing temperature. Above this temperature, the impact of the RWGS temperature has only minor impact on the energy and hydrogen efficiency. The same influence can be found for the *NPC*, just vice versa. Below a certain RWGS temperature, the *NPC* increases due to lower product output/hydrogen efficiency. Additionally, the electricity required for compression has an effect on the Power-to-Liquid

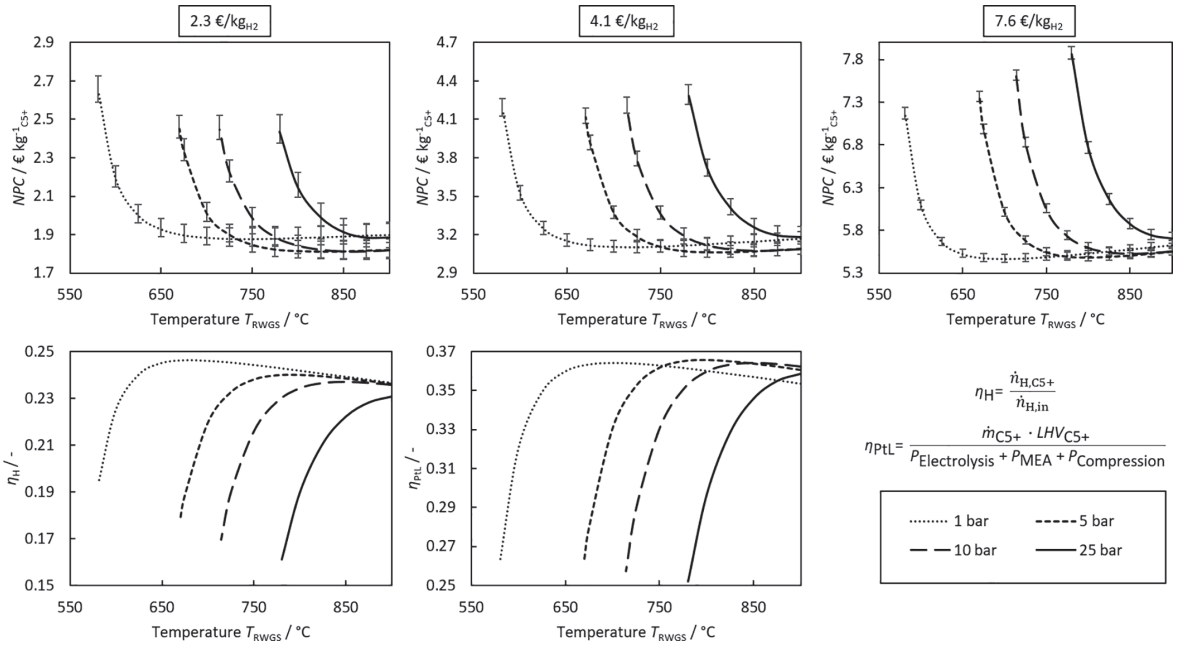

Fig. 10. Top: Syncrude net production cost (C5+) for different hydrogen costs (2.3–7.6 €/kg_{H2}) at varying RWGS operating conditions. Error bars represent the 95 % confidence interval from uncertainty analysis. Bottom right: Power-to-Liquid efficiency η_{PtL} at different RWGS temperatures and pressures. Botton left:Hydrogen efficiency for different RWGS operating conditions. P_{MEA}: Electricity demand for CO_2 recovery, $P_{Electrolysis}$: electrolyzer efficiency assumed to be 66.7 % based on the lower heating value.

efficiency, shifting the optimum from the maximum hydrogen efficiency (at 1 bar) to the optimum at elevated pressure (at 5 bar). This is also reflected in the *NPC*. At low hydrogen cost (2.3 €/kg_{H2}) the impact of the cost for compression is clearly visible (the 1 bar curve is shifted towards higher *NPC*), whereas this becomes less important at high hydrogen cost (7.6 €/kg_{H2}). Hence, the lowest *NPC* is achieved by maximizing the Power-to-Liquid efficiency in case of low hydrogen cost or by maximizing the hydrogen efficiency in case of high hydrogen cost. However, intermediate pressure (e.g. 5 bar) and temperature (e.g. 800–825 °C) allow for low *NPC*s through all hydrogen cost cases, if the uncertainty in hydrogen cost cannot be ruled out. The minimum *NPC*s estimated are 1.81 €/kg_{C5+}, 3.06 €/kg_{C5+} and 5.47 €/kg_{C5+} for 2.3 €/kg_{H2}, 4.1 €/kg_{H2} and 7.6 €/kg_{H2}, respectively. No additional extrema are expected outside the varied RWGS pressure and temperature range.

3.3.3. Comparison with literature data

Table 9 lists the net production costs calculated by other authors for similar processes. As the hydrogen cost is the main contributor to the *NPC*, the *NPC* is recalculated for the different hydrogen costs applied by the respective author. Recalculating the *NPC* with the hydrogen cost from [17] exhibits a good agreement of the *NPC*s. In comparison to the *NPC* calculated by [18], the *NPC* in this work is higher (2.75 €/kg vs. 3.4 €/kg). Further, the Power-to-Liquid efficiency in [18] is significantly higher (50 % vs. 36.6 %). The higher Power-to-Liquid efficiency may explain the lower *NPC*. The difference in energy efficiency may arise from the higher electrolyzer efficiency assumed (70 % vs. 66.7 %) as well as from the difference in RWGS heat supply (electrical heating vs. combustion). Electrical heating has the benefit of less oxygen in the system and hence less water production. This increases the hydrogen efficiency, which may result in a higher energetic efficiency (see [25]). However, the combustion of tail gas has been widely applied in steam methane reforming (= mature technology), which is why this kind of heat supply was chosen in this work.

Table 9
Comparison with literature data. The *NPC*s have been recalculated for the given hydrogen cost in the respective reference (T_{RWGS} = 800 °C and p_{RWGS} = 5 bar). Lower specific costs in [17] representing syncrude production and higher costs representing diesel production.

	Reference €/kgH_2	Reference *NPC* €/kg	This work *NPC* €/kg
Tremel *et al.* [17]	3	2.01–2.34	2.27
Schemme *et al.* [18]	4.6	2.75	3.43

3.3.4. Hydrogen consumption and water production

Hydrogen is converted in different process units within the investigated concept:

- RWGS - activation of CO_2,
- FTS - synthesis of hydrocarbons from CO,
- oxyfuel burner – provision of heat for RWGS by combustion of tail gas and
- hydrocracker - cracking of long chained hydrocarbons.

Overall, most of the molecular hydrogen is converted in the conversion steps (FTS = 54–74 % > RWGS = 21–41 % ≫ hydrocracker ≈ 0.2 %) and only 3.5–5.2 % are converted in the oxyfuel combustion. However, from overall process perspective, this is of little relevance as hydrogen converted to, for example, methane in the FT reactor may still be reformed in the RWGS unit and thus may still end up in the product. In contrast, the water that is produced in the different process units (FTS, RWGS and oxyfuel burner, no water is produced in the hydrocracker) is subsequently lost. The reason is that the water exits the system and therefore the hydrogen incorporated in water is not available to be incorporated in the hydrocarbon product. Consequently, it is more important to analyze the water yield. The water production is rather

equally distributed among the process units: FTS = 29–44 %, RWGS = 36–39 %, oxyfuel = 18–33 %. Within the respective energetic plateaus (compare Fig. 10), the shares do not differ largely. Hence, a representative distribution is shown in Fig. 11 for 800 °C and 5 bar. In this case 21 % of the overall water produced evolves from the oxyfuel burner. The hydrogen demand could therefore be reduced by replacing the oxyfuel combustion with e.g. electrical heat supply. The tail gas used for combustion could then be recycled to the RWGS reactor instead. This affects the RWGS feed composition leading to increased C1+ concentration. It may then be necessary to add a pre-reforming step, as applied in methane steam reforming, depending on the resulting carbon formation affinity. However, it is worth mentioning that, depending on the boundary conditions, it may be more suitable to store and/or transport the electrical energy as hydrogen than to use electricity for heating.

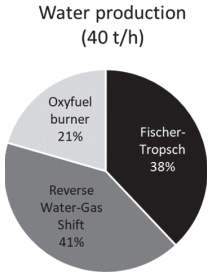

Fig. 11. Water production distribution among the different process units at T_{RWGS} = 800 °C and p_{RWGS} = 5 bar. 40 t/h H_2O are produced in the overall process.

4. Conclusions

The aim of this work was to quantify the impact of different RWGS operating conditions, within the Fischer-Tropsch based PtL process, on the net production cost *NPC*. Therefore, a method was developed to estimate the RWGS reactor cost at varying RWGS pressure and temperature. This method takes into consideration the cost for furnace, tubes and catalyst. Regarding the tube cost, the methodology further allows to identify the design criterion (heat transfer, kinetic or pressure drop limitation) and the optimum tube geometry.

The RWGS operating conditions are varied within the process and the according reactor cost EC_{RWGS} is calculated. Hence, the resulting reactor cost is affected directly (e.g. increasing wall thickness at higher pressures) and indirectly (e.g. by changes in recycling ratios → changes RWGS feed composition and flow rate) by the RWGS operating conditions. The outcomes of the RWGS reactor cost evaluation are:

- Tube design criterion: The minimum number of tubes required may be restricted by heat transfer, kinetic or pressure drop limitation. At low pressure (< 5 bar), the pressure drop defines the number of tubes, while at high pressure (> 5 bar) the system exhibits heat transfer limitations. Kinetic limitations determine the tube number at low temperatures (< 650 °C).
- Optimum tube design: The optimum tube design is defined by the inner diameter and length combination leading to the lowest steel volume. At low pressure, the number of tubes is defined by pressure drop. Hence, short tubes (4 m) and large diameters (0.2 m) are favorable, as both lead to a reduction in pressure drop. At high pressure, the increase in wall thickness becomes dominant. Thus, small diameters (0.1 m) are preferred as they lead to smaller wall thicknesses.
- Reactor cost: The highest reactor cost is observed at high pressure. High pressure (25 bar) leads to high reactor cost due to large wall thicknesses and hence high tube cost, as well as high heat demand and hence furnace cost. Elevated reactor costs are also found at low pressure (1 bar) and temperature (< 600 °C). Below this temperature, the volumetric flowrate increases significantly, leading to higher tube and catalyst cost.

To identify the most economical RWGS operating conditions, the net production costs are calculated at different RWGS temperatures and pressures. The findings are:

- *NPC* cost breakdown: The cost distribution is analyzed for the base case hydrogen cost at T_{RWGS} = 800 °C and p_{RWGS} = 5 bar. The annuity cost accounts for 6 % of the *NPC*. As the annuity is closely related to the overall installed equipment cost, it is evident that the *NPC* should not be significantly affected by changes in RWGS reactor cost (which accounts for 21 % of the *FCI* in the base case). The major contributor to the *NPC* is found to be the hydrogen cost.
- Optimum RWGS operating conditions: Although the RWGS reactor cost affects the *NPC* only marginally, the *NPC* varies significantly with changes in RWGS operating conditions. Hence, the *NPC* is more dependent on the general process performance than on the impact of the actual reactor costs. The reason is that changes in RWGS operating conditions affect the streams in the process, especially the recycling flowrates and compositions and thus the split ratios of the recycle. Three different hydrogen cost cases are analyzed. It is observed that for low hydrogen costs the target should be to maximize the Power-to-Liquid efficiency, whereas at high hydrogen costs the target should focus on maximizing the hydrogen efficiency. Compression work increases with decreasing pressure and temperature, see [25]. At low hydrogen cost, the impact of the costs for compression is higher (share of hydrogen cost decreases → share of compression cost increases). Hence, at low hydrogen cost, intermediate pressures (5–10 bar) are more favorable (less compression work), whereas at high hydrogen cost the impact of the cost for compression almost diminishes - favoring low RWGS pressure (1 bar). Overall, a promising temperature and pressure combination is 800 °C and 5 bar (best case at 4.10 €/kg_{H2}).
- Net production cost: As the hydrogen cost has a large share of the *NPC*, and the hydrogen cost may vary significantly, three different hydrogen cost cases are investigated. The respective minimum *NPC*s estimated are 1.81 €/kg_{C5+}, 3.06 €/kg_{C5+} and 5.47 €/kg_{C5+} for 2.3 €/kg_{H2}, 4.1 €/kg_{H2} and 7.6 €/kg_{H2}.

To conclude, the RWGS reactor may be operated in a broad range of operating conditions without extreme impact on the *NPC*. However, outside these ranges the *NPC* may increase drastically (up to 50 %). Further, the results show that low hydrogen costs are extremely beneficial for the process. Future work should target a more rigorous hydrogen cost analysis, and consequently syncrude production cost analysis, via uncertainty and sensitivity analysis to identify the main drivers for the uncertainty and to quantify the overall impact of the uncertainty.

Declaration of Competing Interest

The authors declare that they have no known competing financial interests or personal relationships that could have appeared to influence the work reported in this paper.

References

[1] Wolff C, Riefer D. Clean Skies for Tomorrow: Sustainable Aviation Fuels as a Pathway to Net-Zero Aviation. World Economic Forum, 2020.
[2] NBC, *We make transportation green.* 2021.
[3] Schmidt P, et al. Power-to-Liquids as Renewable Fuel Option for Aviation: A Review. Chem Ing Tech 2018;90(1–2):127–40.
[4] Estelmann S, Dietrich R-U, Seitz A. *Flexibilitätsoptionen in der Grundstoffindustrie Methodik| Potenziale| Hemmnisse.* 2018: Kopernikus-Projekt „SynErgie –

Synchronisierte und energieadaptive Produktionstechnik zur flexiblen Ausrichtung von Industrieprozessen auf eine fluktuierende Energieversorgung".
[5] *IEA Greenhouse Gas R&D Programme (IEA GHG): CO2 Capture in the Cement Plant Industry*. 2008.
[6] Luque R, et al. Design and development of catalysts for Biomass-To-Liquid-Fischer–Tropsch (BTL-FT) processes for biofuels production. Energy Environ Sci 2012;5(1):5186–202.
[7] Vázquez FV, et al. Power-to-X technology using renewable electricity and carbon dioxide from ambient air: SOLETAIR proof-of-concept and improved process concept. J CO2 Util 2018;28:235–46.
[8] Verdegaal WM, Becker S, Olshausen CV. Power-to-Liquids: Synthetic Crude Oil from CO2, Water, and Sunshine. Chem Ing Tech 2015;87(4):340–6.
[9] KIT, *Kohlendioxidneutrale Kraftstoffe aus Luft und Strom*, in *Von der Bundesregierung gefördertes Kopernikus-Projekt P2X: Integrierte Versuchsanlage im Containermaßstab stellt Kraftstoffe aus Kohlendioxid der Luft und Ökostrom her*. 2019, Karlsruher Institut für Technologie (Press Release): www.kit.edu.
[10] Sunfire, *Erste kommerzielle Blue Crude-Produktion entsteht in Norwegen*. 2017, Sunfire GmbH (Press Release): www.sunfire.de.
[11] FVV, *E-Crude-Produktion in Norwegen - Blaues Rohöl*. 30.04.2020, Forschungsvereinigung Verbrennungskraft-maschinen e.V. (Press Release): https://www.primemovers.de/de/handeln/blaues-oel.
[12] Dieterich V, et al. Power-to-liquid via synthesis of methanol, DME or Fischer–Tropsch-fuels: a review. Energy Environmental Science 2020;13(10):3207–52.
[13] Herz G, Reichelt E, Jahn M. Techno-economic analysis of a co-electrolysis-based synthesis process for the production of hydrocarbons. Appl Energy 2018;215:309–20.
[14] Becker W, et al. Production of Fischer-Tropsch liquid fuels from high temperature solid oxide co-electrolysis units. Energy 2012;47(1):99–115.
[15] Fasihi M, Bogdanov D, Breyer C. *Techno-economic assessment of power-to-liquids (PtL) fuels production and global trading based on hybrid PV-wind power plants*. Energy Procedia, 2016. **99**(10th International Renewable Energy Storage Conference, IRES 2016): p. 243-268.
[16] Cinti G, et al. Integration of Solid Oxide Electrolyzer and Fischer-Tropsch: A sustainable pathway for synthetic fuel. Appl Energy 2016;162:308–20.
[17] Tremel A, et al. Techno-economic analysis for the synthesis of liquid and gaseous fuels based on hydrogen production via electrolysis. Int J Hydrogen Energy 2015;40(35):11457–64.
[18] Schemme S, et al. H2-based synthetic fuels: A techno-economic comparison of alcohol, ether and hydrocarbon production. Int J Hydrogen Energy 2020;45(8):5395–414.
[19] Albrecht FG, et al. A standardized methodology for the techno-economic evaluation of alternative fuels–A case study. Fuel 2017;194:511–26.
[20] König DH, et al. Techno-economic study of the storage of fluctuating renewable energy in liquid hydrocarbons. Fuel 2015;159:289–97.
[21] Marchese M, et al. CO2 from direct air capture as carbon feedstock for Fischer-Tropsch chemicals and fuels: Energy and economic analysis. J CO2 Util 2021;46:101487.
[22] Kondratenko EV, et al. Status and perspectives of CO 2 conversion into fuels and chemicals by catalytic, photocatalytic and electrocatalytic processes. Energy Environ Sci 2013;6(11):3112–35.
[23] Baliban RC, Elia JA, Floudas CA. Toward novel hybrid biomass, coal, and natural gas processes for satisfying current transportation fuel demands, 1: Process alternatives, gasification modeling, process simulation, and economic analysis. Ind Eng Chem Res 2010;49(16):7343–70.
[24] Klara J, et al., Cost Performance Baseline for Fossil Energy Plants: Bituminous Coal and Natural Gas to Electricity (DOE/NETL-2007/1281). 2007.
[25] Adelung S, Maier S, Dietrich R-U. Impact of the reverse water-gas shift operating conditions on the Power-to-Liquid process efficiency. Sustainable Energy Technol Assess 2021;43:100897.
[26] *API 530: Calculation of Heater Tube Thickness in Petroleum Refineries*. 2008, American Petroleum Institute.
[27] Peters MS, Timmerhaus KD, West RE. *Plant design and economics for chemical engineers*. Vol. 4. 2003: McGraw-Hill New York.
[28] Prakash A, Bendale PG. *Comparison of slurry versus fixed-bed reactor costs for indirect liquefaction applications*. 1991, Viking Systems International, Pittsburgh, PA (United States).
[29] Bechtel, *Aspen Process Flowsheet Simulation Model of a Battelle Biomass-Based Gasification, Fischer–Tropsch Liquefaction and Combined-Cycle Power Plant*. 1998, US Department of Energy (DOE) Pittsburgh, Pennsylvania.
[30] Bertuccioli L, et al. Development of Water Electrolysis in the European Union. Lausanne: Fuel Cells and Hydrogen Joint Undertaking; 2014.
[31] Brändle G, Schönfisch M, Schulte S. Estimating long-term global supply costs for low-carbon hydrogen. Appl Energy 2021;302:117481.
[32] Schorn F, et al. Methanol as a renewable energy carrier: An assessment of production and transportation costs for selected global locations. Advances in Applied Energy 2021;3:100050.
[33] *Competitiveness of green hydrogen import pathways for Germany in 2025*. 2021; Available from: http://www.energymailer.de/filestore/newsimgorg/Illustrationen_Stimmungsbilder/Studien_als_PDF/Competitiveness_of_green_hydrogen_import_pathways_for_Germany_in_2025.orig.pdf.
[34] Timmerberg S, Kaltschmitt M. Hydrogen from renewables: Supply from North Africa to Central Europe as blend in existing pipelines–Potentials and costs. Appl Energy 2019;237:795–809.
[35] Eurostat. *Electricity prices for non-household consumers - bi-annual data (from 2007 onwards) NRG_PC_205*. [cited 2021.
[36] *Umweltgebührenordnung (UmwGebO)-Zehnte Verordnung zur Änderung der Umweltgebührenordnung*, H. Bürgschaft, Editor. 2014, Hamburg.
[37] Bennett DL, *Appendix B: Carbon Dioxide Capture Technology: Sheet - Oxygen Production*, in *DOE/NETL Advanced Carbon Dioxide Capture R&D Program: Technology Update*. 2013, National Energy Technology Laboratory (NETL). p. B-512.
[38] Fränkle, C., *Heizkostenvergleich nach VDI 2067-Musterrechnung*. 2015, AGFW Energieeffizienzverband für Wärme, Kälte und KWK e.V.: Franfurt am Main.
[39] Eurostat, *Gas prices for non-household consumers - bi-annual data (from 2007 onwards): NRG_PC_203.*.
[40] Statista. *Liquefied petroleum gas (LPG) price in the Netherlands from 2009 to 2020*. Available from: https://www.statista.com/statistics/658367/liquefied-petroleum-gas-price-in-the-netherlands/.
[41] Joe S, Kuo F. *File implemented: new-joe-kuo-6.21201 as recommended by the authors*. 2010; Available from: https://web.maths.unsw.edu.au/~fkuo/sobol/.
[42] Bredehoef PR, Dysert LR, Hollmann JK. Cost Estimate Classification system-as applied in engineering, procurement, and construction for the process industries: TCM Framework: 7.3 – Cost Estimating and Budgeting, in AACE International Recommended Practice No. 18R-97. 2019, AACE International.
[43] Schwab E, et al. Dry reforming and reverse water gas shift: alternatives for syngas production? Chem Ing Tech 2015;87(4):347–53.
[44] Schmidt P, et al., *Power-to-liquids: Potentials and perspectives for the future supply of renewable aviation fuel*. 2016: German Environment Agency.
[45] Rostrup-Nielsen J, Christiansen LJ. *Concepts in Syngas Manufacture*. Catalytic science series, ed. G.J. Hutchings. Vol. Catalytic science series. 2011, Denmark: Imperial College Press, London.
[46] Wolf A, Jess A, Kern C. Syngas Production via Reverse Water-Gas Shift Reaction over a Ni-Al2O3 Catalyst: Catalyst Stability, Reaction Kinetics, and Modeling. Chemical Engineering Technology 2016;39(6):1040–8.
[47] Davis, B. and C. Okorafor, *Design and Economic Analysis of a Hydrogen Fueling Station*, in *ChE161.2 Process Evaluation and Design II*. 2012, C Squared Consulting LLP: New York.
[48] Xu J, Froment GF. Methane steam reforming: II. Diffusional limitations and reactor simulation. AIChE J 1989;35(1):97–103.
[49] Xu J, Froment GF. Methane steam reforming, methanation and water-gas shift: I. *Intrinsic kinetics*. AIChE journal 1989;35(1):88–96.
[50] Abbas SZ, Dupont V, Mahmud T. Kinetics study and modelling of steam methane reforming process over a NiO/Al2O3 catalyst in an adiabatic packed bed reactor. Int J Hydrogen Energy 2017;42(5):2889–903.
[51] Sadooghi P, Rauch R. Experimental and modeling study of hydrogen production from catalytic steam reforming of methane mixture with hydrogen sulfide. Int J Hydrogen Energy 2015;40(33):10418–26.
[52] Hicks RE. Pressure drop in packed beds of spheres. Industrial Engineering Chemistry Fundamentals 1970;9(3):500–2.
[53] Froment GF, Bischoff KB, De Wilde J. Chemical reactor analysis and design, Vol. 2. New York: Wiley; 1990.

Paper 3

Global sensitivity and uncertainty analysis of a Fischer-Tropsch based Power-to-Liquid Process

Sandra Adelung

The following research paper was published in
Journal of CO2 Utilization
Volume 65, November 2022, 102171
https://doi.org/10.1016/j.jcou.2022.102171

Journal of CO2 Utilization 65 (2022) 102171

Contents lists available at ScienceDirect

Journal of CO2 Utilization

journal homepage: www.elsevier.com/locate/jcou

Global sensitivity and uncertainty analysis of a Fischer-Tropsch based Power-to-Liquid process

Sandra Adelung

German Aerospace Center (DLR), Pfaffenwaldring 38-40, 70569 Stuttgart, Germany

ARTICLE INFO

Keywords:
Alternative fuels
Synthetic fuels
Process analysis
Sobol indices

ABSTRACT

A workflow to conduct a combined uncertainty and global sensitivity analysis supplementing techno-economic process analysis is depicted and applied in this work. Furthermore, different estimators for conducting the variance-based global sensitivity analysis are compared with respect to their computational effort. The model under investigation is a Fischer-Tropsch based Power-to-Liquid process that allows to produce syncrude from electricity, water and carbon dioxide. One of the major contributors to the uncertainty of the net production cost is found to be the full load hours of the electrolyzer. Reducing the full load hours of the electrolyzer reduces the cost for electricity, as the average wholesale electricity price decreases assuming that the electrolyzer is operated at the cheaper hours within the year. However, it also results in increased storage cost and cost for oversizing of the electrolyzer. The results indicate, that the reduced costs for electricity do not outweigh the additional costs for storage and electrolyzer oversizing. Thus, the lowest net production cost is observed at maximum full load hours of the electrolyzer. The base case syncrude net production cost for the plant situated in Germany is 3.89 $€_{2019}$ /kg_{C5+} (5.47 $€_{2019}$/kg_{H2}). The resulting 95 % confidence interval, after fixing the full load hours of the electrolyzer to 8 000 h/a, is between 2.79 and 5.29 $€_{2019}$/kg_{C5+}.

1. Introduction

Decarbonization of the transport sector is a major challenge for human kind in order to reduce the anthropogenic impact on the world's climate [1]. Within the transport sector, ships, heavy trucks and air transport are considered to remain hard to electrify – at least in the near future [1]. Additionally, storage is an issue arising from the volatile production of renewable electricity. Fischer-Tropsch (FT) based hydrocarbons have a high volumetric energy-density, which leads to several benefits regarding storage, transport and the actual usage [2]. However, the cost for the production of these FT based e-fuels is still high and heavily dependent on the electricity price for the actual hydrogen production [3]. Therefore, one aim of this work is to investigate whether it is economically beneficial to reduce the full load hours of the electrochemical hydrogen production in order to reduce the cost for electricity. Consequently, the process under investigation is split into two parts, one part that provides hydrogen and one part that converts this hydrogen with carbon dioxide to synthetic hydrocarbons in a reverse water-gas shift reaction and a subsequent Fischer-Tropsch synthesis. Hydrogen is produced via water electrolysis. The annual full load hours of the electrolyzer are assumed to be variable between 2 000 and 8 000 h/a. Reducing the full load hours of the electrolyzer on the one hand reduces the wholesale electricity price (see chapter 2.4) while on the other hand it increases the cost for the electrolyzer through oversizing. Hence, the decision on the optimum full load hours is not straight forward and requires a detailed investigation.

While conducting an economic evaluation, it becomes evident that there is a range of uncertainty in the input data. For example, as the optimum full load hours are not known, these full load hours may be considered as an uncertain decision variable in the beginning of the analysis. Generally, including such decision variables in a sensitivity analysis allows to prioritize the researcher's subsequent effort for further investigations. Apart from uncertainty through uncertainty in decision making there is uncertainty for example in the underlying cost data for the equipment, cost factors or raw materials that are used to calculate the net production cost. Performing an uncertainty analysis allows to quantify the overall uncertainty of the net production cost. Allocation of the overall uncertainty to the different uncertain input variables helps the evaluator to analyze and process the outcome of the uncertainty analysis. This allocation can be provided by a sensitivity analysis. Therefore, uncertainty and (global) sensitivity analysis are usually conducted in tandem [4].

As previously stated, uncertainty analysis (UA) targets to quantify

https://doi.org/10.1016/j.jcou.2022.102171
Received 19 May 2022; Received in revised form 28 July 2022; Accepted 3 August 2022
Available online 19 September 2022

Abbreviations

C-j	compressor *j*.
Cj	hydrocarbon with *j* carbon atoms.
Cj+	fraction of hydrocarbons with at least *j* carbon atoms.
COMP	compressors and pumps.
EEG	surcharge to support development of renewable electricity.
FF	factor fixing.
FP	factor prioritization.
FT(S)	Fischer-Tropsch (synthesis).
GSA	Global Sensitivity Analysis.
H2tL	Hydrogen to Liquid part of the plant.
HC	hydrocracker.
HEX-j	heat exchanger *j*.
IV	input variable.
KWK	surcharge to support development of electricity from combined heat and power generation.
LPG	liquefied petroleum gas.
MC	Monte-Carlo.
MEA	monoethanolamine.
MPS	medium pressure steam.
NEV	surcharge to aid industries with high electricity demand.
PO	plant overhead cost.
POX	partial oxidation.
PtL	Power-to-Liquid.
QMC	Quasi Monte-Carlo.
RND	pseudo-random sampling.
RWGS	reverse water-gas shift.
S-j	split *j*.
UA	Uncertainty Analysis.
V-j	valve *j*.
WHB	waste heat boiler.

Variables and constants (Greek characters)

$\varepsilon_{Si,j}$, $\varepsilon_{STi,j}$	measure for convergence of the sensitivity indices for sample size *j*.
$\varepsilon_{\sigma,j}$	measure for convergence of the standard deviation for sample size *j*.
σ_j	standard deviation at sample size *j*.
η_H	hydrogen efficiency.
η_{PtL}	Power-to-Liquid efficiency.

Variables and constants (Latin characters)

$\boldsymbol{A}$, $\boldsymbol{B}$	sampling matrix with the size N *x* k.
$\boldsymbol{A}_{\boldsymbol{B}}^{(i)}$, $\boldsymbol{B}_{\boldsymbol{A}}^{(i)}$	$\boldsymbol{A}_{\boldsymbol{B}}^{(i)}$ - ith column of matrix $\boldsymbol{A}$ replaced by the *i*th column of matrix $\boldsymbol{B}$.
ACC	annualized capital cost.
CAPEX	capital expenditures.
C_{Cavern}	cavern cost for storing hydrogen and oxygen.
CEPCI	chemical engineering plant cost index.
CI	confidence interval.
C_{labor}	labor cost.
C_{Stack}	stack cost.
$C_{Stack\ replacement}$	cost for stack replacement.
EC_i	equipment cost of equipment *i*.
$EC_{Ref,i}$	equipment cost of reference equipment *i*.
$\boldsymbol{f(A)_j}$, $\boldsymbol{f(B)_j}$, $f(\boldsymbol{A}_{\boldsymbol{B}}^{(i)})_j$, $f(\boldsymbol{B}_{\boldsymbol{A}}^{(i)})_j$	returned function value for sample *j*.
FCI	fixed capital investment.
$F_{eco,i,j}$	economic factor *j* ($j = 1 \ldots 12$) for equipment *i*.
FLH_{elec}	full load hours of the electrolyzer.
FLH_{H2tL}	full load hours H2tL part of plant.
IR	interest rate.
k	number of uncertain input variables.
LHV_{C5+}	lower heating value of C5 + product fraction.
$\dot{m}_{c5+}$	mass flow C5 + product.
N	sample size.
NPC	net production cost.
OPEX	operational expenditures.
$OPEX_{dir}$	direct operational expenditures.
$OPEX_{indir}$	indirect operational expenditures.
p	pre-factor used to compare estimators for GSA.
$P_{compression}$	electricity for compression.
$P_{electrolysis}$	electricity for electrolysis.
P_{MEA}	electricity for MEA.
S_i	first-order/ main effect index of input variable *i*.
SL	electrolyzer stack lifetime.
S_{Ti}	total order/ effect index of input variable *i*.
T_{CI}	threshold 95 % confidence interval.
T_{FF}	threshold for factor fixing.
Y	model to be analyzed, here: model for calculating the *NPC*.
y	operating time of H2tL part of plant.

the overall uncertainty arising from a set of uncertain input variables. In other words, the aim is to calculate the combined probability function from the set of input probability functions. The joint probability may be obtained from Monte-Carlo (MC) propagation or classical error propagation methods (derivative based). The Monte-Carlo approach is a derivative-free black-box approach. The resulting probability distribution is an approximation and requires larger computational effort in comparison to the derivative based method [5,6]. Strictly, an exact solution may only be derived under specific circumstances, namely by applying the derivative based method for linear systems with input functions exclusively consisting of normal distributions [5,6]. However, the MC method is able to cope with different kinds of probability distributions (not limited to normal distributions) and has no limitation to linear models [5,6]. Due to its broader applicability, MC is applied quite frequently in UA [5,6]. The MC approach is used in this work, as it is state-of-the-art in the field of UA.

Once the uncertainty is quantified via UA, the question arises on how the output uncertainty may be allocated to the different input variables. The knowledge on how much each input variable contributes to the output uncertainty for example helps to decrease the number of input variables by fixing them. This reduces the dimensionality and consequently reduces the complexity. Beyond that, ranking the input variables according to their contribution to the overall output uncertainty aids for example to prioritize subsequent research work. The first setting is known as factor fixing FF and the second as factor prioritization FP. Both settings may for example be answered by variance-based global sensitivity analysis. With this probabilistic method main and total order Sobol indices (S_i and S_{Ti}, respectively) are calculated to answer the two predefined settings. As a result, large main order indices indicate that an input variable has a high priority, whereas sufficiently small total order indices point out the input variables that could be considered for factor fixing. The approach allows the analysis of the whole parameter input space (global analysis) and is also able to deal with nonlinear model behavior and interactions among the input variables (non-additivity of a model). More information on the settings, variance decomposition and the derivation of the Sobol indices is available for example in [4,7]. Local sensitivity analysis, or one-at-a-time analysis, is most often applied by practitioners due to its simplicity in the implementation and comprehension of the results [8]. However, it is well known that this is bad-practice if the model features nonlinearities and interactions [8].

Uncertainty and especially global sensitivity analysis are used rather

sparsely in techno-economic assessments for alternative fuel production routes. More commonly local sensitivity or one-factor-at-a-time analyses are conducted. Still, there are publications complementing or solely focusing on the assessment of global UA and GSA. For example, some fields where UA and/or GSA are applied are biomass-based processes [9–16], carbon capture and storage [17–21], energy system analysis [22], wind farms [23] and photovoltaics [24,25]. All of these studies include UA and a few also feature global sensitivity analysis. To the author's knowledge, no publication is available that investigates the uncertainty of a Fischer-Tropsch based Power-to-Liquid process nor one that investigates the sensitivity of net production cost globally. Nevertheless, similar PtL processes have been economically investigated [26–28]. However, none of the other works explores the impact of the electrolyzer full load hours on the wholesale electricity price, electrolyzer cost, hydrogen storage cost and stack replacement cost and finally the resulting net production cost.

In this work, a workflow to conduct the combined uncertainty and global sensitivity analysis in the field of techno-economic process analysis of alternative fuel production routes is shown. The aim is further to sensitize on the usage of one-at-a-time versus global sensitivity analyses. Regarding the variance-based global sensitivity analysis, several estimators are available in the literature to estimate Sobol indices (see e.g. [29,30]). In this work, three estimators for calculating the main and total order indices, respectively, are compared with respect to their computational effort. Additionally, two different sampling strategies are investigated. The methodological advances to arise from this work are thus

- the identification of the estimator to conduct GSA at lowest computational effort,
- the identification of the sampling method for fast convergence and
- to depict an intuitive workflow to conduct combined GSA and UA.

Moreover, this is the first work to investigate the uncertainty of the net production cost of a FT based Power-to-Liquid process. In the context of this process this work targets:

- to identify and fix non-influential input variables to reduce the complexity (here the first dataset contains more than 60 input variables),
- to prioritize the important input variables with respect to their impact on the overall uncertainty (here to identify the main contributors to the uncertainty of the net production cost),
- to analyze important decision variables in order to fix them to their most beneficial value (here the full load hours of the electrolyzer will emerge as an important decision variable),
- to answer the question if a reduction of electrolyzer full load hours benefits the net production cost and.
- to finally quantify the remaining uncertainty of the net production cost after fixing the decision variable(s) and non-influential input variables.

2. Methodology

The following chapter constitutes of four subchapters. The first subchapter covers the general workflow to assess UA and GSA, while the second evolves around the different estimators used for calculating the Sobol indices. The third subchapter describes the Power-to-Liquid process model and the last depicts the approach to calculate the net production cost. Furthermore, the input data required for the deterministic model as well as the probabilistic analysis is summarized in the last subchapter.

2.1. Uncertainty and global sensitivity analysis: workflow

The workflow for combined UA and GSA is shown in Fig. 1 and the different steps are described more in detail in this subchapter.

a) First, the input variables to be incorporated in the uncertainty

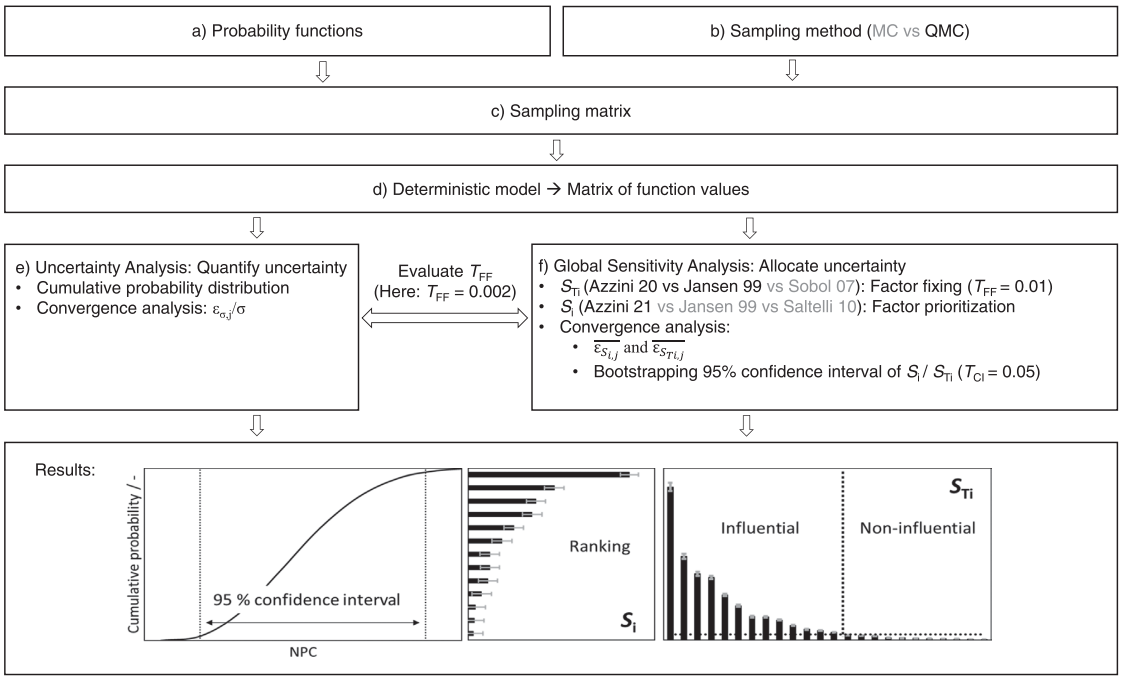

Fig. 1. Workflow for uncertainty and global sensitivity analysis. In brackets the different possibilities investigated in this study – grey tones highlight the inferior solution, observed in this work.

analysis need to be specified. Secondly, probability functions for these input variables need to be defined in order to have a correlation of the input variable value with its probability. The probability distributions may be for example rectangular, triangular or normal distributions depending on the nature of the input variables. Data on the uncertainty of a specific input variable may be gathered e.g. from the source that provides the base case value, through statistical analysis of further available literature data or with the use of expert judgment. Naturally, the resulting uncertainty of the model output relies heavily on the input probability functions that are considered in this step [8]. It is evident that this is a very important and challenging step in the overall uncertainty and sensitivity analysis procedure. See [17] for more information on the creation of the probability distributions and chapter 2.4 for the probability functions used in this work.

b) - d) Both, UA and GSA, rely on a sampling matrix. The input for the sampling matrix can be provided by pseudo-random sampling (Monte-Carlo MC) or quasi-random sampling (quasi Monte-Carlo QMC) within a unit hypercube. Pseudo-random sampling targets at generating patternless numbers. Here, in the case of pseudo-random sampling, the RND function provided by Excel is used. In contrast to pseudo-random sampling, the quasi-random sampling is not random at all. Low-discrepancy sequences, such as Sobol and Halton, are often found to exhibit a faster convergence than pseudo-random sampling. In this work, Sobol sequence is implemented as QMC method. Starting values for building the sequence (Gray code) are taken from [31]. The sampling matrix is of the dimension of the number of samples N and two times the number of input variables k (Nx2k). The 2k arises from the fact that two matrices are required to conduct the GSA, $\boldsymbol{A}$ and $\boldsymbol{B}$, see Table 1. Hence, the first k-columns are dedicated to matrix $\boldsymbol{A}$ and the remaining k-columns to matrix $\boldsymbol{B}$. From the sampling matrix, the function evaluations (model runs) are computed – N for matrix $\boldsymbol{A}$ and N for matrix $\boldsymbol{B}$, hence, returning 2 N function values. These function values are used for UA and GSA. Thus, with the same computational effort, the apparent sample size is N for GSA and 2 N for UA. Depending on the estimators, further model evaluations are required to calculate the matrices $\boldsymbol{A}_{\boldsymbol{B}}^{(\boldsymbol{i})}$ and/or $\boldsymbol{B}_{\boldsymbol{A}}^{(\boldsymbol{i})}$. In case of $\boldsymbol{A}_{\boldsymbol{B}}^{(\boldsymbol{i})}$ the ith column of matrix $\boldsymbol{A}$ is replaced by the ith column of matrix $\boldsymbol{B}$.

e) UA uses the function values derived from matrix $\boldsymbol{A}$ and $\boldsymbol{B}$: $f(\boldsymbol{A})_j$ and, $f(\boldsymbol{B})_j$with $j = 1 \ldots N$. Reordering and creating suitable intervals yields the cumulative probability distribution of the model output – from which for example confidence intervals or the standard deviation σ may be calculated. In order to evaluate and visualize the convergence of the UA, $\varepsilon_{\sigma,j}$ is calculated, representing the stochastic convergence of the standard deviation [32]. Therefore, 2 N standard deviations are calculated from a sample size of one to the maximum sample size of 2 N. From these, the maximum absolute difference, for a given sample size j, is calculated: $\varepsilon_{\sigma,j} = \sup_s \; |\sigma_j\text{-}\sigma_s|$ with $s = j\text{-}4, j\text{-}3, \ldots, 2N$. In order to get a relative value, this is further normalized with the standard deviation σ from the maximum sample size 2 N.

f) As the settings in this work are factor prioritization and fixing, the main and total order indices, S_i and S_{Ti}, are calculated. The following subchapter 2.2 describes how the sensitivity indices are calculated from the matrices derived in step d). Chapter 2.2 also introduces the different estimators under investigation. The key performance indicator to compare the different estimators is the computational effort required to reach stochastic convergence. Convergence is assumed when all i individual 95 % confidence intervals for S_i/S_{Ti} reach a certain threshold [33]. Increasing the sample size N reduces the 95 % confidence interval. Hence, the sample size where all i 95 % confidence intervals are below the threshold of $T_{CI} = 0.05$ [33] marks the sample size with a convergent solution. Small confidence intervals are not only helpful to reach stochastic convergence but are also beneficial for clearer rankings as less overlaps between der sensitivity indices are observed. Bootstrapping is conducted to obtain the 95 % confidence interval for each of the i sensitivity indices S_i/S_{Ti} [34]. The sample size for bootstrapping is equal to the actual sample size for calculating S_i/S_{Ti} and the number of resamples is 1 000. Furthermore, $\overline{\varepsilon_{S_{ij}}}$ and $\overline{\varepsilon_{S_{Tij}}}$ are calculated to asses and visualize the stochastic convergence and compare the different sampling methods. This is conducted similarly to the calculation of $\varepsilon_{\sigma,j}$: $\varepsilon_{S_{ij}} = \sup_s \; |S_{i,j}\text{-}\, S_{i,s}|$ with $s = j\text{-}4, j\text{-}3, \ldots, N$. Hence, for a given sample size j, a set of $\varepsilon_{S_{ij}}$ and $\varepsilon_{S_{Tij}}$ is established. In order to have one single performance indicator, the mean value over all input variables is calculated: $\overline{\varepsilon_{S_{ij}}} = \frac{1}{k}\sum_{i=1}^{k}\varepsilon_{S_{ij}}$ and $\overline{\varepsilon_{S_{Tij}}} = \frac{1}{k}\sum_{i=1}^{k}\varepsilon_{S_{Tij}}$. In order to validate the findings from factor fixing, plausibility checks are conducted to ensure that the predefined threshold of $T_{FF} = 0.01$ leads to satisfying results. Therefore, all input variables with small S_{Ti}, below the predefined threshold of 0.01, are fixed and the impact on the cumulative probability distribution is analyzed. In this work, the predefined threshold is found to be too high (see chapter 3.3). The results indicate an appropriate $T_{FF} \leq 0.002$ to be reasonable for factor fixing in order to still obtain a similar variance as observed prior factor fixing.

2.2. Global sensitivity analysis: settings and estimators

Global sensitivity analysis is conducted for the following settings

- S_i: Factor prioritization (FP) → Ranking.
- S_{Ti}: Factor fixing (FF) → Screening.

Table 1
Nominator and denominator to calculate first and total sensitivity indices S_i and S_{Ti}, respectively. N-sample size, k-number of input variables or dimensionality. For a fair comparison the sample size for the Azzini estimators is half the sample size compared to the remaining estimators: $N_{Azz} = N/2$.

Nominator for S_i: $V_{X_i}(E_{X_{\sim i}}(Y\|X_i))$ =			**Cost of evaluation**	**Pre-factor p=**	**Denominator**	**Source**
Saltelli 10	$\frac{1}{N}\sum_{j=1}^{N} f(\boldsymbol{B})_j (f(\boldsymbol{A}_{\boldsymbol{B}}^{(i)})_j - f(\boldsymbol{A})_j)$	(i)	$N(k+2)$	N	Saltelli 08	[30]
Jansen 99	$V(Y) - \frac{1}{2N}\sum_{j=1}^{N} (f(\boldsymbol{B})_j - (f(\boldsymbol{A}_{\boldsymbol{B}}^{(i)})_j)^2$	(ii)	$N(k+2)$	N	Saltelli 08	[37]
Azzini 21	$2\sum_{j=1}^{N} (f(\boldsymbol{A})_j - f(\boldsymbol{A}_{\boldsymbol{B}}^{(i)})_j)(f(\boldsymbol{B}_{\boldsymbol{A}}^{(i)})_j - f(\boldsymbol{B})_j)$	(iii)	$2N(k+1)$	$2\,N_{Azz}$	Azzini 20	[38]
Nominator for S_{Ti}: $E_{X_{\sim i}}(V_{X_i}(Y\|\boldsymbol{X}_{\sim i}))$ =						
Sobol 07	$\frac{1}{N}\sum_{j=1}^{N} f(\boldsymbol{A})_j (f(\boldsymbol{A})_j - f(\boldsymbol{A}_{\boldsymbol{B}}^{(i)})_j)$	(iv)	$N(k+2)$	N	Saltelli 08	[39],[30]
Jansen 99	$\sum_{j=1}^{N} (f(\boldsymbol{A})_j (f(\boldsymbol{A}_{\boldsymbol{B}}^{(i)})_j)^2$	(v)	$N(k+2)$	N	Saltelli 08	[37]
Azzini 20	$\sum_{j=1}^{N} (f(\boldsymbol{B})_j - f(\boldsymbol{B}_{\boldsymbol{A}}^{(i)})_j)^2 + (f(\boldsymbol{A})_j - f(\boldsymbol{A}_{\boldsymbol{B}}^{(i)})_j)^2$	(vi)	$2N(k+1)$	$2\,N_{Azz}$	Azzini 20	[40]
Denominator: $V(Y)$ =						
Saltelli 08	$\frac{1}{N}\sum_{j=1}^{N} (f(\boldsymbol{A})_j)^2 - (\frac{1}{N}\sum_{j=1}^{N} f(\boldsymbol{A})_j)^2$	(vii)				[4]
Azzini 20	$\sum_{j=1}^{N} ((f(\boldsymbol{A})_j - f(\boldsymbol{B})_j)^2 + (f(\boldsymbol{A}_{\boldsymbol{B}}^{(i)})_j - f(\boldsymbol{B}_{\boldsymbol{A}}^{(i)})_j)^2$	(viii)				[40]

Factor prioritization targets to rank the different input variables among each other. Therefore, the main effect or first-order sensitivity index S_i is used as it relates to the average expected variance reduction for fixing the input variable i [30,35]. Thus, a large first-order index S_i ($S_i = 0…1$) indicates a large average variance reduction by fixing of i. In other words, this index is a measure of the additive effect of i on the model output. The main effect index S_i has the property $\sum S_i \leq 1$. For a model $Y = f(X_1, X_2, \ldots, X_k)$, S_i is calculated according to:

$$S_i = \frac{V_{X_i}(E_{\boldsymbol{X}_{\sim i}}(Y|X_i))}{V(Y)}$$

In contrast, the total effect, or total effect, sensitivity index S_{Ti} represents the average expected (remaining) variance if all input variables but input variable i could be fixed [30]. Hence, it relates to the average expected variance reduction by fixing all the other input variables while still varying input variable i [30]. The total effect sensitivity index is calculated from ($\boldsymbol{X}_{\sim i}$: matrix of all input variables except i):

$$S_{Ti} = \frac{E_{X_{\sim i}}(V_{X_i}(Y|\boldsymbol{X}_{\sim i}))}{V(Y)}$$

The total order index adds up the first-order index and higher order indices, e.g. for a model with three input variables: $S_{T1} = S_1 + S_{12} + S_{13} + S_{123}$. Hence, it is a measure of the additive plus interaction effects of i on the model output. Due to its nature the sum of all total order indices is at least unity, $\sum S_{Ti} \geq 1$. If the interaction between the input variables is negligible, the higher order sensitivity indices approach zero, resulting in $\sum S_i = 1$ and $\sum S_{Ti} = 1$. The model is then additive. The objective of factor fixing is to identify the input variables that have a negligible impact on the uncertainty and, hence, are at least close to non-influential. To identify the according input variables, the total-order index S_{Ti} is used. A total-order index of zero marks an input variable that has no impact on the model output. However, usually a threshold larger than zero is set below which the impact of an input variable is assumed to be negligible. A commonly assumed threshold is $T_{FF} = 0.01$ [33].

Table 1 summarizes the different estimators under investigation. Among the estimators for calculating S_{Ti} the Jansen estimator is the closest to being state of the art ([30] and recently again confirmed in [29,36], where different estimators for calculating S_{Ti} are compared). For the same sample size N, the cost of evaluation is larger for Azzini 20/21 than for the other estimators (almost double for a large number of input variables k). Hence, in order to have a similar cost of evaluation for a fair comparison in the following investigations, the sample size of the Azzini estimators applied is half the sample size of the other estimators: $N_{Azz} = N/2$. To simplify this in the presentation of the results, a pre-factor p is introduced to show this adaption: $p = N = 2\,N_{Azz}$.

2.3. Power-to-Liquid process model

The Power-to-Liquid process investigated in this work consists of an electrolysis section and a hydrogen-to-syncrude section (see Fig. 2). The latter is operated at 8 000 h/a and converts hydrogen to the desired C5 + products (H2tL part). A techno-economic process analysis of the H2tL process is available in [3,41]. These publications also provide a detailed process description and further background information. In contrast to the H2tL part the full load hours of the electrolyzer FLH_{elec} are assumed to be variable between 2 000–8 000 h/a. In the base case, the electrolyzer operates at 8 000 h/a leading to an overall stationary process (no cavern storage necessary). Wholesale electricity prices change throughout the year. The hourly cost profile is derived from SMARD database (= day-ahead market price for the market area Germany and Luxembourg in 2019) [42] and depicted in Fig. 3. Operating the electrolyzer at hours with low electricity prices reduces the electricity cost. This requires a reduction of full load hours of the electrolyzer which increases the equipment cost through oversizing and additional cavern cost (constant hydrogen provision to the H2tL part).

Fig. 2 shows the flowsheet of the investigated Power-to-Liquid process. Hydrogen and oxygen are produced in a proton exchange membrane electrolyzer from water and electricity. The electrolyzer is either on or off depending on the electricity cost at the respective hours of the year. If the full load hours are smaller than 8 000 h/a, hydrogen is stored in a salt cavern to be used during hours when no hydrogen is produced. Oxygen is either directly provided to the oxyfuel burner, stored in a salt cavern for later provision of oxygen to the burner or sold in case of excess oxygen. Carbon dioxide is provided via monoethanolamine

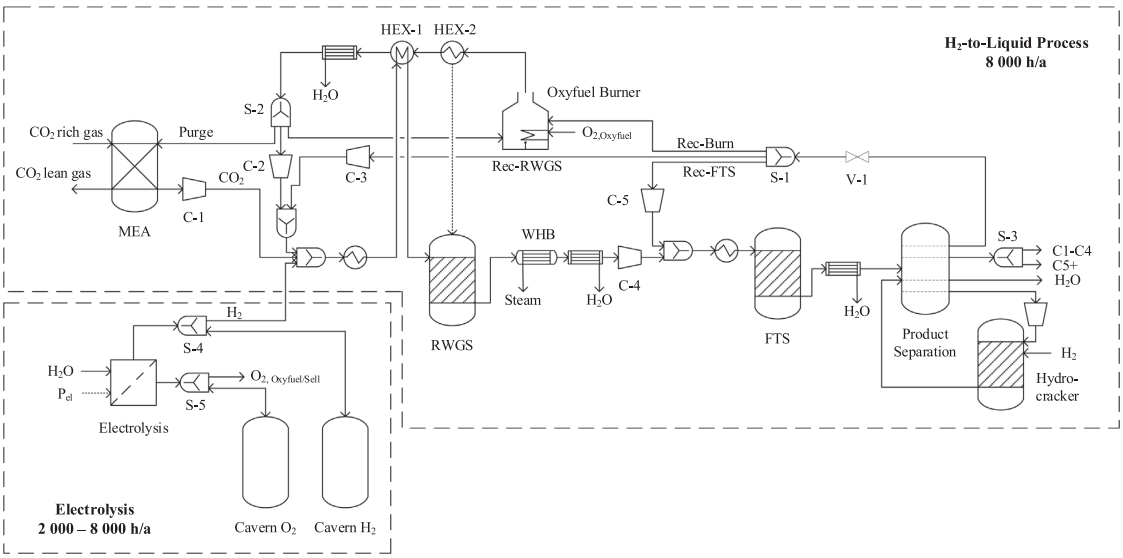

Fig. 2. Flowsheet of the Power-to-Liquid process consisting of a hydrogen supply part and the H2tL part. The hydrogen supply part constitutes an electrolyzer, operated for 2 000–8 000 h/a, using caverns to supply a constant hydrogen feed to the remaining plant. Hydrogen and CO_2-rich gas from the cement plant is processed in/passes through several units: MEA-monoethanolamine absorption, RWGS-reverse water-gas shift, WHB-waste-heat boiler, FTS-Fischer-Tropsch, S-j-splitter, C-j-compressor, V-j-valve.

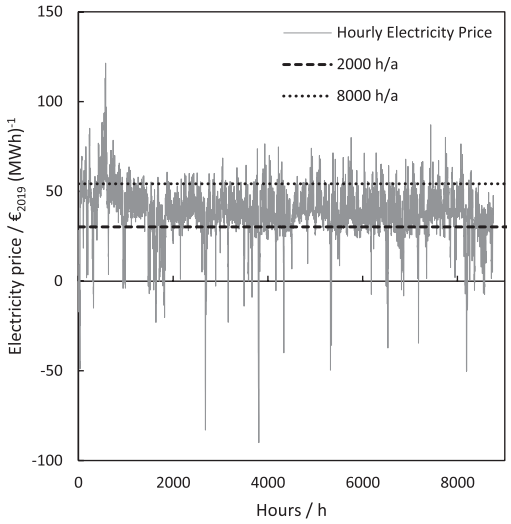

Fig. 3. Fluctuating hourly electricity prices in Germany 2019 derived from SMARD database [42]. The respective maximum electricity prices of the cheapest hours obtained after 8 000 and 2 000 h of operation are: 8 000 h/a → 54.2 €$_{2019}$/MWh and 2 000 h/a → 30.2 €$_{2019}$/MWh. These maximum prices mark the electricity prices at which the electrolyzer is shut down for a given number of full load hours.

scrubbing (MEA) from the CO_2 rich off-gas of an average sized cement plant [41]. The heat demand required for the MEA unit is provided by the exothermic Fischer-Tropsch reactor [41]. Hydrogen and carbon dioxide are converted in the endothermic reverse water-gas shift reaction (RWGS) to produce carbon monoxide (5 bar and 825 °C, see [3,41]). Subsequently, the product gas is cooled in a waste-heat boiler (WHB) to prevent metal-dusting. Water is separated from the product stream, and the remaining syngas continues to the exothermic Fischer-Tropsch (FT) reactor (25 bar, 220 °C) where hydrogen and carbon monoxide react to a broad range of hydrocarbon chain lengths (Co-catalyst, fixed-bed reactor, model based on [43]). The FT product is separated and long chained hydrocarbons (waxes) are fed to a hydrocracker to increase the product output in the desired chain length (C5 +). The light components are recycled to increase the carbon efficiency of the process [3,44]. A partial amount of this recycling gas continues to the FT reactor in order to provide a constant inert gas content in the feed of the FT reactor [41]. A second part continues to the oxyfuel burner to provide the high temperature heat for the RWGS reactor and the remaining gas is recycled to the RWGS reactor [41]. Pinch analysis is carried out to calculate the amount of cooling water required and to assess the amount of medium pressure steam and district heating that may be sold [41].

2.4. Economic methods and assumptions

Table 2 provides the input data to calculate the base case net production cost *NPC*. The *NPC* is calculated from Eqs. (ix)-(xi). The approach is described in detail in [45,46]. The *NPC* is calculated from the annuity *ACC*, direct *OPEX*, indirect *OPEX*, labor cost and the mass flow of the C5 + product $\dot{m}_{C5+}$. Direct *OPEX* are calculated from the specific material cost for raw materials, utilities and by-products. Table 2 depicts the factors and bases used for the calculation of the indirect *OPEX*. The annuity *ACC* is calculated from the fixed capital investment *FCI*, the lifetime of the plant *y* and the interest rate *IR*. The *FCI* is calculated from the equipment cost EC_i and the economic factors $F_{eco,i,j}$.

$$NPC = \frac{ACC + \sum OPEX_{dir} + \sum OPEX_{indir} + C_{labor}}{\dot{m}_{C5+}} \quad \text{(ix)}$$

$$FCI = \sum_{i=1}^{m} EC_i \times \left(1 + \sum_{j=1}^{10} F_{eco,i,j}\right) \times \left(1 + \sum_{j=11}^{12} F_{eco,i,j}\right) \quad \text{(x)}$$

$$ACC = FCI \times \left(IR \times \frac{(1+IR)^y}{(1+IR)^y - 1} + \frac{IR \times y}{9}\right) \quad \text{(xi)}$$

In addition to the base case values to calculate the base case net production cost, Table 2 also summarizes the input data for the UA and GSA. The analyses include uncertainties of the equipment cost, cost for raw materials, utilities and by-products, cost factors for calculating indirect *OPEX* and the *FCI* and a few general assumptions. As a result, 60 input variables are investigated. Each uncertain input variable requires the definition of its probability distribution. In this work, triangular distributions are assumed as the probability functions. This triangular function is defined by a minimum, a maximum value and the highest probability is assumed to be at the base case value (see Table 2).

General plant assumptions: The hydrogen-to-liquid part of the PtL-plant operates 8 000 h/a and is provided with a constant hydrogen feed of 6 t/h. The full load hours of the PEM electrolyzer are assumed to be between 2 000 and 8 000 h/a [61], with 8 000 h/a in the base case. The stack lifetime affects the stack replacement cost. A broad range of stack lifetimes is observed in the literature: 20 000–70 000 h [47], 60 000–100 000 h [24], 40 000 h [62], 50 000–80 000 [53], 20 000–85 000 [57], resulting in an overall range for this uncertainty analysis between 20 000 h [47] and 100 000 h [24]. The base case is assumed to be 40 000 h [48].

Raw materials, utilities and by-products: The specific costs/benefits for water, MEA and the by-products are assumed to be in the range of − 15 % to + 20 % which represents Class 2 in [63]. An important contributor to the *NPC* is the cost for electricity. The specific cost for the steady state provision (8 000 h/a) of electricity is derived from the Eurostat database for large scale industrial consumers (consumption larger than 150 000 MWh/a, data only available for the second semester of 2019) [49]. This database distinguishes between three levels: level 1 – electricity price excluding taxes and levies, level 2 – excluding VAT and other recoverable taxes and levies, level 3 – including all taxes and levies. For the different price levels the electricity cost in 2019 were 34.8 €$_{2019}$/MWh, 76.8 €$_{2019}$/MWh and 111 €$_{2019}$/MWh, respectively. Thus, the range of uncertainty from no to maximum additional charges is 0 €$_{2019}$/MWh to 76.2 €$_{2019}$/MWh while 42 €$_{2019}$/MWh (including concession fee, EEG surcharge, KWK surcharge, offshore surcharge, NEV surcharge and surcharge for switchable loads = level 2) is assumed to be the base case. In contrast to that, the electricity cost for operating the electrolyzer varies with the full load hours of the electrolyzer. Reduced full load hours allow for lower electricity cost as the electrolyzer may be operated at hours with lower electricity prices. The hourly electricity price, without taxes and levies, is derived from the SMARD database and depicted in Fig. 3 [42]. From these values the mean cumulative electricity price is calculated (see Fig. 4). This sets in relation the average price of the cheapest hours to the cumulative hours of consumption. In other words, the mean cumulative electricity price at 8 000 h/a of electrolyzer full load hours is calculated by averaging the electricity prices of the 8 000 cheapest hours in 2019. The resulting average price for 8 000 h of electrolyzer operation is 35.3 €$_{2019}$/MWh. This is slightly higher than the value obtained from the Eurostat database (34.8 €$_{2019}$/MWh). Very few cumulative hours of consumption (smaller than 2 000 h/a) lead to a large reduction and even negative prices. In the range of 2 000–8 000 h the mean price scales almost linearly. Fig. 4 shows the resulting equation that is used to calculate the mean cumulative electricity price (*y*) as a function of the specific full load hours of the electrolyzer FLH_{elec} (*x*).

Equipment cost: It is assumed that the cost for the first set of stacks

Table 2
Base case, minimum and maximum values used to calculate the NPC in the uncertainty and global sensitivity analysis as well as for the deterministic cost analysis [3,24,42,45–56,59,60].

General Plant Assumptions	**Min**	**Max**	**Base**	
Plant full load hours FLH_{H2tL}	-	-	8 000 h	
Hydrogen flow rate	-	-	6 t/h	
Interest rate *IR*	0.04	0.08	0.07	
Plant lifetime *y*	-	-	20 years	
Annual full load hours electrolysis FLH_{elec}	2 000 h	8 000 h	8 000 h	
Stack lifetime SL [24, 47, 48]	20 000 h	100 000 h	40 000 h	
Raw materials and utilities	**Min**	**Max**	**Base**	**€$_{2019}$/**
Electricity for electrolysis, excl. taxes and levies [42]	= f (FLH_{elec})		35.3	MWh
Electricity for H2tL, excl. taxes and levies [49]	-	-	34.8	MWh
Taxes and levies [49]	0	76.2	42	MWh
Cooling water [50]	-15 %	+20 %	0.005	m^3
Fresh water [51]	-15 %	+20 %	2.06	t
MEA (per CO_2 captured) [52]	-15 %	+20 %	2.313	t
Waste water [45]	-15 %	+20 %	2.28	m^3
Stack cost [47, 48, 53]	358	791	450	kW
Stack replacement cost	= f (FLH_{elec}, *SL*)		5.738	MWh
By-Products	**Min**	**Max**	**Base**	**€$_{2019}$/**
District heating [54]	-15 %	+20 %	0.03	kWh
Oxygen [45]	-15 %	+20 %	23.77	t
Medium pressure steam [55]	-15 %	+20 %	19.24	t
C1-C4 product [56]	-15 %	+20 %	1.252	kg
Equipment Cost EC_i[1]	**Min**	**Max**	**Base**	**Unit**
Electrolyzer [24, 48, 57]	= f (FLH_{elec}) -57.2%	+83.3%	388.4	M€$_{2019}$
Cavern [58]	= f (FLH_{elec}) -30 %	+50 %	0	M€$_{2019}$
MEA scrubbing [52]	-30 %	+50 %	7.6	M€$_{2019}$
HEX [46]	-15 %	+20 %	0.96	M€$_{2019}$
Pumps/ Compressors [46]	-15 %	+20 %	9.97	M€$_{2019}$
Hydrocracker [59]	-30 %	+50 %	7.3	M€$_{2019}$
Fischer-Tropsch synthesis [60]	-30 %	+50 %	5.2	M€$_{2019}$
Reverse water-gas shift [3]	-30 %	+50 %	5.74	M€$_{2019}$
Columns [46]	-15 %	+20 %	3.51	M€$_{2019}$
Economic Factors for *FCI* $F_{eco,i,j}$ with *j* = 1…12 [46]	**Min**	**Max**	**Base**	**Basis[2]**
1 Installation factor	0.25	0.55	0.47	*EC*
2 Instrumentation & control	0.08	0.5	0.36	*EC*
3 Piping system	0.1	0.8	0.68	*EC*
4 Electrical systems	0.1	0.4	0.11	*EC*
5 Buildings	0.1	0.7	0.18	*EC*
6 Yard improvements	0.1	0.2	0.1	*EC*
7 Service facilities	0.3	0.8	0.7	*EC*
8 Engineering & supervision	0.32	0.33	0.33	*EC*
9 Construction expenses	0.34	0.41	0.41	*EC*
10 Legal expenses	-	-	0.04	*EC*
11 Contractor's fee	0.015	0.06	0.05	*D* + *I*
12 Contingency	0.05	0.15	0.1	*D* + *I*
Factors for estimating indirect *OPEX* [46]	**Min**	**Max**	**Base**	**Basis[3]**
Operating supervision	0.1	0.2	0.15	*OL*
Maintenance labor	0.01	0.03	0.01	*FCI*
Maintenance material	0.01	0.03	0.01	*FCI*
Operating supplies	0.1	0.2	0.15	*M*
Laboratory charges	0.1	0.2	0.2	*OL*
Insurances and taxes	0.014	0.05	0.02	*FCI*
Plant overhead costs *PO*	0.5	0.7	0.6	*TLC*
Administrative costs	0.15	0.25	0.25	*PO*

[1] *EC* = Equipment Cost, *D* + *I* = Direct (*j* = 1–7) and Indirect (*j* = 8, 9) plant costs.
[2] Economic factors $F_{eco,i,j}$ considered for the different equipment types: All economic factors included for MEA, Pumps, FTS, RWGS, Columns; Including factors for installation, buildings, construction expenses, contractor's fee and contingency for electrolyzer and compressors; No economic factors included (turnkey) for cavern and hydrocracker.
[3] *OL* = Operating Labor calculated from specific labor cost and man-hours [45], *M* = Maintenance Material and Maintenance Labor, *TLC* = Total Labor Costs from operating supervision, *OL* and Maintenance Labor.

is already included in the equipment cost of the electrolyzer while the cost for stack replacement is assigned to the operational expenditures. The cost for stack replacement $C_{Stack\ replacement}$ is calculated based on the stack cost C_{Stack}, the lifetime of the stacks *SL*, the full load hours of the electrolyzer FLH_{elec}, the H2tL plant lifetime *y* and the H2tL full load hours FLH_{H2tL}:

$$C_{Stack\ replacement} = C_{Stack} / (y \bullet FLH_{H2tL}) \bullet (FLH_{elec} \bullet y - SL) / SL.$$

For large stack lifetimes and small electrolyzer full load hours, the lifetime of the stacks may exceed the lifetime of the plant. This results in negative values for the stack replacement cost. In these cases, the cost for stack replacement is set to zero.

For the sake of simplicity, all HEX, pumps & compressors and columns are combined in Table 2, although they are investigated separately in the model. Columns, pumps, compressors and HEX are assumed to have an uncertainty range of − 15 % to + 20 % (Class 2 [63]), whereas the reactors, scrubber and caverns are assumed to be in the range of − 30 % to + 50 % (Class 4 [63]).

The range of electrolyzer equipment cost $EC_{Electrolyzer\ (8000\ h)}$ is obtained from a literature review with − 57.2 % to + 83.3 %. More specific, this range results from the range of the specific equipment cost: 550 €$_{2019}$/kW [24], 1285 €$_{2019}$/kW [48] and 2355 €$_{2019}$/kW [57], which results from the ranges observed in the different studies: 1390–1470 €$_{2017}$/kW [47], 800–2200 €$_{2020}$/kW [57], 1200–1500 €$_{2017}$/kW [48], 700–1400 USD$_{2020}$/kW [53], 614–1704 USD$_{2020}$/kW [24] and

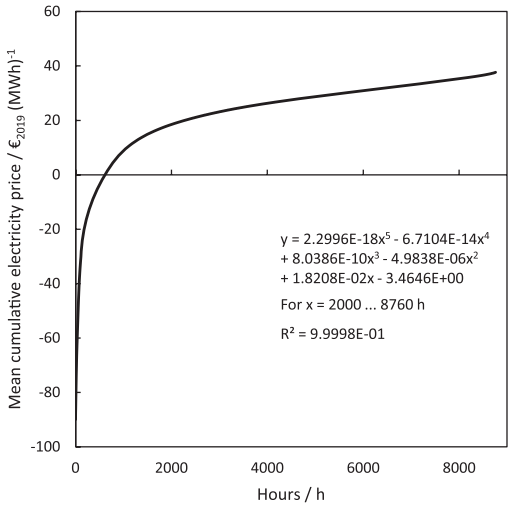

Fig. 4. Mean cumulative electricity price after a respective number of purchased hours. The mean cumulative electricity price is calculated by averaging the cheapest hourly electricity prices provided by SMARD database (see Fig. 3). The fitted 5th order polynomial, mean cumulative electricity price *y* as a function of hours of operation *x*, is applicable for 2 000–8 760 h.

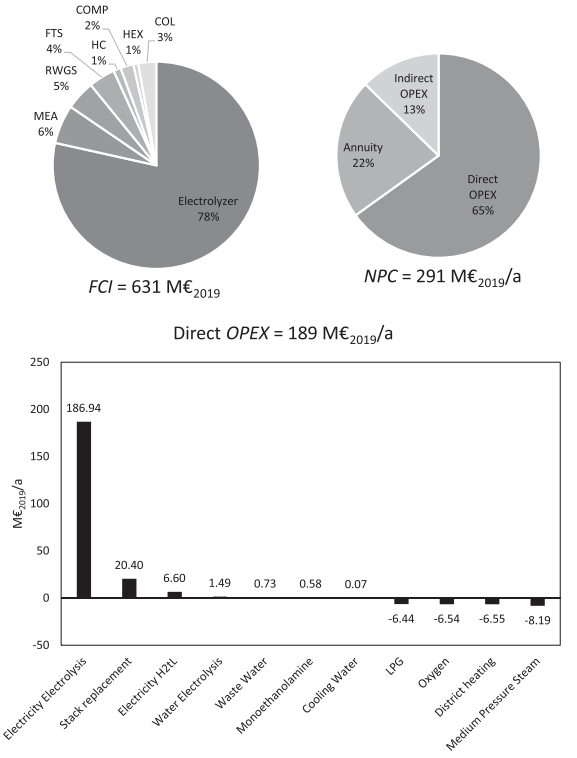

Fig. 5. Fixed capital investment *FCI*, annual net production cost *NPC* and direct *OPEX* for the base case (FLH_{elec}=8 000 h). MEA-Monoethanolamine absorption unit for CO_2 recovery, RWGS-reverse water-gas shift reactor including oxyfuel burner, FTS- Fischer-Tropsch reactor, HC-hydrocracker, COMP-pumps and compressors, HEX-heat exchanger, COL-columns, LPG-liquefied petroleum gas representing the C1-C4 by-product fraction.

1300 €$_{2017}$/kW. Additionally, the electrolyzer cost varies with varying full load hours FLH_{elec}: $EC_{Electrolyzer} = EC_{Electrolyzer\ (8000\ h)} \bullet 8\ 000\ h/a/FLH_{elec}$. In the base case the electrolysis is operated at 8 000 h/a which results in equipment cost of 388.4 M€$_{2019}$ (specific equipment cost of 1285 €$_{2019}$/kW).

In the base case the electrolyzer and the H2tL-part of the plant operate at the same full load hours. Hydrogen and oxygen are continuously fed to the H2tL plant. In contrast, full load hours FLH_{elec} smaller than 8 000 h require hydrogen and oxygen storage. It is assumed that hydrogen and oxygen is stored in salt caverns at a pressure of 30 bar. Boundary electricity prices are calculated above which the electrolyzer is shut down at the respective full load hours. Hence, these boundary prices mark the maximum hourly price that is reached after a respective number of hours of consumption. As an example, Fig. 3 shows the boundary prices for 2 000 and 8 000 h/a electrolyzer full load hours. Comparing the boundary prices with the hourly prices in Fig. 3 shows when the electrolyzer is operated and when it is shut down. If the hourly price is lower than the boundary price, the electrolyzer is producing hydrogen feeding the H2tL plant and the cavern. If the hourly price is higher than the boundary price then the H2tL plant is fed from the hydrogen salt cavern instead. The size of the hydrogen salt cavern is derived from the maximum loading required for constant hydrogen provision. Oxygen is produced along with the hydrogen production. The oxygen cavern size is designed in order to provide enough oxygen in times when the electrolyzer is shut down. Excess oxygen is sold. From the cavern sizes the cost are approximated using the cost function provided by [58]. Two cost functions are fitted for the combined cavern cost for hydrogen and oxygen storage dependent on the full load hours:

$C_{Cavern} = 224.513–0.01595 \bullet FLH_{elec}$ for $FLH_{elec} \leq 7\ 000$ h/a and $C_{Cavern} = 915.013–0.11454 \bullet FLH_{elec}$ for $FLH_{elec} > 7\ 000$ h/a.

See Table 4 for the resulting cavern sizes and costs.

Economic factors for estimating the *FCI* and indirect *OPEX*: The minimum, maximum and base case values are extracted from [46], who also provided the general methodology for the calculation of the *NPC*.

Table 4
Cost calculated for different full load hours of the electrolyzer FLH_{elec}: Electricity cost for electrolysis without taxes and levies, boundary electricity price for sizing of salt caverns, respective storage amount and cavern cost, equipment cost for the electrolyzer and stack replacement cost for different stack lifetimes (20 000, 40 000 and 100 000 h).

FLH_{elec}	Average electricity price	Boundary electricity price	H_2 stored	O_2 stored	H_2 cavern cost	O_2 cavern cost	Electrolyzer cost	Stack replacement (40 000 h)	Stack replacement (20 000 h)	Stack replacement (100 000 h)
h/a	€$_{2019}$/MWh	€$_{2019}$/MWh	t_{2019}/a	t_{2019}/a	M€$_{2019}$	M€$_{2019}$	M€$_{2019}$	M€$_{2019}$/a	M€$_{2019}$/a	M€$_{2019}$/a
2 000	18.45	30.23	4 882	6 500	128	64	1 552	0	7	0
3 000	23.13	34.3	4 487	3 800	125	55	1 035	3	14	0
4 000	26.25	37.01	3 442	1 500	116	42	776	7	20	0
5 000	28.71	39.98	2 830	600	110	33	621	10	27	0
6 000	30.92	43.95	1 962	400	99	29	517	14	34	1
7 000	33.04	48.11	1 315	250	89	26	443	17	41	3
8 000	35.31	54.19	0	0	0	0	388	20	48	4

Table 3
Reference net production cost compared to this work. For a fair comparison the hydrogen-to-syncrude section of the plant is cut off and the *NPC* is recalculated based on the hydrogen prices applied in the reference publication.

	Reference €/kg_{H2}	Reference *NPC* €/kg	This work *NPC* €/kg
Base Case	5.5		3.9
Tremel et al.[27]	3	2–2.3	2.3
Schemme et al.[65]	4.6	2.8	3.4
Zang et al.[64]	4.5	3.5	3.4

3. Results and discussion

The following four subchapters elaborate on the global sensitivity, uncertainty and deterministic cost analysis. The first subchapter focuses on the net production cost breakdown for the base case. Then, different estimators and sampling methods for calculating the global sensitivity indices are compared with respect to their computational effort. In the third subchapter, the impact of the uncertain input variables on the net production cost of the Power-to-Liquid products is evaluated. Subsequently, the most important input variables regarding the uncertainty are analyzed more in depth in a deterministic cost analysis.

3.1. Base case net production cost

The base case net production cost is calculated from the base case input data provided in Table 2. Fig. 5 exhibits the resulting cost contributors to the net production cost *NPC*, fixed capital investment *FCI* and direct *OPEX*. The annual net production cost is 291 $M€_{2019}$/a for a product output of 74.74 kt_{C5+}/a which results in specific net production cost of 3.89 €/kg_{C5+} or 88 €/GJ_{C5+} (based on lower heating value). The main contributor to the *NPC* is the direct *OPEX* (65 %) followed by the annuity (22 %) and indirect *OPEX* (including labor cost). The annuity results from the fixed capital investment. The *FCI* is dominated by the electrolyzer cost (78 %). The annual direct *OPEX* is 189 $M€_{2019}$/a with the electricity cost for electrolysis having the largest share of 187 $M€_{2019}$/a followed by stack replacement cost for the electrolyzer (20.4 $M€_{2019}$/a) and electricity cost for the H2tL part of the plant (6.6 $M€_{2019}$/a). The revenue from the by-products LPG, oxygen, steam and district heating sums up to almost 28 $M€_{2019}$/a. To summarize, the hydrogen production has a large share of the net production cost through firstly electricity cost (64 %) and secondly electrolyzer cost (17 %). Hence, the *NPC* is highly dependent on the electricity cost for electrolyzer operation, which further depends on the full load hours of the electrolyzer (8 000 h/a in the base case, no salt caverns required) and the additional costs for taxes and levies (see chapter 3.2). From these results it is reasonable to argue that it should be the first priority to reduce the electricity price, e.g. by operating the plant at hours with low electricity.

Similar FT based PtL processes have been economically investigated by other researchers. In order to compare the results with literature data the hydrogen-to-syncrude section of the plant is decoupled from the hydrogen provision. Hence, the process is fed with hydrogen purchased for a specified price instead. A comparison of the results with the adapted hydrogen prices used in the different publications yields the results depicted in Table 3. The *NPC*s calculated by Tremel et al. [27] and Zang et al. [64] are in good agreement with this work. Schemme et al. [65] calculate lower *NPC*, which may be related to their higher Power-to-Liquid efficiency.

3.2. Global sensitivity analysis

This subchapter targets to compare two sampling strategies (RND vs. QMC) to calculate the sensitivity indices, to identify the most suitable combination of estimators to calculate the main and total effect sensitivity indices and to conduct factor prioritization as well as factor fixing (assuming the predefined threshold T_{FF}).

The two sampling methods are compared (see Fig. 6A) by comparing the mean changes of $\overline{\varepsilon_{S_{i,j}}}$ and $\overline{\varepsilon_{S_{Ti,j}}}$ for varying sample sizes j. $\overline{\varepsilon_{S_{i,j}}}$ and $\overline{\varepsilon_{S_{Ti,j}}}$ are measures for the stochastic convergence averaged over all input variables i at a respective sample size j. Generally, the Sobol sampling method (lines) outperforms the pseudo-random sampling method (dots) as smaller $\overline{\varepsilon_{S_{i,j}}}$ and $\overline{\varepsilon_{S_{Ti,j}}}$ result for the same sample size j. The progression of the convergence of the main and total effect index for $S_{i,Azzini\ 21}$ and $S_{Ti,Azzini\ 20}$ is identical, whereas it is almost identical for $S_{i,Saltelli\ 10}$ and $S_{Ti,Sobol\ 07}$. In contrast, the total effect index $S_{Ti,Jansen\ 99}$ converges significantly faster than the main effect index $S_{i,Jansen\ 99}$. Overall, the smallest $\overline{\varepsilon_{S_{i,j}/S_{Ti,j}}}$ are obtained for $S_{i,Azzini\ 21}$, $S_{Ti,Azzini\ 20}$ and $S_{Ti,Jansen\ 99}$. Hence, these estimators exhibit the fastest stochastic convergence.

Fig. 6 B/C shows the resulting main and total effect indices at different sample sizes for the different estimators. For the sake of simplicity, only the five input variables with the largest sensitivity indices and their respective 95 % confidence intervals are depicted. For a fair comparison, the sample size N is halved in the Azzini case to provide similar cost of evaluation among the estimators (pre-factors $p = 2\ N_{Azz}$ for Azzini 21/20 and $p = N$ for the other estimators). As expected, increasing sample sizes lead to smaller confidence intervals throughout all estimators. However, the sensitivity index values themselves do not differ largely within the investigated sample sizes.

The horizontal black line in Fig. 6 B/C indicates the threshold for the maximum confidence interval ($T_{CI} = 0.05$) that was preliminary assumed to be necessary in order to reach stochastic convergence [33]. The resulting confidence intervals are compared with this threshold. The sample size where the confidence intervals of all i input variables are below the threshold marks the sample size that is required to reach stochastic convergence. The smaller this sample size, the lower the computational effort as fewer model evaluations are required.

The different estimators for the calculation of the main effect index S_i show significant deviations in their confidence intervals (Fig. 6 B). Within the given sample size ($p = 15\ 000$), Saltelli 10 does not reach the target threshold for large main order indices S_i. Hence, larger computational effort would be required to reach the threshold, especially in order to reduce the confidence intervals for large main effect indices. Similarly, Jansen 99 does not reach the threshold, also requiring larger sample size $p > 15\ 000$. In contrast to Saltelli 10, the confidence intervals are more equally distributed among the different input variables but slightly larger for smaller main effect indices S_i. In contrast to the other estimators Azzini 21 requires comparably low computational effort ($p < 5\ 000$) to reach the target threshold. Consequently, comparing the different estimators to calculate the main effect index S_i shows that Azzini 21 outperforms the other estimators leading to the ranking: Azzini 21 > Jansen 99 > Saltelli 10.

Similar results are obtained when comparing the estimators for calculating the total order indices S_{Ti} (Fig. 6 C). Sobol 07 does not reach the target threshold within the investigated sample size. The threshold is exceeded particularly at large S_{Ti}. In contrast, Jansen 99 and Azzini 20 perform superior, both requiring less than the minimum investigated sample size ($p < 5\ 000$) to reach the target threshold T_{CI}. For both, the confidence intervals increase with increasing S_{Ti}. One might argue that a proper

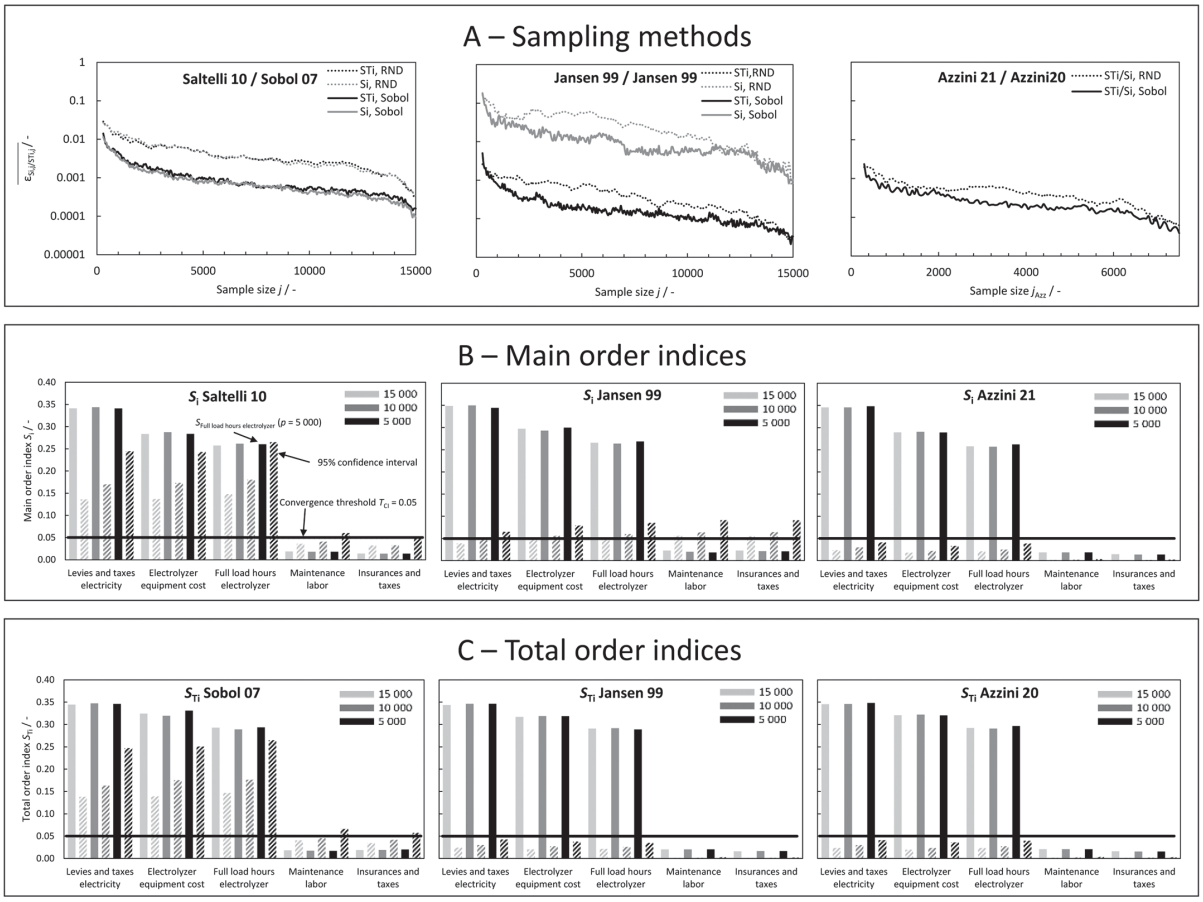

Fig. 6. A: Comparison of sampling methods – random sampling (Excel function RND) and quasi-random sampling (Sobol). For the definition of $\overline{\varepsilon_{S_{ij}}}$ and $\overline{\varepsilon_{S_{Ti,j}}}$ see chapter 2.1 f). B and C: Main and total effect indices (S_i and S_{Ti}) for different pre-factors ($p = 2\,N_{Azz}$ for Azzini 21/20 and $p = N$ for the other estimators (p = 5 000–15 000)) as well as the respective 95 % confidence intervals (the sample size for bootstrapping to calculate confidence intervals equals sampling size for calculating S_i/S_{Ti}, the number of re-evaluations for bootstrapping is 1 000). Sensitivity indices are calculated based on Sobol sampling. The threshold for stochastic convergence is assumed to be $T_{CI} = 0.05$. For the sake of simplicity, the y-axes are only labelled in the left diagram of each row. Thus, the same scale applies for the respective two diagrams in each row.

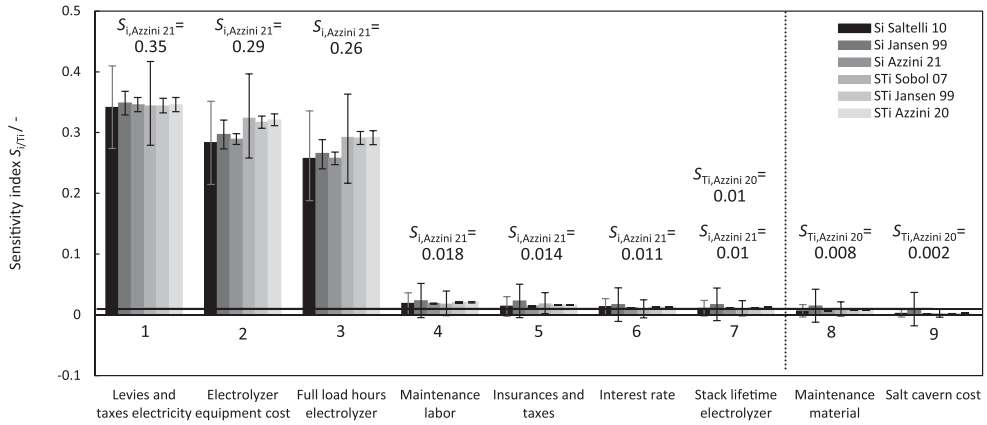

Fig. 7. Main and total order indices for different estimators (p = 15 000, Sobol sampling). Black line indicates the threshold for factor fixing: $T_{FF} = 0.01$. Input variables with $S_{Ti} < 0.01$ are assumed to be fixed without major impact on the uncertainty.

estimation of large S_{Ti} is not necessary as the main objective of S_{Ti} is to fix the unsensitive variables (FF) and hence a good estimation of small S_{Ti} may be more important. However, an accurate approximation of all S_{Ti} also allows to conclude additive/non-additive behavior of the model through adding up all total order indices. Overall, Azzini 20 and Jansen 99 outperform Sobol 07 leading to the following ranking: Azzini 20 ≈ Jansen 99 > > Sobol 07.

Fig. 7 shows the resulting main and total effect indices (largest nine, rest not shown for the sake of simplicity) for the different estimators (assuming $p = 15\,000$ and Sobol sampling) including the corresponding 95 % confidence interval. The obtained main sensitivity indices $S_{i,Azzini\ 21}$ are used for factor prioritization and the total order indices $S_{Ti,\ Azzini\ 20}$ for factor fixing. A preliminary threshold of $T_{FF} = 0.01$ (black line) is assumed for factor fixing (see chapter 2.1). Thus, input variables with $S_{Ti} < 0.01$ are assumed to be close to non-influential and may potentially be fixed in further studies. Seven of the 60 input variables show a total order index larger than $S_{Ti,Azzini\ 20} > 0.01$. However, further investigations in the uncertainty analysis in chapter 3.3 indicate that a threshold of $T_{FF} = 0.002$, resulting in nine sensitive input variables, should be applied. Among the sensitive input variables a factor prioritization is conducted using the Azzini main effect indices $S_{i,Azzini\ 21}$. Three of the input variables lead to substantially larger main effect indices. For these three input variables no overlap of the confidence intervals is observed – hence leading to a clear prioritization: Levies and taxes for electricity (0.35) > Electrolyzer equipment cost EC_{elec} (0.29) > Full load hours electrolyzer FLH_{elec} (0.26). For most input variables the main and the total effect indices do not differ largely, except for EC_{elec} and $FLH_{elec,}$ where the total order index is larger than the main effect index. From this it may be concluded that for EC_{elec} and FLH_{elec} the higher order indices are substantially larger than zero and thus interactions are present. Overall, this results in $\sum S_i = 0.96$ and $\sum S_{Ti} = 1.04$, so an almost, but not purely, additive system (additive model: $\sum S_{Ti} = 1$).

To summarize, quasi-random sampling (QMC) speeds up the stochastic convergence in comparison to pseudo-random sampling (RND). Hence, in order to reduce the computational effort, Sobol sampling is proposed over pseudo-random sampling. Azzini 21 requires the lowest computational effort for the calculation of the main effect index S_i. In order to make the best use of the function evaluations (= model runs), it is beneficial to use the Azzini 21 and Azzini 20 combination for the estimation of both sensitivity indices as no additional function evaluations are required for the calculation of $S_{Ti,Azzini\ 20}$ ($f(\boldsymbol{B})_j$, $f(\boldsymbol{A})_j$, $f(\boldsymbol{A}_{\boldsymbol{B}}^{(i)})_j$ and $f(\boldsymbol{B}_{\boldsymbol{A}}^{(i)})_j$ for the sample size N_{Azz} are already calculated for $S_{i,\ Azzini\ 21}$, compare Table 1). It is also possible to use the Jansen 99 estimator for the calculation of S_{Ti}, but this leads to N_{Azz} additional function evaluations in order to reach the same pre-factor p ($f(\boldsymbol{A})_j$, $f(\boldsymbol{A}_{\boldsymbol{B}}^{(i)})_j$ with $N_{Azz} = N_{Jansen\ 99}/2$ already calculated for $S_{i,\ Azzini\ 21}$). The most important contributors to the uncertainty are: Levies and taxes for electricity (0.35) > Electrolyzer equipment cost EC_{elec} (0.29) > Full load hours electrolyzer FLH_{elec} (0.26). The results from factor fixing are investigated more in detail in the following subchapter.

3.3. Uncertainty analysis

The following subchapter quantifies the uncertainty arising from the uncertainties of all input variables as described in chapter 2.4. Furthermore, the impact of factor fixing different sets of input variables on the cumulative probability distribution is investigated. The outcome is used to examine the suitability of the predefined threshold for factor fixing that is applied in chapter 3.2. In addition, two sampling strategies (MC vs. QMC) are compared in terms of convergence of the standard deviation.

The resulting cumulative probability distribution, taking into consideration all 60 input variables (IV), is shown in Fig. 8 ('Vary all IV'). The resulting 95 % confidence interval considering all 60 input variables is obtained at 3.12–6.64 €$_{2019}$/kg$_{C5+}$ (width of 95 % confidence interval ΔCI = 3.52 €$_{2019}$/kg$_{C5+}$).

In chapter 3.2 factor fixing is conducted with a predefined threshold of $S_{Ti} < 0.01$, leading to a set of seven input variables with a total order index larger than this threshold. Fig. 8 ('Vary IV 1–7′) shows the resulting cumulative probability distribution if all 53 input variables with $S_{Ti} < 0.01$ are fixed to their base case value as shown in Table 2. Ideally, after factor fixing, the variance should be close to identical compared to the variance prior factor fixing [22]. In other words, factor fixing targets to reduce the number of input variables without significant loss in accuracy. However, the resulting confidence interval ΔCI = 3.32 €$_{2019}$/kg$_{C5+}$ is significantly smaller and shifted to smaller values. Hence, the number of input variables taken into consideration for the uncertainty analysis is increased according to their ranking for S_{Ti} as observed in Fig. 7. First maintenance material is added ('Vary IV 1–8′), leading to a larger confidence interval (ΔCI = 3.44 €$_{2019}$/kg$_{C5+}$), but still showing some deviation in comparison to the cumulative curve for varying all IV. Finally, almost identical cumulative probability distributions are observed when further adding the salt cavern cost ('Vary IV 1–9′, ΔCI = 3.55 €$_{2019}$/kg$_{C5+}$). In the present case, it may be concluded that the predefined threshold of 0.01 seems to underestimate the number of input variables required. Iterative identification of the number of relevant input variables lead to less than 1 % deviation between the two confidence intervals (prior and after factor fixing). As a result, the corresponding threshold for factor fixing is reduced to $T_{FF} = 0.002$.

The net production cost for the base case is 3.89 €$_{2019}$/kg$_{C5+}$ (Fig. 8, see also chapter 3.1). With a probability of 20 % the *NPC* is smaller than the base case cost. One input variable considerably contributing to the

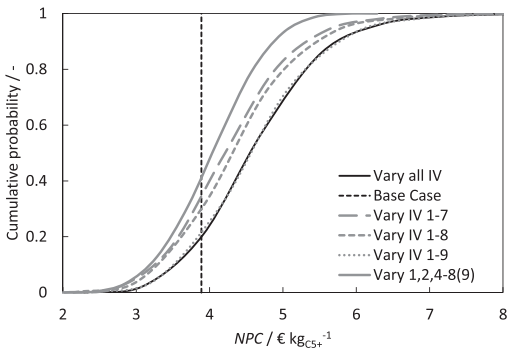

Fig. 8. Cumulative probability distribution of the *NPC* for different input variable cases (Sobol sampling, 15 000 samples). The numbers of the input variables (IV) 1–9 correspond to the ranking from Fig. 7.

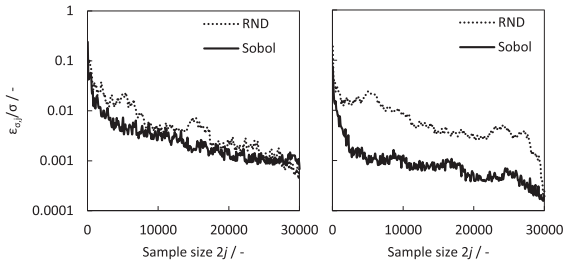

Fig. 9. Normalized deviation of the standard deviation ($\varepsilon_{\sigma,j}$: see chapter 2.1 e), σ: standard deviation of the cumulative probability function at maximum sample size) at varying sample sizes and for different sampling methods: quasi-random sampling 'Sobol' and pseudo-random sampling 'RND', maximum sample size: $2j = 30\,000$. Left: vary all input variables ($k = 60$), right: vary reduced number of input variables after factor fixing and further fixing FLH_{elec} ($k = 7$). Scale of the y-axis applies for both diagrams.

fact that the uncertainty for higher *NPC*s is larger (80 %) than for lower *NPC*s (20 %) is the design variable FLH_{elec}. The full load hours of the electrolyzer is one of the three main contributors to the uncertainty and also a design variable. The deterministic cost analysis in chapter 3.4 leads to the conclusion that the full load hours of the electrolyzer have to be as high as possible in order to reduce the *NPC*. Therefore, FLH_{elec} (IV 3), being a design variable, is fixed to 8 000 h/a. Conclusively, no salt cavern is necessary to store the produced hydrogen and oxygen (IV 9 is fixed). The resulting cumulative probability ('Vary 1,2,4–8(9)') is shown in Fig. 8. The confidence interval $\Delta CI = 2.50$ €$_{2019}$/kg$_{C5+}$ is notably smaller than without fixing the design variable FLH_{elec} and also shifted to smaller *NPC*s. As a result, the uncertainty is reduced substantially. Fixing FLH_{elec} further results in a changed model behavior: $\sum S_i = 1$ and $\sum S_{Ti} = 1$. This means that the remaining model is additive. The probability that the *NPC* is smaller than the base case cost is now at 41 % with the 95 % confidence interval between 2.79 and 5.29 €$_{2019}$/kg$_{C5+}$.

Two sampling methods, quasi-random and pseudo-random, are compared in terms of convergence of the standard deviation (see Fig. 9). Two cases are investigated. In the first case all 60 input variables are varied ('Vary all IV'). In this case the two sampling strategies lead to similar results. The second case fixes most of the input variables leaving only seven for variation ('Vary 1,2,4–8(9)'). In this case, the quasi-random sampling (Sobol method) outperforms the pseudo-random sampling quite notably. Thus, the Sobol method's advantage increases with decreasing number of input variables *k*.

3.4. Deterministic cost analysis

This subchapter investigates the impact of the electrolyzer full load hours (design variable) on the net production cost in a deterministic approach. Moreover, the net production cost dependency on the three main contributors is investigated. As the hydrogen cost is the main contributor to the *NPC* of the syncrude, the hydrogen cost is explored.

Table 4 shows the impact of the electrolyzer full load hours on the electricity price, salt cavern cost, electrolyzer cost and cost for stack replacement. The average electricity prices in this table are derived from the SMARD database for the year 2019 by cumulating and averaging the hours with the lowest electricity prices (see chapter 2.4). Taxes and levies are not included in this electricity price. Naturally, the price increases with increasing full load hours as more of the costly hours contribute to the average price. From 2 000 to 8 000 h/a, the electricity price is almost doubled. As has been mentioned in chapter 2.4, the cavern sizing is conducted based on a boundary price for a respective FLH_{elec}. This price determines when the electrolyzer is shut down. The amount of hydrogen and oxygen that needs to be stored decreases with increasing full load hours until no storage is necessary at 8 000 h/a. Consequently, the respective cavern costs (storage at 30 bar) also decrease with increasing FLH_{elec}. As linear scale-up is assumed for the electrolyzer, and the hydrogen feed to the H2tL plant is kept constant for the different FLH_{elec} cases, it is evident that the electrolyzer costs inversely correlate with the full load hours of the electrolyzer (four times the electrolyzer cost at 2 000 h/a than at 8000 h/a). The amount of initially purchased stacks with the electrolyzer consequently increases with reduced FLH_{elec} resulting in reduced stack replacement cost. Larger stack lifetimes also reduce the stack replacement cost, until the stack replacement cost diminishes at long stack lifetimes and small FLH_{elec}.

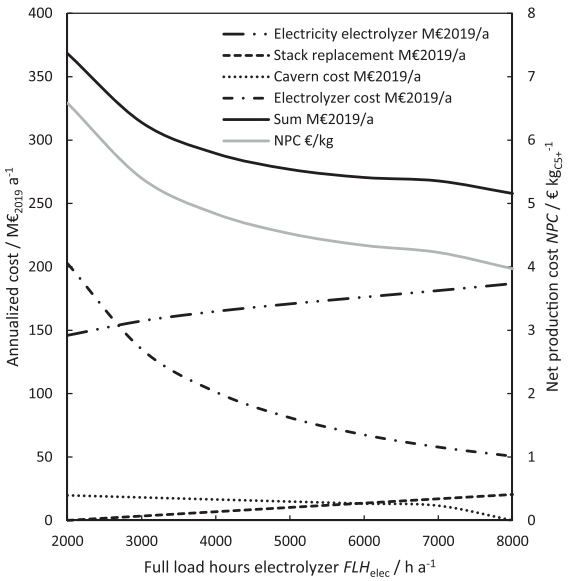

Fig. 10. Annualized cost for electrolyzer electricity, stack replacement, caverns, electrolyzer and the sum thereof as well the specific net production cost *NPC* in dependence of the electrolyzer full load hours FLH_{elec}.

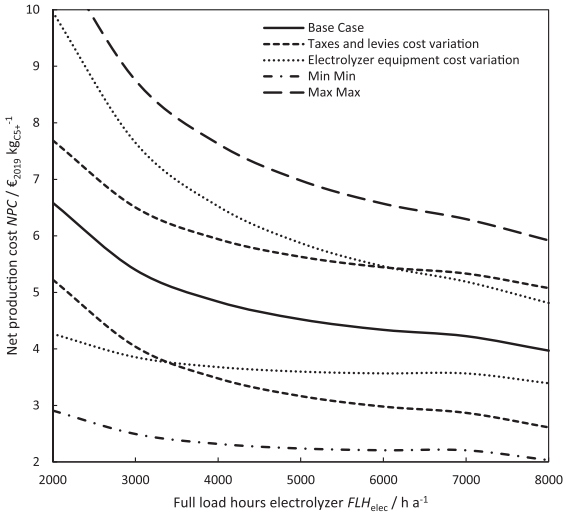

Fig. 11. Influence of the electrolyzer cost, full load hours and taxes and levies on the net production cost. Base case: see also Fig. 10, values from Table 2. Taxes and levies variation: 0–72 €/MWh, electrolyzer equipment cost variation: 550–2355 €/kW, Min Min- minimum values for levies and taxes and minimum value for electrolyzer cost, Max Max- maximum values for levies and taxes and maximum values for electrolyzer cost.

Fig. 10 shows the impact of the electrolyzer full load hours FLH_{elec} on the cost for stack replacement, caverns, electrolyzer, and electrolyzer electricity (non-dependent input variables are fixed to base case values from Table 2). Non-linear behavior is observed for both the annualized costs and the specific net production cost. Reducing the electrolyzer full load hours from the base case operation at 8000 h/a leads to a reduction in electricity cost and stack replacement cost but increases the electrolyzer cost and storage cost in salt caverns. The largest variation is observed for the electrolyzer cost (four times the cost at 2000 h/a than at 8 000 h/a as numbering up is assumed). The electricity cost in the base case is already on a high level but the reduction in electricity cost is not nearly as large as the increase in electrolyzer equipment cost. Consequently, the slight cost reduction of the electricity cost does not outweigh the larger equipment cost for the electrolyzer. This becomes even more evident when adding up the annualized cost for electricity, stack replacement, caverns and electrolyzer, where the sum of the annualized cost increases monotonously with decreasing full load hours. As a result, the net production cost is the lowest for the maximum full

load hours of the electrolyzer FLH_{elec} = 8 000 h/a.

As levies and taxes, full load hours of the electrolyzer and electrolyzer equipment cost are the main contributors to the uncertainty, their impact on the *NPC* is depicted in Fig. 11. The uncertainty in the specific electrolyzer equipment cost results in a large uncertainty of the *NPC* at low FLH_{elec}: *NPC* in the worst case almost 2.5 times larger than the *NPC* in the best case. Especially in the pessimistic electrolyzer cost case (2355 €/kW) the *NPC* is highly dependent on FLH_{elec}. In the optimistic electrolyzer cost case (550 €/kW) the influence of FLH_{elec} almost diminishes (8 000 h/a still result in the lowest *NPC*). The impact of taxes and levies, that add to the electricity cost for electrolysis, on the specific *NPC* is almost constant at different full load hours. The minimum cost calculated for the optimistic electrolyzer and electricity cost cases (no levies and taxes, minimum electrolyzer cost and 8 000 h/a electrolyzer operation) is 2.03 $€_{2019}/kg_{C5+}$.

From the previous results it is evident that the hydrogen production part of the plant has a large impact on the overall economics. Therefore, the hydrogen production process is separated from the H2tL process to calculate the hydrogen net production cost. The resulting hydrogen net production cost in the base case (8 000 h/a, base case values from Table 2) is 5.47 $€_{2019}/kg_{H2}$. The variation of full load hours without additional uncertainties (similar to Fig. 10, base case values from Table 2) results in a hydrogen cost range of 5.47–9.25 $€_{2019}/kg_{H2}$. The minimum hydrogen production cost calculated for the optimistic electrolyzer and electricity cost cases (no levies and taxes, minimum electrolyzer cost and 8 000 h/a electrolyzer operation) is 2.67 $€_{2019}/kg_{H2}$.

4. Conclusions

Global sensitivity (GSA), uncertainty (UA) and deterministic cost analyses are conducted for a Fischer-Tropsch based Power-to-Liquid plant located in Germany for the base year 2019. Generally, the analyses incorporate uncertainty in the cost of equipment, raw materials, utilities, by-products, interest rate and economic factors for calculating capital expenditures and indirect operational expenditures. More specific, one major part of the uncertainty arises from the uncertainty in the electrolyzer's full load operating hours FLH_{elec} which impacts the electricity cost for hydrogen production, the electrolyzer cost, the electrolyzer stack replacement cost and the salt cavern storage cost.

Estimators for global sensitivity analysis: Different estimators, for assessing the variance-based sensitivity indices, are compared in terms of computational effort. As measure of convergence, the confidence intervals of the sensitivity indices have to be lower than a certain threshold (T_{CI} = 0.05) [33]. Comparing the different estimators gives the following rankings (from small to large computational effort) for S_i: Azzini 21 > Jansen 99 > Saltelli 10 and for S_{Ti}: Azzini 20 ≈ Jansen 99 > > Sobol 07. If both main and total effect index are to be determined, the optimum use of the function evaluations (lowest computational effort) results for the combination $_{Si,Azzini\ 21}$ and $S_{Ti,Azzini\ 20}$.

Sampling methods: Sobol sampling outperformed pseudo-random sampling in GSA. The comparison of Sobol sampling and pseudo-random sampling in UA reveals that especially for small numbers of input variables *k* the quasi-random sampling outperforms random sampling with respect to faster convergence of the resulting standard deviations. For large numbers of input variables *k* pseudo-random sampling approaches the results obtained with Sobol sampling. This finding is in good agreement with the observations from [66].

Factor Fixing and Prioritization: At first, a threshold of T_{FF} = 0.01 was assumed for factor fixing. Seven of the 60 input variables result in S_{Ti} > 0.01. The factor fixing threshold applied in GSA is further investigated in the uncertainty analysis. The results indicate that a more conservative threshold (T_{FF} = 0.002) is necessary in order to have a similar cumulative probability distribution before and after factor fixing. As a result, 51 of the 60 input variables may be fixed to reduce the model complexity without significant loss in accuracy. Three input variables have a substantially larger main effect index than the remaining indices. The ranking from factor prioritization is: Levies and taxes for electricity (0.35) > Electrolyzer equipment cost (0.29) > Full load hours electrolyzer (0.26). The electrolyzer full load hours is a design variable and further investigated in a deterministic analysis in order to obtain the optimum FLH_{elec}.

Deterministic Analysis: GSA and UA are subsequently complemented by a deterministic cost analysis with special attention to the three main contributors to the uncertainty. The resulting base case net production cost for syncrude is 3.89 $€_{2019}/kg_{C5+}$ (5.47 $€_{2019}/kg_{H2}$). In the base case, the share of electrolyzer equipment cost is substantially smaller (17 % of *NPC*) than the share of electricity cost (64 % of *NPC*). However, the variation of the electrolyzer full load hours reveals that the reduction in electricity cost, at smaller FLH_{elec}, does not outweigh the cost for additional electrolyzer equipment. Hence, the lowest *NPC* is observed at maximum full load hours of the electrolyzer. The minimum net production cost calculated for the optimistic electrolyzer and electricity cost cases (no levies and taxes, minimum electrolyzer cost and 8 000 h/a electrolyzer operation) is 2.03 $€_{2019}/kg_{C5+}$ (2.67 $€_{2019}/kg_{H2}$). Fixing the full load hours of the electrolyzer, which is a design variable, to its most beneficial value (8 000 h/a), gives a 95 % confidence interval between 2.79 and 5.29 $€_{2019}/kg_{C5+}$. Furthermore, fixing FLH_{elec} reduces the dimensionality from nine uncertain input variables to seven (no salt caverns necessary at maximum FLH_{elec}) and leads to additive model behavior.

Outlook: This work focuses on the uncertainty of relevant economic input data to the *NPC* calculation of the PtL process. Uncertainty in process parameter may also be of interest in future analyses – for example the performance of electrolysis (e.g. efficiency) or Fischer-Tropsch synthesis parameter (e.g. H_2/CO, CO conversion, temperature). However, input variables must be considered carefully as the described approach is only valid for uncorrelated input variables [4]. Beyond that, approaches for non-independent input variables are also available in literature [67,68].

CRediT authorship contribution statement

Sandra Adelung: Conceptualization, Data curation, Formal analysis, Investigation, Methodology, Software, Validation, Visualization, Writing - original draft.

Declaration of Competing Interest

The authors declare that they have no known competing financial interests or personal relationships that could have appeared to influence the work reported in this paper.

Data Availability

Data will be made available on request.

Acknowledgements

This research did not receive any specific grant from funding agencies in the public, commercial, or not-for-profit sectors.

References

[1] R. Sims, Climate Change 2014: Mitigation of Climate Change. Contribution of Working Group III to the Fifth Assessment Report of the Intergovernmental Panel on Climate Change, Cambridge University Press, Cambridge, United Kingdom and New York, NY, USA, 2014, p. 606.
[2] V. Dieterich, et al., Power-to-liquid via synthesis of methanol, DME or Fischer–Tropsch-fuels: a review, Energy Environ. Sci. 13 (10) (2020) 3207–3252.
[3] S. Adelung, R.-U. Dietrich, Impact of the reverse water-gas shift operating conditions on the Power-to-Liquid fuel production cost, Fuel 317 (2022), 123440.
[4] A. Saltelli, et al., Global sensitivity analysis. The Primer, John Wiley & Sons, 2008.

[5] G. Chew, T. Walczyk, A Monte Carlo approach for estimating measurement uncertainty using standard spreadsheet software, Anal. Bioanal. Chem. 402 (7) (2012) 2463–2469.
[6] JCGM, Evaluation of measurement data - Supplement 1 to the "Guide to the Expression of Uncertainty in Measurement" - Propagation of distributions using a Monte Carlo method, in Guide to the Expression of Uncertainty in Measurement. 2008.
[7] A. Saltelli, et al., Sensitivity analysis in practice: a guide to assessing scientific models, Wiley Online Libr. Vol. 1 (2004).
[8] A. Saltelli, et al., Why so many published sensitivity analyses are false: a systematic review of sensitivity analysis practices, Environ. Model. Softw. 114 (2019) 29–39.
[9] I. Dimitriou, H. Goldingay, A.V. Bridgwater, Techno-economic and uncertainty analysis of Biomass to Liquid (BTL) systems for transport fuel production, Renew. Sustain. Energy Rev. 88 (2018) 160–175.
[10] B. Li, et al., Techno-economic and uncertainty analysis of in situ and ex situ fast pyrolysis for biofuel production, Bioresour. Technol. 196 (2015) 49–56.
[11] S. Li, et al., Techno-economic uncertainty analysis of wet waste-to-biocrude via hydrothermal liquefaction, Appl. Energy 283 (2021), 116340.
[12] Y. Jiang, et al., Techno-economic uncertainty quantification of algal-derived biocrude via hydrothermal liquefaction, Algal Res. 39 (2019), 101450.
[13] K. Rajendran, et al., Uncertainty over techno-economic potentials of biogas from municipal solid waste (MSW): A case study on an industrial process, Appl. Energy 125 (2014) 84–92.
[14] K.J. Vicari, et al., Uncertainty in techno-economic estimates of cellulosic ethanol production due to experimental measurement uncertainty, Biotechnol. Biofuels 5 (1) (2012) 1–12.
[15] Z.-C. Tang, et al., Uncertainty analysis and global sensitivity analysis of techno-economic assessments for biodiesel production, Bioresour. Technol. 175 (2015) 502–508.
[16] X. Zhao, T.R. Brown, W.E. Tyner, Stochastic techno-economic evaluation of cellulosic biofuel pathways, Bioresour. Technol. 198 (2015) 755–763.
[17] M. Van der Spek, et al., Uncertainty analysis in the techno-economic assessment of CO_2 capture and storage technologies. Critical review and guidelines for use, Int. J. Greenh. Gas Control 100 (2020), 103113.
[18] A.W. Zimmermann, et al., Techno-economic assessment guidelines for CO_2 utilization, Front. Energy Res. (2020) 5.
[19] B. Koelbl, et al., Uncertainty in the deployment of Carbon Capture and Storage (CCS): A sensitivity analysis to techno-economic parameter uncertainty, Int. J. Greenh. Gas Control 27 (2014) 81–102.
[20] M. Van der Spek, et al., Unravelling uncertainty and variability in early stage techno-economic assessments of carbon capture technologies, Int. J. Greenh. Gas Control 56 (2017) 221–236.
[21] S.H.R. Hosseini, et al., Uncertainty analysis of the impact of increasing levels of gas and electricity network integration and storage on techno-economic-environmental performance, Energy 222 (2021), 119968.
[22] G. Mavromatidis, K. Orehounig, J. Carmeliet, Uncertainty and global sensitivity analysis for the optimal design of distributed energy systems, Appl. Energy 214 (2018) 219–238.
[23] V. Mytilinou, A.J. Kolios, Techno-economic optimisation of offshore wind farms based on life cycle cost analysis on the UK, Renew. Energy 132 (2019) 439–454.
[24] J. Yates, et al., Techno-economic analysis of hydrogen electrolysis from off-grid stand-alone photovoltaics incorporating uncertainty analysis. Cell Rep. Phys. Sci. 1 (10) (2020), 100209.
[25] D. Coppitters, W. De Paepe, F. Contino, Surrogate-assisted robust design optimization and global sensitivity analysis of a directly coupled photovoltaic-electrolyzer system under techno-economic uncertainty, Appl. Energy 248 (2019) 310–320.
[26] D.H. König, et al., Techno-economic study of the storage of fluctuating renewable energy in liquid hydrocarbons, Fuel 159 (2015) 289–297.
[27] A. Tremel, et al., Techno-economic analysis for the synthesis of liquid and gaseous fuels based on hydrogen production via electrolysis, Int. J. Hydrog. Energy 40 (35) (2015) 11457–11464.
[28] S. Schemme, et al., Power-to-fuel as a key to sustainable transport systems–An analysis of diesel fuels produced from CO_2 and renewable electricity, Fuel 205 (2017) 198–221.
[29] A. Puy et al. The battle of total-order sensitivity estimators arXiv Prepr. arXiv 01147 2020.
[30] A. Saltelli, et al., Variance based sensitivity analysis of model output. Design and estimator for the total sensitivity index, Comp. Phys. Commun. 181 (2) (2010) 259–270.
[31] Joe, S. and F. Kuo. File implemented: new-joe-kuo-6.21201 as recommended by the authors. 2010; Available from: ⟨https://web.maths.unsw.edu.au/~fkuo/sobol/⟩.
[32] Han, S.O., Varianzbasierte Sensitivitätsanalyse als Beitrag zur Bewertung der Zuverlässigkeit adaptronischer Struktursysteme. 2011, TU Darmstadt: Darmstadt.
[33] F. Sarrazin, F. Pianosi, T. Wagener, Global sensitivity analysis of environmental models: convergence and validation, Environ. Model. Softw. 79 (2016) 135–152.
[34] G. Archer, A. Saltelli, I.M. Sobol, Sensitivity measures, anova-like Techniques and the use of bootstrap, J. Stat. Comput. Simul. 58 (2) (1997) 99–120.
[35] J. Yang, Convergence and uncertainty analyses in Monte-Carlo based sensitivity analysis, Environ. Model. Softw. 26 (4) (2011) 444–457.
[36] A. Puy, et al., A comprehensive comparison of total-order estimators for global sensitivity analysis, Int. J. Uncertain. Quantif. 12 (2022) 2.
[37] M.J. Jansen, Analysis of variance designs for model output, Comput. Phys. Commun. 117 (1–2) (1999) 35–43.
[38] Azzini, I. and R. Rosati, Sobol' main effect index: An innovative algorithm (IA) using dynamic adaptive variances. Reliability Engineering System Safety, 2021. 213: p. 107647.
[39] I.Y.M. Sobol', Global sensitivity indices for the investigation of nonlinear mathematical models, Mat. Model. 19 (11) (2007) 23–24.
[40] I. Azzini, T. Mara, R. Rosati, 2020. Monte Carlo estimators of first-and total-orders Sobol'indices arXiv Prepr. arXiv 08232.
[41] S. Adelung, S. Maier, R.-U. Dietrich, Impact of the reverse water-gas shift operating conditions on the Power-to-Liquid process efficiency, Sustain. Energy Technol. Assess. 43 (2021), 100897.
[42] Müller, T. SMARD Strommarktdaten. Bundesnetzagentur für Elektrizität, Gas, Telekommunikation, Post und Eisenbahnen 2021 10.11.2021].
[43] D. Vervloet, et al., Tropsch reaction–diffusion in a cobalt catalyst particle: aspects of activity and selectivity for a variable chain growth probability, Catal. Sci. Technol. (2012) 1221–1233.
[44] D.H. König et al.: Simulation and evaluation of a process concept for the generation of synthetic fuel from CO2 and H2, Proceedings of the ICE - Energy , 91, 2015, pp. 833–841.
[45] F.G. Albrecht, et al., A standardized methodology for the techno-economic evaluation of alternative fuels–a case study, Fuel 194 (2017) 511–526.
[46] Peters, M.S., et al., Plant design and economics for chemical engineers. Vol. 5. 2003: McGraw-Hill New York.
[47] Smolinka, T., et al., Industrialisierung der Wasserelektrolyse in Deutschland: Chancen und Herausforderungen für nachhaltigen Wasserstoff für Verkehr, Strom und Wärme, in Studie IndWEDe. 2018.
[48] Chardonnet, C., et al., Study on the early business cases for H2 in energy storage and more broadly power to h2 applications, in A study prepared for the FCH-JU by Tractebel and Hinicio. 2017.
[49] Eurostat. *Electricity prices for non-household consumers - bi-annual data (from 2007 onwards) NRG_PC_205*. [cited 2021.
[50] Bürgerschaft, H., Umweltgebührenordnung (UmwGebO)-Zehnte Verordnung zur Änderung der Umweltgebührenordnung. 2016, Hamburg.
[51] The International Benchmarking Network for Water and Sanitation Utilities (IBNET). 2021 [cited 2021 7.12.2021]; Available from: https://tariffs.ib-net.org/sites.
[52] CO2 capture in the cement industry, in IEA Greenhouse Gas R&D Programme (IEA GHG), 2008/3. 2008.
[53] IRENA, Green Hydrogen Cost Reduction: Scaling up Electrolysers to Meet the 1.5ºC Climate Goal, in International Renewable Energy Agency. 2020: Abu Dhabi.
[54] AGFW, Heizkostenvergleich nach VDI 2067-Musterrechnung. Energieeffizienzverband für Wärme, Kälte und KWK e.V., 2015.
[55] Eurostat, Gas prices for industrial consumers.
[56] Statista, Liquefied petroleum gas (LPG) price in the Netherlands from 2009 to 2020.
[57] O. Schmidt, et al., Future cost and performance of water electrolysis: an expert elicitation study, Int. J. Hydrog. Energy 42 (52) (2017) 30470–30492.
[58] M. Reuß, et al., Seasonal storage and alternative carriers: a flexible hydrogen supply chain model, Appl. Energy 200 (2017) 290–302.
[59] Bechtel, Aspen Process Flowsheet Simulation Model of a Battelle Biomass-Based Gasification, Fischer–Tropsch Liquefaction and Combined-Cycle Power Plant. 1998, US Department of Energy (DOE) Pittsburgh, Pennsylvania.
[60] Prakash, A. and P.G. Bendale, Comparison of slurry versus fixed-bed reactor costs for indirect liquefaction applications. 1991, Viking Systems International, Pittsburgh, PA (United States).
[61] J. Proost, State-of-the art CAPEX data for water electrolysers, and their impact on renewable hydrogen price settings, Int. J. Hydrog. Energy 44 (9) (2019) 4406–4413.
[62] G. Matute, J.M. Yusta, L.C. Correas, Techno-economic modelling of water electrolysers in the range of several MW to provide grid services while generating hydrogen for different applications: a case study in Spain applied to mobility with FCEVs, Int. J. Hydrog. Energy 44 (33) (2019) 17431–17442.
[63] L.R. Dysert et al. Cost Estimate Classification system-as applied in engineering, procurement, and construction for the process industries AACE Int. Recomm. Pract. No. 18R 97 2016 1 30.
[64] G. Zang, et al., Performance and cost analysis of liquid fuel production from H2 and CO_2 based on the Fischer-Tropsch process, J. CO_2 Util. 46 (2021), 101459.
[65] S. Schemme, et al., H2-based synthetic fuels: a techno-economic comparison of alcohol, ether and hydrocarbon production, Int. J. Hydrog. Energy 45 (8) (2020) 5395–5414.

[66] T. Hou, et al., Quasi-Monte Carlo based uncertainty analysis: Sampling efficiency and error estimation in engineering applications, Reliab. Eng. Syst. Saf. 191 (2019), 106549.
[67] K. Zhang, et al., A new framework of variance based global sensitivity analysis for models with correlated inputs, Struct. Saf. 55 (2015) 1–9.
[68] J. Jacques, C. Lavergne, N. Devictor, Sensitivity analysis in presence of model uncertainty and correlated inputs. Reliability Engineering System Safety 91 (10–11) (2006) 1126–1134.

3. Results and Discussion

This chapter is divided into three subchapters in order to address the three research objectives that are introduced in Chapter 1.2 – technical analysis, economic analysis as well as uncertainty and global sensitivity analysis. The technical analysis is conducted in Paper 1 and 2. The economically optimum RWGS operating conditions are investigated in Paper 2, whereas Paper 3 investigates the impact of varying electrolyzer full load hours on the net production cost. Paper 3 also discusses the economic uncertainty and conducts a global sensitivity analysis to identify the main contributors to the uncertainty.

3.1. Technical Analysis (Paper 1 & 2)

The following subchapter summarizes the outcome of the technical process analysis. First, isolated thermodynamic equilibrium calculations are conducted to investigate the influence of RWGS pressure and temperature on the product yields at constant feed conditions. Subsequently, the whole process is analyzed regarding different efficiencies (carbon, hydrogen and Power-to-Liquid efficiency). The subchapter ends with a detailed discussion of the results.

Isolated RWGS equilibrium calculations:

The RWGS reactor's task is to provide CO for the subsequent FT reaction. Figure 6 shows the calculated equilibrium CO_2 conversion and CO selectivity for an exemplary feed of $H_2/CO_2 = 2$ at varying RWGS pressure and temperature. The CO_2 conversion is comparably mildly affected by changes in pressure and temperature. However, the CO selectivity is very sensitive to these changes. The selectivity towards methane increases with decreasing temperature and increasing pressure. Graphite formation becomes of relevance at temperatures below 650 °C. In order to maximize the CO yield, high temperature and low pressure are required from equilibrium perspective. From these isolated equilibrium calculations it can be concluded that the temperature should be at least 600-700 °C in order to establish a favorable once-through CO yield in the RWGS reactor.

The integration of the RWGS unit into the PtL process concept results in varying RWGS feed compositions at varying RWGS operating conditions. More specific, the variation of the RWGS operating conditions yields H_2/CO_2 ratios in the range of 2-3 and a CH_4 content between 1-30 mol % in the feed of the RWGS reactor. Although the isolated equilibrium calculations are only valid for the selected feed composition, the general finding that higher CO yields are established with lower RWGS pressure and higher RWGS temperature are important for the following analysis of the PtL process efficiencies.

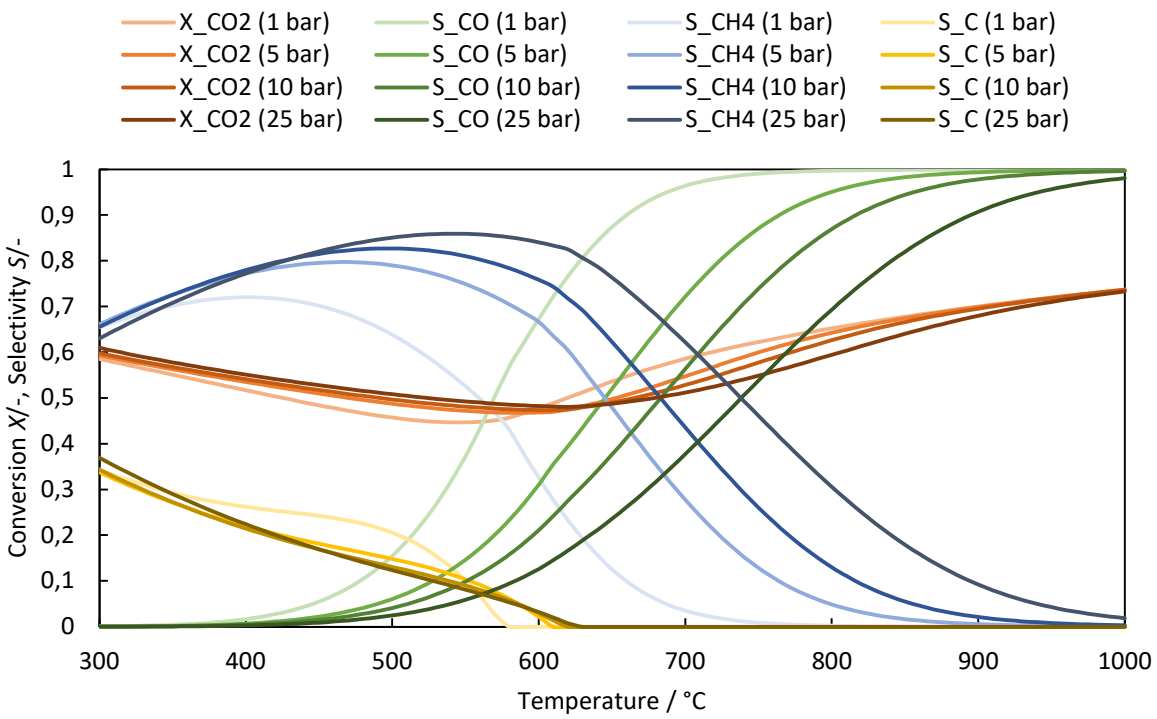

Figure 6: Equilibrium CO_2 conversion *X* and $CO/CH_4/C$ selectivity *S* in Aspen Plus® for a constant feed of $H_2/CO_2 = 2$. Note: Carbon C is considered as graphite.

High energy-dense synthetic hydrocarbons for aviation and shipping are the target product of the investigated process. More specific, the target is to produce a maximum amount of C5+ hydrocarbons from electricity/hydrogen and carbon dioxide. Hence, the material and energetic efficiencies are investigated with respect to the C5+ target product fraction (see Figure 7 for the definitions of the different efficiencies).

Carbon efficiency:

The carbon efficiency sets in relation the carbon in the C5+ product to the carbon in the cement plant's off-gas. Diluted carbon dioxide enters the process as off-gas from the cement plant and is subsequently recovered in a monoethanolamine scrubber with a recovery rate of 90 %. The carbon efficiency is boosted substantially through recycling of the gaseous components and restricted mainly by the recovery of CO_2 from amine scrubbing. It is not affected by the RWGS operating conditions when considering all hydrocarbons as product (Paper 1: $\eta_{C,C2+} = 88$ %). In contrast, the carbon efficiency towards the C5+ fraction is affected through changes in RWGS operating conditions (see Figure 7 right). A higher C5+ carbon efficiency is obtained at lower RWGS temperature and higher RWGS pressure. At these conditions the recycling rate to the RWGS increases, which increases the reforming of C2-C4. This results in a reduction of the C2-C4 fraction in the product output and in return increases the C5+ amount/fraction. The maximum carbon efficiency observed is $\eta_C = 86.8$ %.

Hydrogen efficiency:

The hydrogen efficiency sets in relation the hydrogen incorporated in the C5+ product to the hydrogen obtained from electrolysis. The hydrogen efficiency increases with decreasing RWGS pressure. Pressure dependent optima are observed with respect to the RWGS temperature (see Figure 7 left). The main hydrogen-containing by-product from the process is water. Reducing the RWGS temperature lowers the CO yield, leading to an increase of the inert gas content in the RWGS product gas and thus to an increased recycle rate to the RWGS reactor. An increase in pressure results in the same effect as is observed for a reduction in temperature. In conclusion, low temperature and high pressure are unfavorable for a high hydrogen efficiency (contrarily to what is observed regarding the optimum carbon efficiency!). Additionally, high temperatures induce a higher heat demand also leading to higher water production. The minimum water production, and hence highest hydrogen efficiency (η_H = 24.6 %), is observed at low RWGS pressure and rather low RWGS temperature (700 °C & 1 bar).

Power-to-Liquid efficiency:

Overall, the investigated PtL process is exothermic. Thus, no external heating is required. Consequently, the electricity supply is the main energy input. The Power-to-Liquid efficiency sets in relation the resulting energy in the C5+ product, based on the lower heating value, to the electricity demand for electrolysis, CO_2 recovery and the compression work. In comparison to the results obtained for the hydrogen efficiency, the optimum operating conditions are shifted to slightly higher RWGS pressure and temperature (η_{PtL} = 36.6 % at 800 °C & 5 bar), as the work for compression increases with decreasing RWGS pressure. Similar to the hydrogen efficiency, a plateau is observed where the RWGS operating conditions only have a minor impact on the process performance.

Overall, the PtL process provides a significant amount of heat that can again be used to produce electricity in a steam cycle and thereby increase the energy efficiency by 2 % (Paper 1). However, whether this is economically beneficial remains yet to be proven. Beyond optimization of the RWGS operating conditions, the Power-to-Liquid efficiency may be increased by increasing the electrolyzer efficiency and oxyfuel burner temperature and by reducing FT temperature, H_2/CO ratio as well as through improved heat transfer in the RWGS reactor (Paper 1). Still, changes in these process parameters do not lead to other optimum RWGS operation conditions (Paper 1). Thus, it may be concluded that robust optimum operating conditions are obtained.

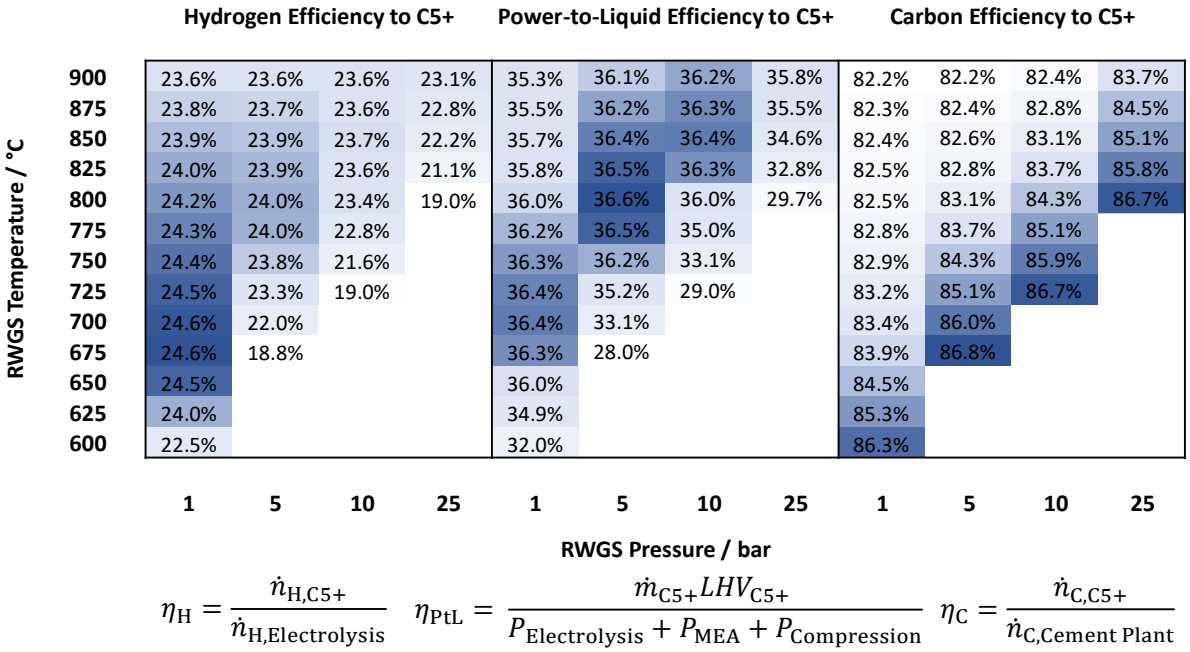

Figure 7: Material efficiencies (hydrogen and carbon) and Power-to-Liquid efficiency of the Power-to-Liquid process at different RWGS operating conditions. The target product is the C5+ fraction.

Discussion:

Table 1 compares the obtained material and energy efficiencies with data available in the literature. The theoretical values are derived in Chapter 1.1. As the electrolyzer efficiency can only be increased through technology improvement, the benchmarking PtL efficiency at a realistic electrolyzer efficiency of 66.7 % is added to the table.

Theoretical efficiencies: The hydrogen efficiency is about 9 % lower in this work in comparison to the theoretical optimum obtained from the stoichiometric consideration. The deviation can be explained by the hydrogen that is lost as water through combustion in the oxy-fuel burner and water that is produced through methanation, in the RWGS and the FT reactor, and C2-C4 production, in the FT reactor. A minor amount of hydrogen also ends up in the by-products C2-C4 (dissolved in the liquid C5+ fraction). About 15 % of the carbon from the cement plant off-gas does not end up in the syncrude. This is mainly due to the scrubber recovery efficiency of 90 %. Losses in C2-C4 and purge gas, that is required in order to avoid accumulation of inert components, further add to the carbon losses. The PtL efficiency is about 20 % lower in comparison to the benchmark PtL efficiency. This results from the reduced hydrogen efficiency as well as from the additional electricity consumption for compression.

Carbon Efficiency: Neither the RWGS nor the FT reactor allows for full conversion. Thus, the carbon efficiency depends mainly on the fact if the gaseous components exiting the FT reactor are again recycled to the RWGS. Conclusively, a once-through operation tends to result in rather low carbon efficiencies (Vázquez *et al.* – pilot plant, Zang *et al.* only recycle CO_2 but not the other gases). If the FT gases are recycled, carbon efficiencies larger than 80 % can be achieved for a scrubber recovery rate

of 90 % (this work, Schemme *et al.* and Vázquez *et al.*-theoretical). Additionally, the carbon efficiency is mildly affected by the amount of gas that needs to be purged in order to avoid accumulation of inert gases.

Table 1: Material and energy efficiencies from this and other works. Brackets indicate that the data was not available and further assumptions had to be made in order to calculate the according values (n.a. – not available).

	η_H	η_C	$\eta_{PtL,LHV}$	$\eta_{Elec.,\ LHV}$
Theoretical maximum (compare Chapter 1.1)	33.3 %	100 %	70 %	100 %
Benchmark efficiency (compare Chapter 1.1)			56 %[d]	66.7 %
Maximum in this work (compare Figure 7)	24.6 %	86.7 %	36.6 %	66.7 %
Base case this work (RWGS @ 800 °C & 5 bar)	24.0 %	83.1 %	36.6 %	66.7 %
Tremel *et al.* [23]	n.a.[h]	n.a.[h]	n.a.[h]	n.a.[h]
Schemme *et al.* [24]	31.3 %	(88 %[a])	50.6 %	70 %
Zang *et al.* [67]	(23.6 %[e])	(41 %[b])	(38.5 %[c])	-
König *et al.* [16]	(27.4 %[e])	(66.3 %[g])	43.3 %	69.7 %
Vázquez *et al.* SOLETAIR - pilot plant [19]	n.a.[h]	38 %	n.a.[h]	-
Vázquez *et al.* - theorectical [19]	32 %	(87.3 %[f])	43.7 %	67 %

[a] The carbon conversion from CO_2 to fuel is 98 %. Assuming the amine scrubber recovery rate from this work of 90 % yields an overall carbon efficiency of 88 %.
[b] The carbon conversion from CO_2 to fuel is 45.5 %. Assuming the amine scrubber recovery rate from this work of 90 % yields an overall carbon efficiency of 41 %.
[c] The model boundaries assume hydrogen as input. Assuming the electrolyzer efficiency from this work of 66.7 % yields a Power-to-Liquid efficiency of 38.5 %.
[d] Benchmarking value for the applied electrolyzer efficiency.
[e] Calculated by applying an approximate hydrogen/carbon ratio of 2 for the product.
[f] The carbon conversion from CO_2 to fuel is 97 %. Assuming the recovery rate from this work of 90 % yields and overall carbon efficiency of 87.3 %.
[g] The carbon conversion from CO_2 to fuel is 73.7 %. Assuming the recovery rate from this work of 90 % yields and overall carbon efficiency of 66.3 %.
[h] n.a – not available: Value could not be calculated with the data available in the respective literature source.

Hydrogen and Power-to-Liquid Efficiency: A high hydrogen efficiency is necessary to achieve a high Power-to-Liquid efficiency as this implies a high conversion from the electrochemically derived hydrogen to the product. Therefore, the approaches with the higher hydrogen efficiencies allow for higher PtL efficiencies. Both, König *et al.* and Schemme *et al*., use the RWGS product gas to preheat the RWGS feed. The RWGS product, however, creates an environment that has a high risk for metal dusting, which is a potential risk for a safe operation of the heat exchanger (see Appendix B). Furthermore, the RWGS product composition may change through reverse reaction in a heat exchanger, which would require experiments in order to assess the actual, cooled product composition in comparison with the equilibrium composition (possible wall catalysis in the heat exchanger, see Appendix A). Therefore, in this work, it is assumed that the product requires rapid cooling in order to allow for a safe operation and to avoid any of these side effects. That means that the product gas

cannot be used to preheat the RWGS feed but is cooled down rapidly in a waste-heat boiler. This, however, leads to a higher energy demand for the RWGS reactor and thus, to a lower hydrogen efficiency as more of the recycling gas needs to be combusted. Additionally, Schemme *et al.* use electrical preheating of the RWGS reactor which also reduces the hydrogen consumption at the expense of more electrical energy input. Still, their operating electrical energy consumptions including electrical RWGS heating seems rather low (1.1 $MJ/kg_{Product}$) in comparison to the electricity consumption obtained in this work (4 $MJ/kg_{Product}$).

Carbon formation: Carbon formation in the reactor may lead to a breakdown of the unit and may therefore narrow down the possible RWGS operating window. Graphite formation is observed in the equilibrium calculations at reduced temperatures (below 675 °C, 750 °C, 800 °C, 850 °C at 1 bar, 5 bar, 10 bar, 25 bar, respectively, see Paper 2 - Figure 8). However, these operating conditions result in a low Power-to-Liquid efficiency (see Paper 2 or Figure 7) and are thus not favorable from an energy perspective. Moreover, experimental investigations show that a suitable catalyst may help to kinetically suppress the carbon formation even at operating conditions where carbon formation is predicted from equilibrium calculations (refer to Annex A for the outcome of the experimental investigations).

Limitations: Strictly, the results in Figure 7 are only valid for this process setup with this specific set of operating conditions for all the process units. However, it is observed that the optimum is robust to changes in other major technical parameters (local sensitivity analysis in Paper 1). Hence, the resulting optima for the material and energy efficiencies are valid for a broad range of operation, for similar/identical technologies.

Conclusions: In this work, it is assumed that CO_2 is provided from a cement plant off-gas. Consequently, only little energy is required to separate the CO_2 from this off-gas. The amount of heat that is required can readily be provided from the exothermic FT synthesis. As a consequence, the carbon efficiency does not seem relevant within this concept as it does not substantially add to the energy consumption. However, if CO_2 was considered to be not available as a point source but would need to be captured from air at a substantial energy demand [68], the focus could shift more to maximizing the carbon efficiency instead of the hydrogen efficiency. The hydrogen efficiency is closely related to the methane forming/reforming and extent of heat demand in the RWGS reactor, which is dependent on the RWGS operating conditions. Low temperature and high pressure both lead to high methane formation and heat demand through higher recycling rates to the RWGS reactor. This results in a higher water production and hence loss in hydrogen as the water is subsequently separated from the process. Also, high temperatures induce a higher heat demand which reduces the hydrogen efficiency. Using electrical heating for the RWGS and recuperation of the RWGS feed with the RWGS product stream has the potential to further increase the hydrogen efficiency especially at high temperatures. However,

a safe operation has to be technically proven. Furthermore, the hydrogen efficiency could potentially be improved through catalyst development that would reduce the production of C1-C4 in the FT reactor.

3.2. Economic Analysis (Paper 2 & 3)

The results from the technical evaluation aid practitioners to understand the material and energy efficiencies. Some of the results from the technical analysis may closely correlate to the economic behavior. This is for example the case when a large share of the cost is allocated to a certain raw material. Consequently, it is important to minimize the required input of this raw material and thus maximize the material efficiency. In contrast, if a process is mainly driven by equipment costs the outcome from the technical optimization will most certainly differ from the economic optimization. In between these scenarios there is often a tradeoff. For example, the conversion in a reactor may be increased through larger reactor sizing (increased residence time). This results in more product but also more cost for the reactor. Thus, depending on the monetary value of the materials, utilities and the equipment, an economic optimization may be driven in order to maximize a certain material efficiency, energetic efficiency or by minimizing equipment cost at the expense of lower efficiencies.

The aim of this thesis is to identify the economically optimum RWGS operating conditions within the Power-to-Liquid process. Therefore, this work implements justified RWGS reactor cost and gives a methodology to calculate the RWGS reactor cost at varying operating conditions (varying pressure, temperature and feed composition). Operating the electrolyzer at hours with low wholesale electricity prices yields lower average electricity prices and thus allows to reduce the cost for electricity. Whether this leads to an overall reduction of the net production cost is part of the economic investigations.

Economic optimum RWGS operating conditions:

A methodology for calculating the RWGS reactor cost depending on the RWGS operating conditions is developed and discussed in Paper 2. The reactor cost is calculated from the cost for furnace, tubes and catalyst. The furnace cost depends on the heat demand of the reactor whereas the tubes are designed depending on the relevant design criterion: heat transfer, pressure drop or kinetic limitation. Moreover, the methodology allows to identify the optimum tube length and tube diameter constellation to minimize the tube cost. All three tube design criteria are observed throughout the investigated RWGS operating conditions: pressure drop at low pressure, heat transfer at high pressure and kinetics at low pressure and temperature. Large tube diameter is superior in the pressure drop limited cases, namely at lower RWGS pressure. The resulting RWGS reactor cost vary in the range of 5-12 M€$_{2019}$. The lowest reactor costs are found at an intermediate temperature range similar to the plateaus observed for the Power-to-Liquid efficiency and at pressures smaller than 10 bar, where smaller wall thickness of the reactor tubes results in lower tube cost.

The net production cost is investigated at varying hydrogen prices in order to assess the impact of the hydrogen cost on the optimum RWGS operating conditions. The chosen hydrogen cost cases are justified in Paper 2. The RWGS reactor cost account for a minor share of the net production cost, e.g. 6 % at 800 °C & 5 bar. Thus, the economically optimum RWGS operating conditions arise rather from changes of the process performance than the RWGS reactor cost. Overall, high hydrogen prices shift the focus on maximizing the hydrogen efficiency, whereas the Power-to-Liquid efficiency is a good indicator when the hydrogen price is intermediate/low (see Figure 8 in comparison with Figure 7). Nevertheless, intermediate pressure and temperature (e.g. 800 °C & 5 bar) allow for low production cost throughout the whole investigated hydrogen cost range.

RWGS Temperature / °C	*NPC* in €$_{2019}$/kg$_{C5+}$ at 2.3 €/kg$_{H2}$				*NPC* in €$_{2019}$/kg$_{C5+}$ at 4.1 €/kg$_{H2}$				*NPC* in €$_{2019}$/kg$_{C5+}$ at 7.6 €/kg$_{H2}$			
	1	5	10	25	1	5	10	25	1	5	10	25
900	1.90	1.82	1.82	1.89	3.16	3.09	3.09	3.18	5.63	5.55	5.56	5.70
875	1.90	1.82	1.81	1.89	3.15	3.08	3.08	3.19	5.60	5.53	5.54	5.74
850	1.89	1.81	1.81	1.91	3.14	3.07	3.07	3.26	5.57	5.50	5.53	5.87
825	1.89	1.81	1.82	1.99	3.13	3.06	3.08	3.41	5.55	5.49	5.54	6.16
800	1.88	1.81	1.84	2.15	3.12	3.06	3.12	3.71	5.53	5.48	5.60	6.76
775	1.88	1.82	1.88		3.11	3.07	3.19		5.50	5.49	5.73	
750	1.88	1.85	1.98		3.10	3.10	3.36		5.49	5.54	6.05	
725	1.88	1.90	2.22		3.10	3.18	3.78		5.47	5.68	6.83	
700	1.88	2.01			3.10	3.37			5.47	6.01		
675	1.90	2.33			3.11	3.91			5.47	6.98		
650	1.93				3.15				5.52			
625	2.00				3.24				5.66			
600	2.19				3.52				6.09			

RWGS Pressure / bar

Figure 8: Syncrude net production cost at varying RWGS operating conditions for three different hydrogen price cases (compare Paper 2).

Impact of the electrolyzer full load hours:

Analyzing the cost breakdown of the net production cost indicates that the electricity cost for hydrogen production is the main contributor to the *NPC* (see Paper 3). Wholesale electricity prices fluctuate throughout the year. Operating the electrolyzer at times with low electricity prices reduces the cost for electricity. However, reducing the full load hours of the electrolyzer also increases the combined electrolyzer equipment and stack replacement cost and adds cost for (cavern) storage. Paper 3 therefore investigates whether a reduction of electrolyzer full load hours leads to a reduction of net production cost. The results in Figure 9 show that the reduction of electricity cost does not outweigh the additional cost, especially for oversizing of the electrolyzer. Consequently, the electrolyzer should be operated at maximum full load hours in order to obtain the minimum net production cost.

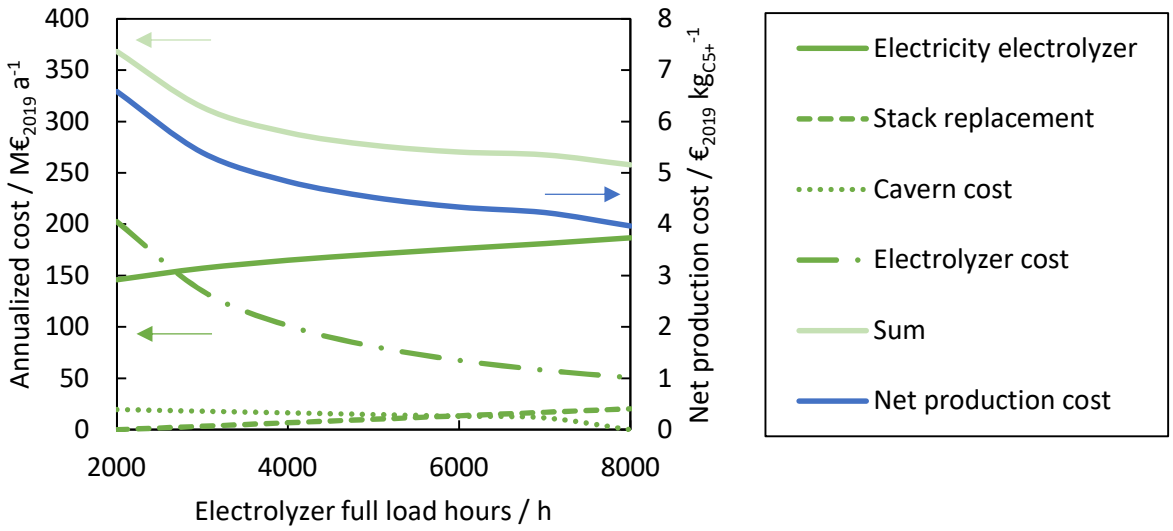

Figure 9: Annualized cost for electrolyzer electricity, caverns, electrolyzer equipment and stack replacement and the sum thereof as well as the net production cost at varying electrolyzer full load hours (reproduced from Paper 3).

Discussion:

Comparison with literature: The resulting net production costs are compared with the results obtained by other researchers for similar processes [23, 24, 67]. Therefore, the RWGS operating conditions are fixed to 800 °C and 5 bar and the net production cost is recalculated based on the hydrogen price applied in the reference publication. The resulting *NPC*s are summarized in Table 2. The *NPC*s calculated by Tremel *et al.* [23] and Zang *et al.* [67] are in good agreement with this work. Schemme *et al.* [24] calculate a lower *NPC*. Their specific hydrogen consumption is 0.48 $kg_{H2}/kg_{Product}$ whereas it is 0.6 $kg_{H2}/kg_{Product}$ in this thesis. Hydrogen makes up for about 90 % of the *NPC*. Applying, for the sake of plausibility, the hydrogen consumption from Schemme *et al.* [24] yields an estimated *NPC* of 2.8 €/kg_{C5+}. Thus, the deviation arises through this difference in hydrogen consumption (refer to Chapter 3.1 regarding the discussion of the difference in hydrogen efficiency).

Carbon efficiency and net production cost: No monetary value is allocated to the off-gas from the cement plant. Thus, the carbon source is assumed to be available at zero cost. Moreover, the carbon dioxide recovery and the carbon efficiency are already at a high value (90 % and > 80 %, respectively) and are thus not severely limiting the amount of possible product. Consequently, the carbon efficiency does not correlate with the *NPC* at varying RWGS operating conditions. Conclusively, the carbon efficiency is not the efficiency to be optimized when targeting low net production cost. This may deviate significantly, when other carbon sources, especially direct air capture, are considered.

Table 2: Recalculated *NPC*s based on the hydrogen prices applied in the reference publication.

	Reference H_2 cost in €/kg_{H2}	Reference *NPC* in €/$kg_{Product}$	This work *NPC* in €/kg_{C5+}
Tremel *et al.* [23]	3	2-2.3	2.3
Schemme *et al.* [24]	4.6	2.8	3.4
Zang *et al.* [67]	4.5	3.5	3.4

Conclusions: In conclusion, the optimization of the hydrogen efficiency is most important when the hydrogen price is high while smaller hydrogen prices shift the focus towards the PtL efficiency optimization as the share of the cost for compression increases. Introducing a variable electrolyzer operation shifts the focus to an equipment cost, more specific electrolyzer cost, related optimization. However, this kind of operation is not found to be economically beneficial. Nevertheless, when targeting robust optima with respect to both, changes in hydrogen price and RWGS operating conditions, it seems more beneficial to maximize the Power-to-Liquid efficiency (800 °C, 5 bar). For example, the minimum *NPC* obtained at high hydrogen prices is found at 700 °C and 1 bar. Small pressure increases may already result in a substantial increase in *NPC*. In contrast this is significantly less relevant at e.g. 800 °C and 5 bar, where the *NPC* is only affected minorly by small changes in RWGS pressure and temperature. Still, the confidence in the obtained results requires further analysis by quantification of the uncertainty (see the following subchapter). In principle, the developed methodology for the reactor cost calculation can be translated to other allothermal tube reactors through an adaption of the reaction kinetics and average heat flux. It is worth to mention that the reactor cost estimation methodology does not claim to represent a detailed reactor design.

3.3. Uncertainty and Global Sensitivity Analysis (Paper 2 & 3)

Uncertainty analysis is conducted to answer the following two questions. Firstly, it is used in order to determine the confidence levels for the economic analysis of the optimum RWGS operating conditions at varying hydrogen prices. Secondly, the uncertainty analysis is conducted to quantify the overall uncertainty of the net production cost including uncertainty in the hydrogen cost provision. The uncertainty analysis is further complimented with a global sensitivity analysis intending to identify the economically unimportant input variables, that can be fixed to any value without impacting the uncertainty of the *NPC* substantially, and furthermore, to allow for a ranking of the important variables in order to prioritize subsequent research efforts.

Question 1: RWGS operating conditions under uncertainty

Equivalently to error bars in experimental works, uncertainty quantification is conducted to aid the interpretation of the economic analysis. The hydrogen cost constitutes a large share of the net

production cost. Therefore, different hydrogen prices are evaluated individually as uncertain hydrogen cost result in an excessive overlapping of the confidence intervals. Still, overlapping of the 95 % confidence intervals is observed over a broad range of RWGS operating conditions (see Figure 10). This yields no clear ranking of the operating conditions within the plateaus. Further investigations would be necessary in order to reduce the uncertainty, and with that reduce the confidence intervals, in order to identify clear optimum RWGS operating conditions for a fixed hydrogen price. Additionally, the results of the uncertainty analysis show an overlapping of the confidence intervals obtained for the respective optimum operating conditions at the specific hydrogen prices. For example, the optimum at high hydrogen price (700 °C & 1 bar) has an overlapping confidence interval with the optimum at low hydrogen price (800 °C & 5 bar) in all three hydrogen price cases. Thus, it is not possible to prioritize either of the two temperature/pressure combinations over another in order to find the best option for variable hydrogen prices. Conclusively, within the given uncertainty, the choice for the optimum RWGS operating conditions is very broad and lies within the plateaus and cannot be fixed to a specific value.

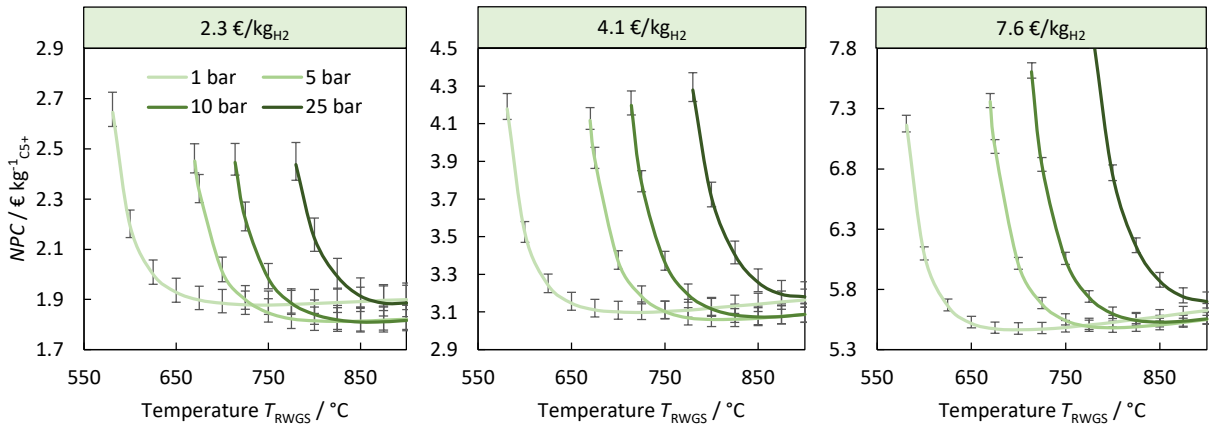

Figure 10: Uncertainty (95 % confidence intervals) of the net production cost at varying hydrogen prices and RWGS operating conditions (reproduced from Paper 2).

Question 2: Uncertainty analysis and allocation

Paper 3 comprises an uncertainty analysis and a variance-based global sensitivity analysis, which allows for allocation of the uncertainty. In contrast to Paper 2 it also incorporates the uncertainty of the hydrogen supply. The preliminary 95 % confidence interval was obtained between 3.12 and 6.64 €$_{2019}$/kg$_{C5+}$ (Figure 11). The first data set consisted of 60 uncertain input variables. It is found that only nine of these 60 input variables contribute relevantly to the output uncertainty. As a result, 51 input variables are fixed to their base case value. This reduces the complexity substantially. One of the main contributors observed was the electrolyzer full load hours. The optimum number of full load hours of the electrolyzer was a design variable as it was uncertain through lack of further analysis and optimization. Thus, the optimum electrolyzer full load hours were obtained through a deterministic

approach (see Chapter 3.2). As a result, the electrolyzer full load hours are fixed to their most beneficial value (maximum full load hours yield the lowest net production cost, eliminating the need for cavern storage). Consequently, the model complexity is further reduced to seven out of 60 input variables. The remaining uncertainty of the seven uncertain input variables is then calculated to be in the range between 2.79 and 5.29 $€_{2019}/kg_{C5+}$ (95 % confidence interval), with the base case at 3.89 $€_{2019}/kg_{C5+}$.

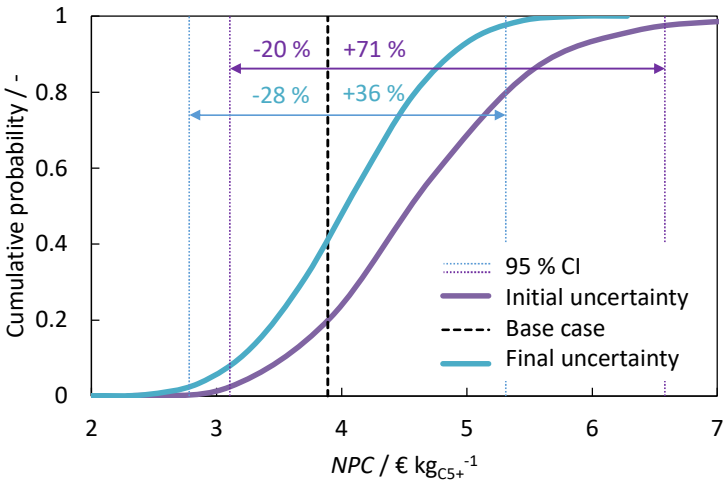

Figure 11: Uncertainty of the net production cost before (Initial uncertainty, 60/9 uncertain variables) and after fixing the electrolyzer full load hours (Final uncertainty, 7 uncertain variables). CI - Confidence Interval.

Estimators for global sensitivity analysis:

Main and total order sensitivity indices are calculated in order to rank influential input variables and to identify non-influential input variables, respectively. Several estimators are available in the literature to calculate these sensitivity indices [64, 65]. For a selection of them it is investigated which estimator requires the lowest computational effort in order to calculate the main and the total order sensitivity index individually as well as simultaneously. The performance indicator for the computational effort is the amount of model evaluations that are required in order to yield a 95 % confidence interval below a predefined threshold for stochastic convergence (see Figure 12). The 95 % confidence intervals are obtained from bootstrapping (resampling from the original sample with replacement). Comparing the different estimators results in the following rankings for the main order index S_i: Azzini 21 [69] > Jansen 99 [70] > Saltelli 10 [64] and for the total order index S_{Ti}: Azzini 20 [71] ≈ Jansen 99 [70] >> Sobol 07 [72],[64]. If both main and total effect index are to be determined simultaneously, the optimum use of the function evaluations results for the combination $S_{i,Azzini\ 21}$ and $S_{Ti,Azzini\ 20}$.

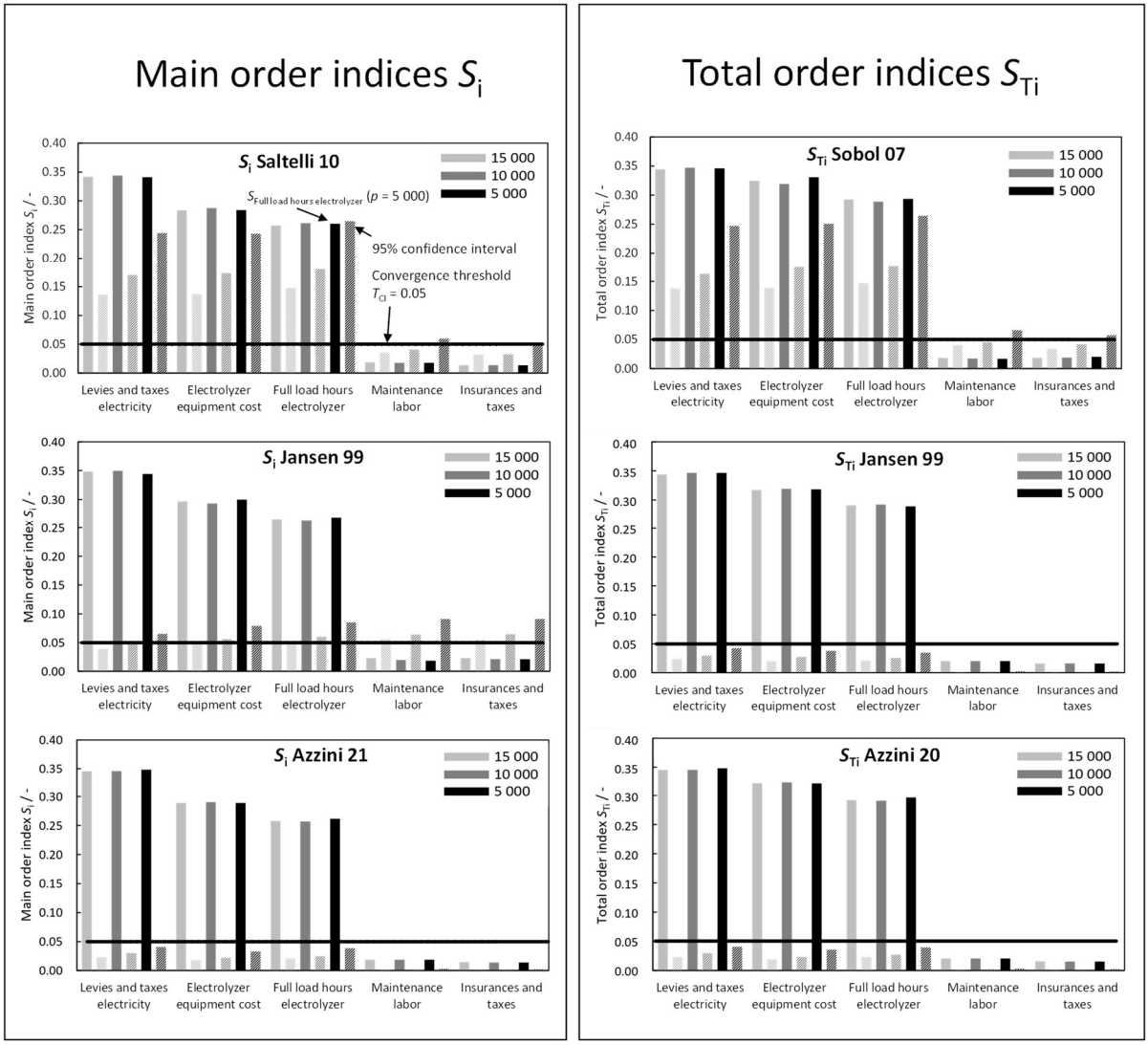

Figure 12: Main and total effect indices at varying sample sizes (model evaluations) as well as the respective 95 % confidence intervals (bootstrapping sample size equals sampling size for calculating S_i/S_{Ti}, number of re-evaluations for bootstrapping is 1 000). The threshold for stochastic convergence is assumed to be T_{CI} = 0.05 (reproduced from Paper 3).

Discussion:

Comparison with literature: Different estimators are also compared in other studies. Puy *et al.* compare eight estimators to calculate the total order index [65, 66]. They state that different conclusions may be drawn for a comparison depending on the sampling method, form and dimensionality of the model function, distribution of the model inputs and the performance measure applied [65]. They rate the Azzini 20 [71] and Jansen 99 [70] estimators over most of the other estimators investigated. Han [73] also compares two estimators for the total order index – resulting in the suggestion of using the Jansen 99 [70] estimator over the Sobol 07 [72], [64] estimator. Similar results are achieved by Saltelli *et al.* [64]. This is in good agreement with the results obtained in this thesis.

Methodology applied for the comparison: Typically, the performance measure used in these comparisons is the mean absolute error. This requires the knowledge of the analytical value of the sensitivity indices. However, the analytical value here was not known as the actual aim was to calculate the sensitivity indices. Instead, in alignment with the work from Han [73], a measure was applied to assess the stochastic convergence of the sensitivity indices through bootstrapping. Based on this method, the different estimators are compared in order to identify which estimator yields the lowest computational effort to reach the target threshold T_{CI}. Interestingly, it is observed that even though some estimators require a very large sample size (e.g. Saltelli 10) to reach the target, they already yield similar sensitivity indices at small sample sizes. However, further analysis would be necessary in order to investigate this observation in more detail.

Conclusions: The results of economic analyses are a priori uncertain [74]. Error bars are used frequently in the assessment of experimental results, whereas this is not very common in economic evaluations. However, making use of confidence intervals obtained from the uncertainty analysis helps the interpretation of the results. Furthermore, it allows comparisons of different approaches under uncertainty. In this thesis, the resulting confidence intervals indicate that no clear ranking of the RWGS operating conditions is possible within the observed plateaus. In order to obtain robust RGWS operating conditions, however, it is further recommended to choose a temperature and pressure combination such that small changes in pressure and temperature do not lead to severe changes in *NPC*. For example, at high hydrogen cost, the minimum is observed at 1 bar and 700 °C. However, an increase in pressure from this optimum would severely increase the *NPC*. Thus, a robust choice would be in the intermediate pressure and temperature range (for example at 800 °C and 5 bar) as changes in RWGS operating conditions and hydrogen cost do not have a large impact on the *NPC*. Although uncertainty analysis may aid practitioners to quantify the uncertainty, the definition of the input probability functions reflecting the uncertainty of the input variables is not trivial. Further research for the assessment of these probability functions and comprehensible guidelines might encourage practitioners and result in a broader application of the methodology. Sensitivity analysis is highly recommended to complement the uncertainty analysis as it helps with the interpretation of the results. It allows to identify main contributors to the uncertainty and therefore can help to prioritize subsequent efforts in order to reduce the uncertainty. Moreover, global sensitivity analysis is not limited to uncertainty analysis. It may also be used in the technical analysis to identify process parameter that have a high impact on the process efficiencies in order to prioritize more detailed (deterministic) analyses as well as to identify process parameter that can be fixed without further investigations.

4. Summary and Outlook

Scope and objectives: A Power-to-Liquid process model was set up in Aspen Plus® for the conversion of carbon dioxide, obtained from amine scrubbing of cement plant off-gas, and hydrogen, from PEM electrolysis, to syncrude for utilization in aviation and shipping. Carbon dioxide and hydrogen react in the reverse water-gas shift (RWGS) reactor to convert the very stable CO_2 molecule to CO, which is then further converted in a Fischer-Tropsch reactor. The process concept is investigated with the objectives of maximizing the efficiency and minimizing the net production cost while taking into consideration the uncertainty in the cost calculations. The obtained confidence intervals are further examined in a global sensitivity analysis to identify the main drivers for the uncertainty.

RWGS operating conditions: The RWGS reactor is a central unit operation within the Power-to-Liquid process concept. Therefore, the impact of variable RWGS operating conditions on the net production cost and efficiencies is investigated. Divergent results are obtained for maximizing the carbon and the hydrogen efficiency. With the economically and energetically inexpensive cement plant off-gas as carbon source, it is more relevant to target a higher hydrogen efficiency from both energetic as well as economic perspective. Hydrogen and Power-to-Liquid efficiency correlate closely as the electricity for the hydrogen production is the main energy consumer. An optimum Power-to-Liquid efficiency is found at 800 °C and 5 bar. This optimum is robust to changes in technical parameters like Fischer-Tropsch operating conditions or electrolyzer efficiency. The Power-to-Liquid efficiency and the economic analysis show pressure dependent temperature plateaus where changes in temperature only have a minor impact. The confidence intervals obtained from the economic uncertainty analysis show overlaps throughout these plateaus. Thus, it is not possible to clearly identify one temperature and pressure combination as the economically optimum choice of operating condition. However, a robust economic optimum is obtained in the intermediate pressure and temperature range, e.g. at 800 °C and 5 bar, where slight changes in operating conditions at variable hydrogen cost have negligible impact on the net production cost. No unwanted graphite formation occurred in the equilibrium calculations in the temperature region of the plateaus. Experiments further indicate that a suitable catalyst may also aid in pushing the carbon formation boundaries to broaden the possible RWGS operating window.

Electrolysis operation: One of the main net production cost contributors is the electricity cost for the electrochemical hydrogen production. Wholesale electricity prices fluctuate during the year. The average electricity price can be reduced, if the electrolyzer is operated at times when wholesale electricity prices are lower. However, the results indicate that the oversizing of the electrolyzer

outweighs the benefit of reduced electricity cost. Conclusively, it is economically more beneficial to operate the electrolyzer at maximum full load hours at the expense of more costly electricity.

Uncertainty and global sensitivity analysis: In order to quantify the uncertainty in the net production cost calculations, DLR's tool for techno-economic process evaluation (TEPET) was extended to conduct a Monte-Carlo based, derivative-free, uncertainty analysis. Furthermore, an intuitive workflow was introduced that allows to simultaneously conduct the uncertainty and global sensitivity analysis. The global sensitivity analysis targets to allocate the uncertainty to the uncertain input variables which consequently enables fixing of unimportant input variables and ranking of important input variables. This is the first work to conduct an uncertainty and global sensitivity analysis of a Fischer-Tropsch based Power-to-Liquid process. The results indicate that seven relevant input variables contribute to an overall uncertainty, 95 % confidence interval, in the range of 2.8-5.3 $€_{2019}/kg_{C5+}$. The most important variables are levies and taxes for electricity as well as electrolyzer equipment cost. Furthermore, different estimators are compared to calculate the main and total order indices in the global sensitivity analysis with respect to the resulting computational effort. If both, main and total order index, are to be determined, the minimum computation effort is achieved for the combination of the Azzini estimators ($S_{i,Azzini\ 21}$ and $S_{Ti,Azzini\ 20}$).

Outlook: Although a few promising experiments were conducted, the final experimental validation of a safe and stable RWGS operation at the obtained optimum RWGS operating conditions remains yet to be proven. Additionally, a more sophisticated RWGS reactor model complementing experimental investigations may aid to identify possible carbon formation potential. Utilizing the RWGS product to preheat the RWGS feed in a heat exchanger has a large potential to increase the Power-to-Liquid efficiency. However, experimental research is necessary to investigate possible metal dusting and reverse reaction in the heat exchanger. From a holistic process analysis point of view, a detailed life cycle assessment would help to quantify and reduce the impact on the environment, e.g. through ecological optimization of the RWGS operating conditions. Additionally, complementing life cycle assessments with uncertainty and global sensitivity analysis could support the interpretation of the results. Moreover, when investigating process models at a rather early stage, with decision variables undecided, global sensitivity analysis may be useful in order to prioritize the subsequent research effort (at the cost of computational effort).

The findings lead the author to the conclusion that the global implementation of the Power-to-Liquid process will depend on the availability of inexpensive sustainable hydrogen, which heavily relies on electricity obtained at low cost and low carbon footprint. Therefore, it will require a united effort from policymakers, industry and society on a worldwide scale to make the process a viable option.

5. References

1. IEA. *Transport License: CC BY 4.0*. 2022; Available from: https://www.iea.org/reports/transport.
2. Sims, R., et al., *Climate Change 2014: Mitigation of Climate Change. Contribution of Working Group III to the Fifth Assessment Report of the Intergovernmental Panel on Climate Change*. 2014, Cambridge University Press: Cambridge, United Kingdom and New York, NY, USA. p. 606.
3. Dieterich, V., et al., *Power-to-liquid via synthesis of methanol, DME or Fischer–Tropsch-fuels: a review.* Energy & Environmental Science, 2020. **13**(10): p. 3207-3252.
4. ASTM, *Standard Specification for Aviation Turbine Fuel Containing Synthesized Hydrocarbons*, in *D7566-20b*. 2020.
5. Fasihi, M., O. Efimova, and C. Breyer, *Techno-economic assessment of CO2 direct air capture plants.* Journal of cleaner production, 2019. **224**: p. 957-980.
6. Barker, D., et al., *IEA Greenhouse Gas R&D Programme (IEA GHG): CO2 capture in the cement industry*, in *Technical Study*. 2008.
7. GCCA, *Concrete Future - The GCCA 2050 Cement and Concrete Industry Roadmap for Net Zero Concrete*. 2021, Global Cement and Concrete Association.
8. Statista. *Total fuel consumption of commercial airlines worldwide between 2005 and 2022*. 2022; Available from: https://www.statista.com/statistics/655057/fuel-consumption-of-airlines-worldwide/.
9. IATA, *Net-Zero Carbon Emissions by 2050*. 2021.
10. Schmidt, P., et al., *Power-to-Liquids as Renewable Fuel Option for Aviation: A Review.* Chemie Ingenieur Technik, 2018. **90**(1-2): p. 127-140.
11. Carmo, M., et al., *A comprehensive review on PEM water electrolysis.* International journal of hydrogen energy, 2013. **38**(12): p. 4901-4934.
12. Becker, W., et al., *Production of Fischer–Tropsch liquid fuels from high temperature solid oxide co-electrolysis units.* 2012. **47**(1): p. 99-115.
13. Cinti, G., et al., *Integration of Solid Oxide Electrolyzer and Fischer-Tropsch: A sustainable pathway for synthetic fuel.* 2016. **162**: p. 308-320.
14. Fasihi, M., D. Bogdanov, and C. Breyer, *Techno-economic assessment of power-to-liquids (PtL) fuels production and global trading based on hybrid PV-wind power plants.* Energy Procedia, 2016. **99**(10th International Renewable Energy Storage Conference, IRES 2016): p. 243-268.
15. Herz, G., E. Reichelt, and M. Jahn, *Techno-economic analysis of a co-electrolysis-based synthesis process for the production of hydrocarbons.* 2018. **215**: p. 309-320.
16. König, D.H., et al., *Simulation and evaluation of a process concept for the generation of synthetic fuel from CO2 and H2.* 2015. **91**: p. 833-841.
17. Schmidt, P., et al., *Power-to-Liquids as Renewable Fuel Option for Aviation: A Review.* 2018. **90**(1-2): p. 127-140.
18. Tremel, A., et al., *Techno-economic analysis for the synthesis of liquid and gaseous fuels based on hydrogen production via electrolysis.* 2015. **40**(35): p. 11457-11464.
19. Vázquez, F.V., et al., *Power-to-X technology using renewable electricity and carbon dioxide from ambient air: SOLETAIR proof-of-concept and improved process concept.* 2018. **28**: p. 235-246.
20. Herz, G., E. Reichelt, and M. Jahn, *Techno-economic analysis of a co-electrolysis-based synthesis process for the production of hydrocarbons.* Applied Energy, 2018. **215**: p. 309-320.
21. Becker, W., et al., *Production of Fischer–Tropsch liquid fuels from high temperature solid oxide co-electrolysis units.* Energy, 2012. **47**(1): p. 99-115.
22. Cinti, G., et al., *Integration of Solid Oxide Electrolyzer and Fischer-Tropsch: A sustainable pathway for synthetic fuel.* Applied Energy, 2016. **162**: p. 308-320.

23. Tremel, A., et al., *Techno-economic analysis for the synthesis of liquid and gaseous fuels based on hydrogen production via electrolysis.* International Journal of Hydrogen Energy, 2015. **40**(35): p. 11457-11464.
24. Schemme, S., et al., *H2-based synthetic fuels: A techno-economic comparison of alcohol, ether and hydrocarbon production.* International journal of hydrogen energy, 2020. **45**(8): p. 5395-5414.
25. Albrecht, F.G., et al., *A standardized methodology for the techno-economic evaluation of alternative fuels–A case study.* Fuel, 2017. **194**: p. 511-526.
26. König, D.H., et al., *Techno-economic study of the storage of fluctuating renewable energy in liquid hydrocarbons.* Fuel, 2015. **159**: p. 289-297.
27. Marchese, M., et al., *CO2 from direct air capture as carbon feedstock for Fischer-Tropsch chemicals and fuels: Energy and economic analysis.* Journal of CO2 Utilization, 2021. **46**: p. 101487.
28. Baliban, R.C., J.A. Elia, and C.A. Floudas, *Toward novel hybrid biomass, coal, and natural gas processes for satisfying current transportation fuel demands, 1: Process alternatives, gasification modeling, process simulation, and economic analysis.* Industrial Engineering Chemistry Research, 2010. **49**(16): p. 7343-7370.
29. Klara, J., et al., *Cost Performance Baseline for Fossil Energy Plants: Bituminous Coal and Natural Gas to Electricity (DOE/NETL-2007/1281)*. 2007.
30. Schwab, E., et al., *Dry reforming and reverse water gas shift: alternatives for syngas production?* Chemie Ingenieur Technik, 2015. **87**(4): p. 347-353.
31. Schemme, S., et al., *Power-to-fuel as a key to sustainable transport systems–An analysis of diesel fuels produced from CO2 and renewable electricity.* Fuel, 2017. **205**: p. 198-221.
32. Dimitriou, I., H. Goldingay, and A.V. Bridgwater, *Techno-economic and uncertainty analysis of Biomass to Liquid (BTL) systems for transport fuel production.* Renewable sustainable energy reviews, 2018. **88**: p. 160-175.
33. Li, B., et al., *Techno-economic and uncertainty analysis of in situ and ex situ fast pyrolysis for biofuel production.* Bioresource technology, 2015. **196**: p. 49-56.
34. Li, S., et al., *Techno-economic uncertainty analysis of wet waste-to-biocrude via hydrothermal liquefaction.* Applied Energy, 2021. **283**: p. 116340.
35. Jiang, Y., et al., *Techno-economic uncertainty quantification of algal-derived biocrude via hydrothermal liquefaction.* Algal Research, 2019. **39**: p. 101450.
36. Rajendran, K., et al., *Uncertainty over techno-economic potentials of biogas from municipal solid waste (MSW): A case study on an industrial process.* Applied Energy, 2014. **125**: p. 84-92.
37. Vicari, K.J., et al., *Uncertainty in techno-economic estimates of cellulosic ethanol production due to experimental measurement uncertainty.* Biotechnology for biofuels, 2012. **5**(1): p. 1-12.
38. Tang, Z.-C., et al., *Uncertainty analysis and global sensitivity analysis of techno-economic assessments for biodiesel production.* Bioresource technology, 2015. **175**: p. 502-508.
39. Zhao, X., T.R. Brown, and W.E. Tyner, *Stochastic techno-economic evaluation of cellulosic biofuel pathways.* Bioresource technology, 2015. **198**: p. 755-763.
40. Van der Spek, M., et al., *Uncertainty analysis in the techno-economic assessment of CO2 capture and storage technologies. Critical review and guidelines for use.* International Journal of Greenhouse Gas Control, 2020. **100**: p. 103113.
41. Zimmermann, A.W., et al., *Techno-economic assessment guidelines for CO2 utilization.* Frontiers in Energy Research, 2020: p. 5.
42. Koelbl, B., et al., *Uncertainty in the deployment of Carbon Capture and Storage (CCS): A sensitivity analysis to techno-economic parameter uncertainty.* International Journal of Greenhouse Gas Control, 2014. **27**: p. 81-102.
43. Van der Spek, M., et al., *Unravelling uncertainty and variability in early stage techno-economic assessments of carbon capture technologies.* International Journal of Greenhouse Gas Control, 2017. **56**: p. 221-236.
44. Hosseini, S.H.R., et al., *Uncertainty analysis of the impact of increasing levels of gas and electricity network integration and storage on Techno-Economic-Environmental performance.* Energy, 2021. **222**: p. 119968.

45. Mavromatidis, G., K. Orehounig, and J. Carmeliet, *Uncertainty and global sensitivity analysis for the optimal design of distributed energy systems.* Applied Energy, 2018. **214**: p. 219-238.
46. Mytilinou, V. and A.J. Kolios, *Techno-economic optimisation of offshore wind farms based on life cycle cost analysis on the UK.* Renewable Energy, 2019. **132**: p. 439-454.
47. Yates, J., et al., *Techno-economic analysis of hydrogen electrolysis from off-grid stand-alone photovoltaics incorporating uncertainty analysis.* Cell Reports Physical Science, 2020. **1**(10): p. 100209.
48. Coppitters, D., W. De Paepe, and F. Contino, *Surrogate-assisted robust design optimization and global sensitivity analysis of a directly coupled photovoltaic-electrolyzer system under techno-economic uncertainty.* Applied Energy, 2019. **248**: p. 310-320.
49. Schmidt, O., et al., *Future cost and performance of water electrolysis: An expert elicitation study.* International Journal of Hydrogen Energy, 2017. **42**(52): p. 30470-30492.
50. Bertuccioli, L., et al., *Development of Water Electrolysis in the European Union*. 2014, Fuel Cells and Hydrogen Joint Undertaking: Lausanne.
51. Roussanaly, S., et al. *Techno-economic analysis of MEA CO2 capture from a cement kiln - impact of steam supply scenario*. in *13th International Conference on Greenhouse Gas Control Technologies, GHGT-13, 14-18*. 2017. Lausanne, Switzerland.
52. Wesenberg, M.H., *Gas heated steam reformer modelling*. 2006, Norwegian University of Science and Technology: Trondheim. p. 11-12.
53. Fratalocchi, L., et al., *Intensifying heat transfer in Fischer-Tropsch tubular reactors through the adoption of conductive packed foams.* Chemical Engineering Journal, 2018. **349**: p. 829-837.
54. Sie, S.T., M.M.G. Senden, and H.M.H. Van Wechem, *Conversion of natural gas to transportation fuels via the shell middle distillate synthesis process (SMDS).* Catalysis Today, 1991. **8**(3): p. 371-394.
55. Vervloet, D., et al., *Fischer–Tropsch reaction–diffusion in a cobalt catalyst particle: aspects of activity and selectivity for a variable chain growth probability.* Catalysis Science & Technology, 2012. **2**(6): p. 1221-1233.
56. Kaiser, P., F. Pöhlmann, and A. Jess, *Intrinsic and Effective Kinetics of Cobalt-Catalyzed Fischer-Tropsch Synthesis in View of a Power-to-Liquid Process Based on Renewable Energy.* Chemical Engineering & Technology, 2014. **37**(6): p. 964-972.
57. Leckel, D. and M. Liwanga-Ehumbu, *Diesel-selective hydrocracking of an iron-based Fischer–Tropsch wax fraction (C15− C45) using a MoO3-modified noble metal catalyst.* Energy & Fuels, 2006. **20**(6): p. 2330-2336.
58. Coonradt, H.L., et al., *Mechanism of hydrocracking. Reactions of Paraffins and Olefins.* Industrial & Engineering Chemistry, 1964. **3**(1): p. 38-45.
59. Adelung, S., *Global sensitivity and uncertainty analysis of a Fischer-Tropsch based Power-to-Liquid process.* Journal of CO2 Utilization, 2022. **65**: p. 102171.
60. Peters, M.S., et al., *Plant design and economics for chemical engineers*. Vol. 5. 2003: McGraw-Hill New York.
61. Adelung, S. and R.-U. Dietrich, *Impact of the reverse water-gas shift operating conditions on the Power-to-Liquid fuel production cost.* Fuel, 2022. **317**: p. 123440.
62. Chew, G. and T. Walczyk, *A Monte Carlo approach for estimating measurement uncertainty using standard spreadsheet software.* Analytical bioanalytical chemistry, 2012. **402**(7): p. 2463-2469.
63. JCGM, *Evaluation of measurement data - Supplement 1 to the "Guide to the Expression of Uncertainty in Measurement" - Propagation of distributions using a Monte Carlo method*, in *Guide to the Expression of Uncertainty in Measurement*. 2008.
64. Saltelli, A., et al., *Variance based sensitivity analysis of model output. Design and estimator for the total sensitivity index.* Computer physics communications, 2010. **181**(2): p. 259-270.
65. Puy, A., et al., *The battle of total-order sensitivity estimators.* arXiv preprint arXiv:.01147, 2020.
66. Puy, A., et al., *A comprehensive comparison of total-order estimators for global sensitivity analysis.* International Journal for Uncertainty Quantification, 2022. **12**(2).
67. Zang, G., et al., *Performance and cost analysis of liquid fuel production from H2 and CO2 based on the Fischer-Tropsch process.* Journal of CO2 Utilization, 2021. **46**: p. 101459.

68. Wang, X. and C. Song, *Carbon capture from flue gas and the atmosphere: A perspective.* Frontiers in Energy Research, 2020. **8**: p. 560849.
69. Azzini, I. and R. Rosati, *Sobol' main effect index: An innovative algorithm (IA) using dynamic adaptive variances.* Reliability Engineering System Safety, 2021. **213**: p. 107647.
70. Jansen, M.J., *Analysis of variance designs for model output.* Computer Physics Communications, 1999. **117**(1-2): p. 35-43.
71. Azzini, I., T. Mara, and R. Rosati, *Monte Carlo estimators of first-and total-orders Sobol'indices.* arXiv preprint arXiv:.08232, 2020.
72. Sobol', I.y.M., *Global sensitivity indices for the investigation of nonlinear mathematical models.* Matematicheskoe modelirovanie (In Russian), 2007. **19**(11): p. 23-24.
73. Han, S.O., *Varianzbasierte Sensitivitätsanalyse als Beitrag zur Bewertung der Zuverlässigkeit adaptronischer Struktursysteme*. 2011, TU Darmstadt: Darmstadt.
74. Dysert, L.R., et al., *Cost Estimate Classification system-as applied in engineering, procurement, and construction for the process industries.* AACE International Recommended Practice No. 18R-97, 2016: p. 1-30.
75. Rostrup-Nielsen, J. and L.J. Christiansen, *Concepts in Syngas Manufacture*. Vol. Catalytic science series. 2011, Denmark: Imperial College Press, London.
76. A. Bode, et al. *Methane Pyrolysis and CO2 Activation -Technologies with Application Options for Hydrogen, Carbon, and Synthesis gas production*. in *Processnet Jahrestagung*. 2016. Aachen: Dechema and VDI-GCV.
77. Thor Wismann, S., K.E. Larsen, and P. Mølgaard Mortensen, *Electrical Reverse Shift: Sustainable CO2 Valorization for Industrial Scale.* Angewandte Chemie, 2022. **134**(8): p. e202109696.
78. Adelung, S., S. Maier, and R.-U. Dietrich. *Energetische Bewertung der Betriebsbedingungen der Synthesegaserzeugung im Power-to-Liquid Verfahren*. in *Processnet Jahrestagung*. 2018. Aachen: Dechema and VDI-GCV.
79. Daza, Y.A. and J.N. Kuhn, *CO 2 conversion by reverse water gas shift catalysis: comparison of catalysts, mechanisms and their consequences for CO 2 conversion to liquid fuels.* RSC advances, 2016. **6**(55): p. 49675-49691.
80. Adelung, S., D. Schnellbögl, and R.-U. Dietrich, *Reaktionskinetik der reversen Wassergas-Shift Reaktion bei Normaldruck zur Übertragung auf die Synthesegasbereitstellung im PtL-Prozess*, in *Processnet Jahrestagung*. 2016: Aachen.
81. Meleloe, K. and D.R. Walwyn, *Success factors for the commercialisation of Gas-to-Liquids technology.* South African Journal of Business Management, 2016. **47**(3): p. 63-72.

Appendix

A RWGS experiments

Carbon formation was experimentally investigated using a monolithic noble metal catalyst (Pt, Pd, Rh on γ-Al_2O_3). Preliminary tests indicated a high activity of the Ni-containing steel tubes. Therefore, experiments were conducted in a tube-in-tube (quartz glass tube inside a high temperature steel tube) configuration to prevent wall catalysis on the steel wall (see Appendix 1). To achieve similar conditions compared to the industrial application, the amount of catalyst was chosen with the aim of reaching equilibrium at the outlet of the reactor. The experiments were conducted over several hours in order to detect any loss of catalytical activity through carbon formation on the active sites. The resulting gas composition is compared with the equilibrium calculations. Furthermore, air is flushed through the system at elevated temperature after each experiment to oxidize any possible carbon depositions at the catalyst.

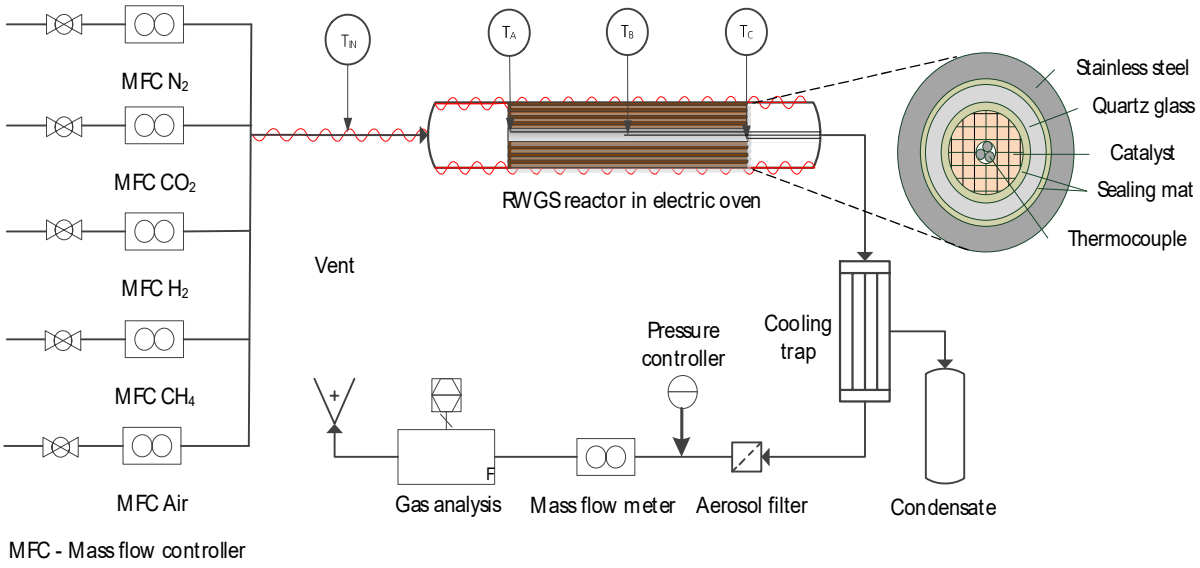

Appendix 1: Experimental RWGS setup to investigate possible carbon formation.

Equilibrium calculations are conducted to identify the risk of carbon formation at varying operating conditions. The results indicated that a higher methane content and lower RWGS temperature increases the risk of carbon formation (see Appendix 2). Experiments are conducted at varying methane contents using a noble metal monolithic catalyst. Even at severe operating conditions (600 °C, H_2/CO_2 = 2 and 31 mol % CH_4), the product composition remained stable during 50 hours on stream (see Appendix 3, left). Furthermore, no CO/CO_2 formation was detected when sending air through the reactor after the experiment. This indicates that no measurable amount of carbon was formed during the experiment. Additionally, the measured product composition is compared to the equilibrium composition calculated in Aspen Plus® (see Appendix 3, right). The calculations are conducted for two scenarios, one considering carbon in the form of graphite as a possible product and one neglecting any carbon formation. A good agreement of the experimental composition with the composition applying carbon suppression is observed. This also indicates that no carbon was formed during the experiment. To summarize, it was demonstrated that it is possible to operate the RWGS unit even at severe

operating conditions (stable 50 hours on stream, no CO/CO_2 detection when treated with oxygen, superior fit of experiment with equilibrium calculations applying suppression of graphite formation). For the sake of completeness, the results obtained at less severe operating conditions (lower methane content) are also shown in Appendix 4.

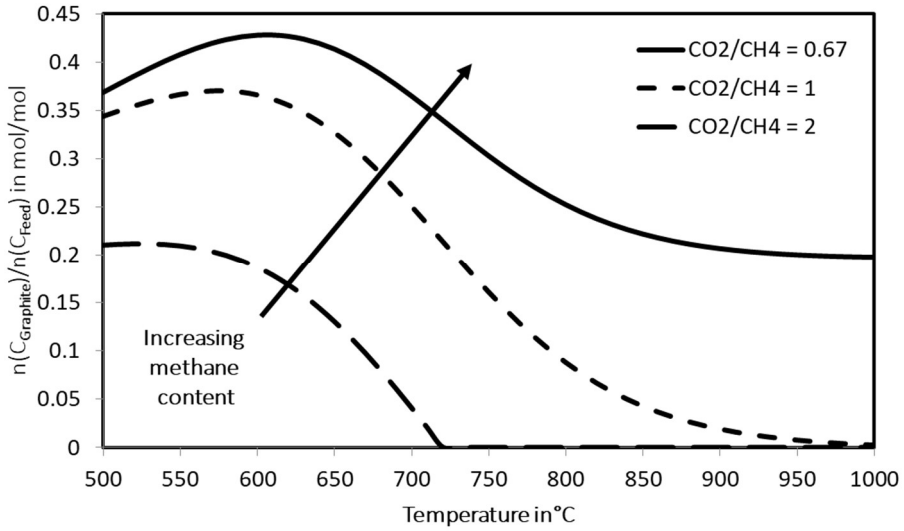

Appendix 2: Graphite (carbon) formation in Aspen Plus® (Gibbs minimization) at 1.5 bar and constant $H_2/CO_2 = 2$.

The most important findings of the experimental investigations and the conclusions derived for the process model can be summarized as follows:

- The reaction is catalyzed substantially through the high temperature stainless steel tube walls: As a result, it is essential to assure inert tube walls in order to conduct kinetic experiments. For the Aspen Plus® model it was decided that the risk of a reverse reaction of the RWGS product in a heat exchange is too high such that the product gas should be cooled down rapidly, for example in a waste-heat boiler. This also reduces the risk for metal dusting.

- Equilibrium was reached at comparably low residence times: For the Aspen Plus® model it was assumed that equilibrium is reached at the outlet of the reactor.

- No indication for carbon formation even at severe operating conditions observed: No limitation of the possible operating window for the technical and economic analysis is predefined. Still, it is worth to mention that the experimental investigations were limited to a rather low pressure of 1.5 bar. Further experiments would be needed to proof the findings at elevated pressure.

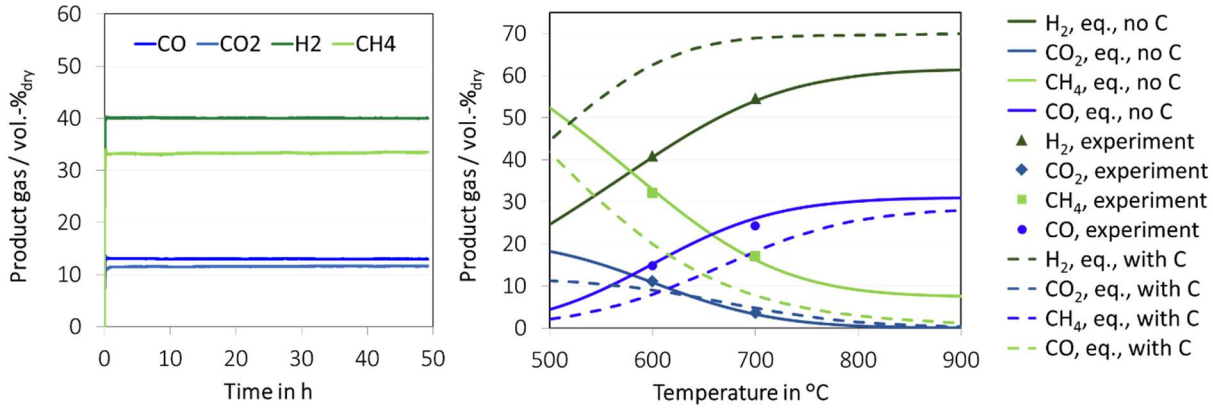

Appendix 3: Left: Transient product composition at p = 1.5 bar, T = 600 °C, H_2/CO_2 = 2, CO_2/CH_4 = 0.67 and the modified retention time τ_{mod} = 41 $kg_{catalyst}$ s $/m^3_{Fluid,norm}$. Right: Comparison of the experimental product composition (experiment) with the results obtained from the equilibrium calculations with (eq., no C) and without (eq., with C) suppression of graphite carbon formation. Operating conditions: p = 1.5 bar, H_2/CO_2 = 2, and CO_2/CH_4 = 0.67.

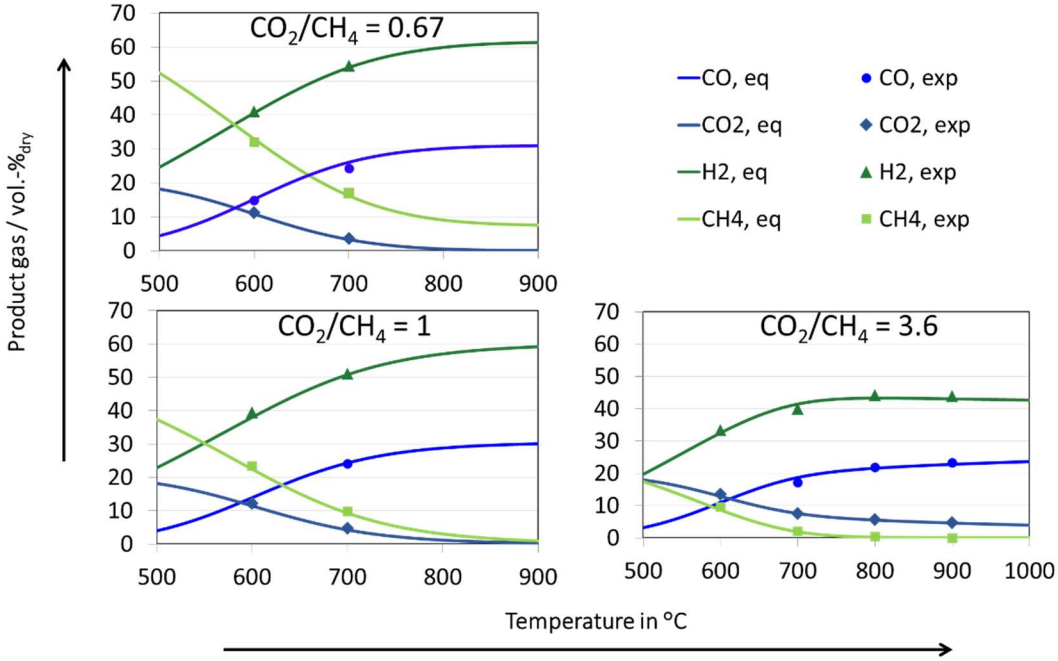

Appendix 4: Experimental product composition (exp) and the results obtained from the equilibrium calculations with suppression of carbon formation (eq) at varying methane content. Operating conditions: p = 1.5 bar, τ_{mod} = 41 $kg_{catalyst}$ s $/m^3_{Fluid,norm}$ and H_2/CO_2 = 2.

B Reverse water-gas shift reactor

Reactor types:

There is no RWGS reactor available at the target scale, yet. However, a lot can be transferred from methane steam reforming as this well-known process has a lot of similarities, e.g. regarding the operating conditions and the reaction network (see Table 6 in Paper 2 for a list of similarities and deviations). The reverse water-gas shift reaction is an endothermic reaction. Different strategies are possible to provide the high-temperature heat for the endothermic reaction:

- Allothermal operation through combustion with air in a tubular fired furnace as applied for several decades in steam methane reforming [75].
- Autothermal operation through combustion with oxygen inside the reactor, e.g. BASF/TKIS [76].
- Electrical heating through induction or ohmic heating, e.g. Haldor Topsoe [77].

A comparison of these three possibilities showed that, for the investigated PtL process concept, the allothermal operation with oxygen combustion and electrical heating are favored over autothermal operation regarding the Power-to-Liquid efficiency [78]. It was found that electrical heating is favorable at electrolyzer efficiencies below 83 $\%_{LHV}$, while the allothermal operation is favored for very high efficiencies [78]. Current electrolyzer efficiencies (≈ 67 $\%_{LHV}$) are well below this electrolyzer efficiency. However, the TRL of the electrically heated RWGS was comparably low at the beginning of this work whereas allothermal operation of methane steam reformers is a well-known and established technique. Moreover, electrical heating leads to more severe operating conditions in the RWGS reactor regarding carbon formation as more short chained hydrocarbons are recycled to the RWGS instead of being combusted in the oxyfuel burner. Therefore, the allothermal type of operation was chosen for the design of this process. Additionally, it is also worth to mention that, the preliminary studies indicate that the technically optimum operating conditions of the electrically heated RWGS do not differ substantially from the optimum operating conditions found in case of allothermal operation [78].

Reaction network and operating conditions:

The relevant reaction network in the RWGS reactor is similar to the reaction network in methane steam reforming (see Appendix 5). The RWGS is an endothermic and equimolar reaction and thus favored at high temperature and not affected by pressure. However, side-reactions such as carbon and methane formation are indeed affected by pressure. The optimum with respect to maximizing the CO yield by minimizing the CH_4 yield is straightforward. Maximum temperature and minimum pressure favor high CO yields.

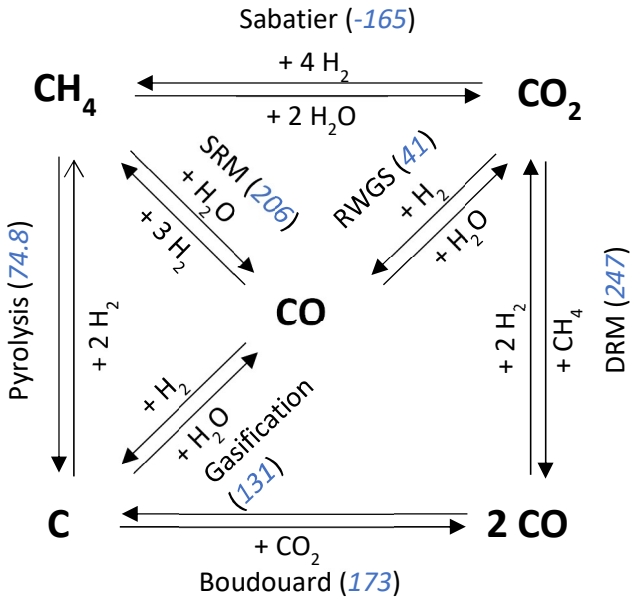

(ΔH_R^0 / (kJ mol^{-1}))

Appendix 5: Reaction network for the RWGS unit including reaction enthalpies. DRM-dry reforming of methane, SRM-steam methane reforming.

Catalytical requirements:

Most researchers target to develop catalysts that obtain the conversion via RWGS reaction while suppressing the methanation reaction in order to have high carbon monoxide yields while having only little methane production. A detailed list of catalysts investigated can be found for example in [79]. In the process design of this thesis, however, the target is to allow for optimum RWGS reactor operation with respect to the overall concept. The task for the RWGS is therein extended from converting only CO_2 to CO to also reforming short chained hydrocarbons (mainly methane and little C2-C4 components formed in the FT reactor). Therefore, the catalyst should also allow for reforming of these short-chained hydrocarbons and must therefore in contrast be active for the methanation reaction. Furthermore, Wismann *et al*. found that RWGS selective catalysts induce a higher carbon formation potential than those that are also active for the methanation reaction [77]. Thus, a methanation active catalyst seems more beneficial from a system level (reforming of methane) and unit level (suppression of carbon formation).

Model:

Experiments using a monolithic, noble metal catalyst indicated that it is possible to reach equilibrium composition at reasonable residence times (τ_{mod} = 41 $kg_{catalyst}$ s/ $m^3_{Fluid,norm}$, see Appendix A and [80]). As a result, the RWGS reactor is modelled as a Gibbs reactor equaling the assumption of thermodynamic equilibrium at the exit of the reactor. Moreover, the experiments showed that it is possible to operate the RWGS at a broad range of methane concentrations without observing carbon

formation (see Appendix A). Thus, the whole pressure and temperature window was investigated. Still, the operating conditions that lead to the formation of carbon in the form of graphite are highlighted in Paper 2.

Metal dusting is a severe kind of high temperature corrosion where graphite enters the steel surface. This results in a break-up of the bulk material to metal powder. The properties of the RWGS product stream lead to an environment that is prone for material problems regarding metal dusting (high CO concentration and 450-800 °C [52]). Therefore, a waste-heat boiler is used to rapidly cool down the RWGS product to allow for safe operation. However, it is worth to mention that preliminary investigations indicated that using the RWGS product gas for preheating the RWGS feed has the potential to increase the PtL efficiency drastically (in that case from 39.9 % to 47.5 %) [78]. As a result, it seems that there is a very large potential to increase the efficiency if the technical challenges of metal dusting can safely be ruled out.

C Fischer-Tropsch synthesis

Reactor types, catalyst and operating conditions:

The Fischer-Tropsch process targets to produce hydrocarbons from syngas. It is a well-established technology that has been implemented and running at large industrial scale for several decades. As it is highly exothermic, a good heat transfer is necessary in order to avoid e.g. hotspots in the reactor. Established reactor types are slurry bubble column, fixed-bed and fluidized bed reactors. The main challenge using slurry reactors is the separation of the product waxes from the catalyst particles. In contrast to the slurry reactor, more attention needs to be paid in a tubular fixed-bed reactor regarding the heat transfer. Dilution with inert components and lower once-through conversion reduces the risk of problems induces by the high exothermicity. There are two types of operation modes regarding the operating temperature of the FT reactor: low- and high-temperature FT meaning 200-240 °C and 300-350 °C, respectively. The higher the temperature the shorter the chain length of the product. High temperature FT is typically carried out using iron catalysts, whereas Fe and Co catalysts are both common for low-temperature FT. Cobalt catalyzed synthesis tends to produce linear paraffinic hydrocarbons whereas iron catalyzed FT also tends to produce a relevant amount of olefins (not suitable for jet engines). The reaction is typically performed at elevated pressure, 20-30 bar. The stoichiometric H_2/CO ratio is > 2, depending on the average hydrocarbon product chain length. Cobalt catalysts require a H_2/CO feed ratio between 2 and 2.3 (lower WGS activity) and iron catalysts between 0.5 and 2.5. In this work, a fixed-bed low-temperature system with Cobalt catalyst is chosen, based on Shell's FT plant in Bintulu, Malaysia (Shell Middle Distillate Synthesis, four FT reactors, each with a capacity of 8,000 barrels per day). A list of commercial plants (2,500-140,000 barrel per day) and testing units (3-1,000 barrel per day) with the applied reactor types, catalyst and temperature modes is available for example in [81] (this work: 1,900 barrel per day).

Model:

The Anderson-Schulz-Flory (ASF) distribution is a well-acknowledged approach to describe the FT product distribution. It relies on the chain growth probability α. From this the weight fraction of a certain carbon number can be estimated: $w_n = n\,(1-\alpha)^2\,\alpha^{(n-1)}$. In this work, the chain growth probability is calculated based on the equation proposed by Vervloet *et al*. [55], see Paper 1. Therein, α is calculated based on temperature and H_2/CO ratio. The overall process is setup to establish a constant inert gas content and H_2/CO ratio in the feed of the FT reactor independent of the RWGS operating conditions. However, in order to identify robust optimum RWGS operating conditions, local sensitivity analyses are conducted that investigate the impact of different FT operating conditions (temperature, inert gas content and CO conversion) on the optimum RWGS operating conditions.